NASA CR-*122385*

FINAL REPORT

for

COLLOID THRUSTER TECHNOLOGY

(August 1970 - September 1971)

Contract No. NAS 5-21025

Prepared by

Electro-Optical Systems
300 North Halstead Street
Pasadena, California   91107

for

Goddard Space Flight Center
Greenbelt, Maryland

FINAL REPORT

for

COLLOID THRUSTER TECHNOLOGY

(August 1970 - September 1971)

Contract No. NAS 5-21025

Goddard Space Flight Center

Contracting Officer: A. L. Essex
Technical Monitor: A. Sherman

Prepared by

Electro-Optical Systems
300 North Halstead Street
Pasadena, California 91107

Project Manager: Dr. Julius Perel

for

Goddard Space Flight Center

Greenbelt, Maryland

FOREWORD

The work described in this interim report is the result of the
second year of a program (Phase II) at Electro-Optical Systems
(EOS) under Contract No. NAS 5-21025 with NASA, Goddard Space
Flight Center (GSFC). The technical monitor was Dr. Allan Sherman
who contributed to the program direction. At EOS, Dr. Julius Perel
(Project Manager), and Messrs. John F. Mahoney and Howard L. Daley
performed the technical work and prepared this final report.
Preparation of laboratory apparatus and fabrication of annular
emitters were accomplished by Arthur Kasa and J. Robert Otto.

ABSTRACT

This program (Phase II) was a continuation of the previous
study program (Phase I) which attained control, reproducibility,
and predictability of operation for the annular colloid emitter.
The accomplishments of Phase I were utilized to obtain and oper-
ate a thruster of new design for a 1000 hour test during Phase II.
The thruster was operated with a neutralizer for 1023 hours at
15 kV with an average thrust of 25 μlb and specific impulse of
1160 sec. The performance was stable and the beam was vectored
periodically. The clean condition of the emitter edge at the
end of the test coupled with no degradation in performance dur-
ing the test indicated that the lifetime could be extrapolated
by at least an order of magnitude over the test time.

CONTENTS

ILLUSTRATIONS

ILLUSTRATIONS (contd)

ILLUSTRATIONS (contd)

SECTION 1

INTRODUCTION

The annular colloid thruster was shown to be feasible for application toward the control of satellites. The annular geometry evolved from the early work in which charged liquid droplets were generated and accelerated using capillary needle emitters. The superior features of the annulus as an emitter was initially demonstrated in the first phase of this program and is described in the Interim Report (Ref. 1) and publications (Ref. 2-4). The present report covers Phase II where the accomplishments of Phase I were utilized to design a thruster for stable operation over a period of 1000 hours.

The primary goal of the present phase was 1000 hours of continuous operation with good stability, reproducibility and with no deliterious effects such as erosion, emitter deposits, or any degradation of thruster performance. The initial work in this phase was devoted toward increasing specific impulse, developing reproducible emitter fabrication techniques, testing neutralization and vectoring methods, and preparing the duration test facility. Specific impulse was primarily enhanced by using a new propellant uncovered by an analytical study of propellants. From this study LiI was found to be a superior dopant to the previous standard NaI, and was therefore used in the duration test. An emitter design was developed that includes a platinum alloy emitter edge and a geometry that allows for adjustment of propellant flow impedance in fabrication. The achievement of reproducibility was demonstrated when the operational characteristics of two separate thrusters (1000 hour thruster and the D-thruster) were virtually identical. Previously developed neutralizer and vectoring techniques were tested with an annular thruster to assure reliable operation. The duration test facility was assembled and tested to provide the confidence required to undergo a 1000 hour duration test with good probability of success. In addition to those tasks relating to the duration test, an analysis was performed on the effect of various parameters upon a thermo-differential flow meter for ultimate use in measuring mass flow rates for operating thrusters.

To provide continuity with Phase I, Section 2 of this report briefly recounts the important performance and equations achieved in Phase I. The rest of the sections describe the analysis, apparatus, and tests accomplished during the program. Appendix I tabulates the geometries and properties of the emitters used while Appendix II contains a listing of the propellants. Identification of each of the test runs are contained in Appendix III. The test of the D-thruster and the flow meter analysis are contained in Appendices IV and V respectively. A description of the analysis on propellant properties is contained in Appendix VI.

SECTION 2

BACKGROUND

2.1 TECHNICAL GOALS AND DIRECTION

The primary technical goal of the second phase of the program was the operation of a single annular thruster with neutralizer for 1000 hours with good stability and reproducibility of operation. In addition, the performance specifications for the test included:

Thrust	25-35 μlb
Specific Impulse	>1500 sec
Voltage	<15 kV
Efficiency	>70%
Beam Spread	<25° half angle
Vectoring	$\pm 7^{\circ}$

These performance specifications were intended as goals to indicate the desired direction for improvement in performance during the development stage since they represented considerable improvement in the state-of-the-art thruster at the beginning of the program. More important was the emphasis upon stability and reproducibility with no generation of deposits (tar) at the emitter. With this emphasis, the specific impulse performance specification was determined to be the most difficult to achieve simultaneous with the others and that a level of ~1000 seconds was considered a substantial improvement. Thrust and specific impulse operational levels were found that assured stability for 1000 hours at near performance specification levels.

Much of the development work before the 1000 hour test was aimed at increasing the specific impulse while maintaining the stability and reproducibility achieved during the first phase of this program (Ref. 1). These were achieved by careful experimentation coupled with new analytical approaches to obtain a broad and detailed understanding of the dynamic characteristics of colloid spraying. The achievements and understanding obtained in Phase I will be summarized in Section 2.2 for use as a technical basis for the

present report. The thruster configuration and emitter designs are described in Section 3. Preliminary tests including neutralizer and vectoring development and experimental propellant studies are discussed in Section 4 and the 1000 hour test is described in Section 5.

2.2 SUMMARY OF ACCOMPLISHMENTS IN PHASE I OF THE PROGRAM

In this section the important features achieved in Phase I (Ref. 1) are summarized to provide the technical background for the present report (Phase II). Phase I was essentially an investigation of the dynamic characteristics of colloid particle generation and acceleration resulting in obtaining means and techniques for reliable prediction and application. In Phase II these techniques were used to increase performance and finally demonstrate these advancements with a successful 1000 hour test on the first attempt. The investigations of Phase I were aimed primarily at determining performance characteristics by changing the control variables in a methodical manner. Performance is ascertained by performance mapping and the use of performance indices to classify the total performance. The terms used and their units are given below:

Thrust Parameters

T –   Thrust (μlb)

I_{sp} –   Specific Impulse (sec)

$\langle C \rangle$ –   Mean Specific Charge (coul/kg)

I –   Emitter Current (A)

η –   Specific Charge Efficiency

Control Variables

V   -   Emitter Voltage (V)

$\dot{m}$ -   Propellant Mass Flow Rate (kg/sec)

Temp   -   Emitter Temperature (^{o}C)

              Geometry of the Emitter

              Propellant Properties

Performance Indices

k_o -   Charge Generation Index (coul/kg-V)$^{1/2}$

P   -   Specific Perveance Index $(A^2\text{-kg/coul-V}^3)^{1/2}$

The control variables are independent parameters that can be varied directly or indirectly. During a run the voltage is directly variable while the mass flow rate is dependent upon the feed pressure, the annulus temperature and the voltage. It also should be noted that both the temperature and voltage affect thrust parameters in addition to their effect on the mass flow rate. The thruster geometry and the propellant are not amenable to instantaneous variation during a run and are therefore only changed after careful analysis.

The performance indices and the specific charge efficiency describe the functional relationships between the thrust parameters and the control variables voltage and mass flow rate.

The resulting operational equations obtained from a coupled analytical and experimental investigation (Ref. 1) are:

$$T = (2\eta)^{1/2} \times f(x) \, PV^2 \tag{1}$$

$$I_{sp} = (2\eta)^{1/2} \, \frac{k_o f(x)}{g} \, V \tag{2}$$

$$\langle C \rangle = k_o{}^2 \, f^2(x) \, V \tag{3}$$

$$I = k_o \, x f^2(x) \, PV^2, \tag{4}$$

where

$$f(x) = x^{-1}(1-e^{-x}) \tag{5}$$

$$x = \frac{k_o \, \dot{m}}{PV} \tag{6}$$

The term g is the acceleration due to gravity, and all terms are in MKS units. To obtain thrust in μlb the following conversion factor is used:

$$T \, (\mu lb) = 0.225T \, (\mu N)$$

A non-dimensional form of displaying the thrust parameters (Eqs 1-4) as a function of mass flow rate at constant voltage is shown in Fig. 1. Plots of the experimental data display these general shapes. The data fit a portion of these curves corresponding to a range of x with the range depending upon the voltage and values of the performance indices. In effect, an increase in voltage causes an increase in the slope of the I and T curves and raising of the I_{sp} and $\langle C \rangle$ curves. A change in the index k_o has a similar effect since k_o is dependent upon properties of the propellant, the electric field at the emitter edge, and the temperature at the emitter edge. The value of the index P determines the range of x (or $\dot{m}$) in which I and T are near linear. The larger the value of P, the longer the near linear range. The index P is dependent upon the emitter edge length and the electric field configuration close to the emitter edge.

To improve performance, ways of increasing k_o were explored by examining dependency upon emitter geometry and propellant properties. Several important features were found and explored more throughly in Phase II.
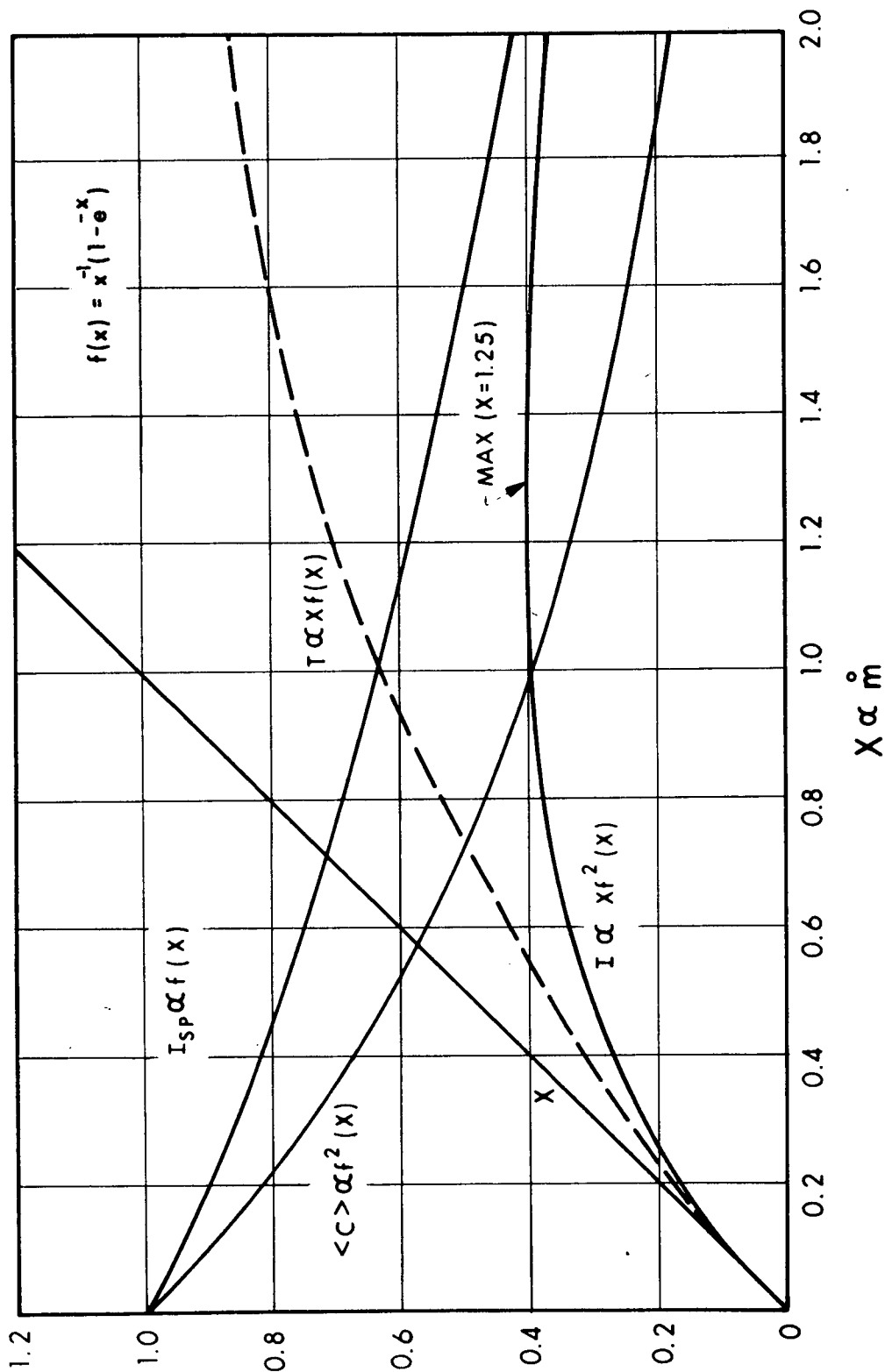
Figure 1. Parametric Variation with $\dot{m}$ at V = Constant

$$f(x) = x^{-1}(1 - e^{-x})$$

MAX (X=1.25)

$T \propto x f(X)$

$I_{SP} \propto f(X)$

$I \propto x f^2(X)$

$<C> \propto f^2(X)$

X

$X \propto \dot{m}$

It was possible in Phase I to predict, using the analytical equations and extrapolation of future improvements, the characteristics of an advanced thruster that would meet the performance goals of Phase II. These characteristics included performance indices of k_o = 0.81 and $P=87 \times 10^{-13}$ with $\eta=80\%$ for operation at 15 kV. In addition, a trap electrode was introduced to minimize electron bombardment of the emitter which could have been hazardous when a neutralizer was operated close to the thruster. Electron bombardment was found to be associated with emitter glow and discharge extractor currents, high beam divergence, excessive TOF noise, poor reliability and reproducibility, and the generation of tar.

The present state-of-the-art thruster utilizes the improvements made in Phase I plus others made in Phase II to obtain performance characteristics that nearly match the early prediction. These improved characteristics were demonstrated by the 1000 hour endurance test described in Section 5.

SECTION 3

THRUSTER SYSTEM

3.1 EXPERIMENTAL ARRANGEMENT

For most of the thruster tests on Phase II of the program, the experimental arrangement was very similar to the arrangement used in Phase I which was described in the Interim Report (Ref. 1) so only a brief description is included here.

The vacuum system used for most of the tests was a 2 foot diameter by 3 foot long chamber with a liquid nitrogen cooled liner. Pumping speeds were sufficient to permit operation in the 10^{-7} Torr pressure range. The vacuum system contained the collector system shown schematically in Fig. 2 which illustrates the general experimental setup. The segmented collectors and the time-of-flight (TOF) collectors were provided with separate leads which permitted either individual or collective measurements of current as shown. The TOF collectors contained one grid used to suppress secondary electrons and a second grid used as an electrostatic shield. Each of these components could also be biased as desired.

The annulus is run at a high positive voltage (+15 kV), the inner extractor (not shown) is run at high negative voltage (-2kV), and the outer extractor and trap electrode (not shown) are run at a slightly negative voltage (-200 to -500V). Propellant is supplied from the reservoir with a flow rate meter occasionally used. An analysis of the mass flow meter technique used is given in Appendix V. TOF data is obtained by pulsing the annulus voltage to ground and observing the decay of the current to the TOF collectors using an oscilloscope or the automatic data acquisition system (DAS).
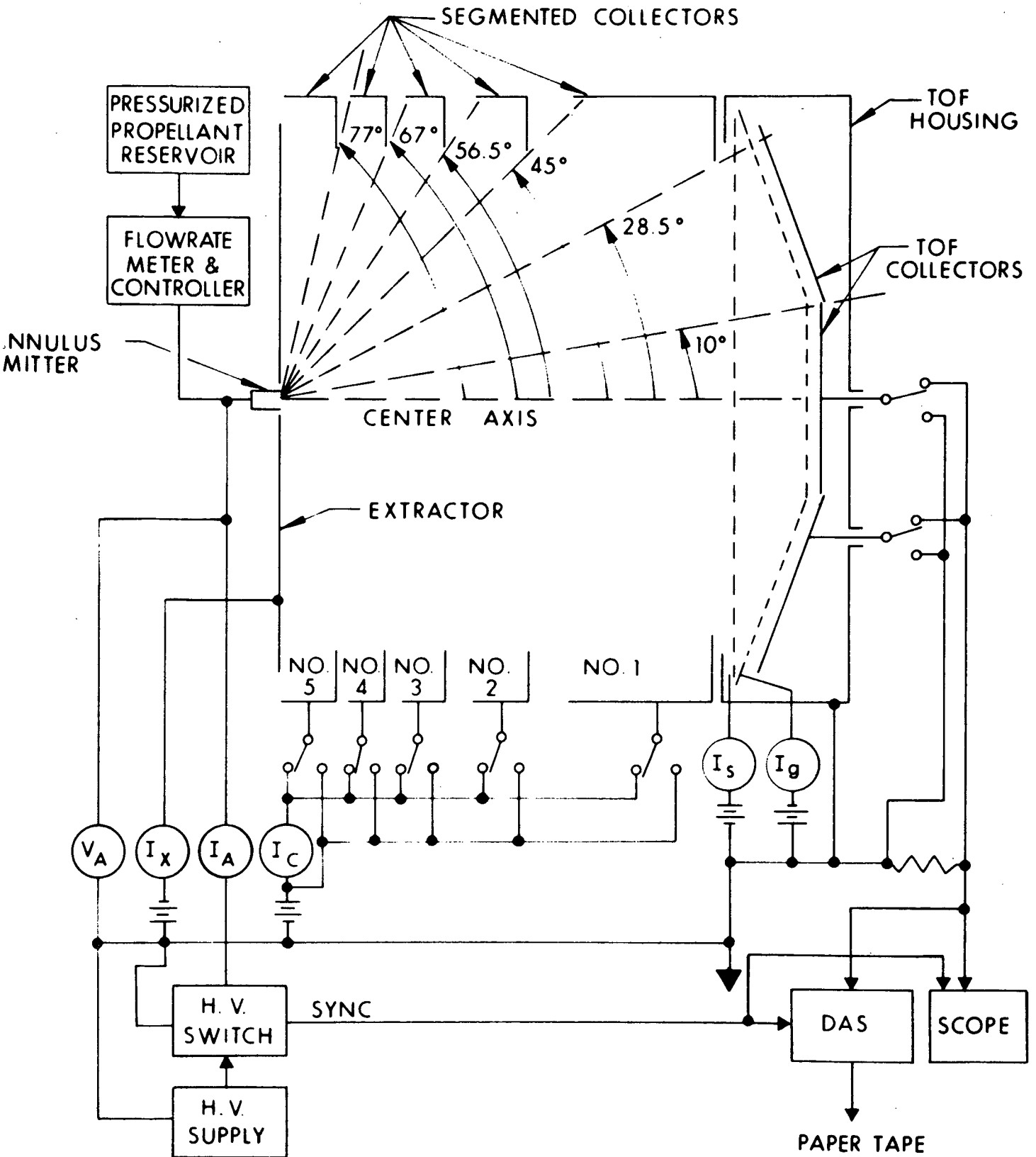
Figure 2. Schematic Diagram of Experimental Setup

3.2 THRUSTER CONFIGURATION

The basic thruster configuration used for the exploratory investigation culminating in a successful 1000 hour test is shown schematically in Fig. 3. Photographs of the deliverable annular colloid thruster (D-Thruster) with neutralizer are shown in Fig. 4 (a) and (b). Variations of the basic thruster configuration are discussed in the appropriate sections of this report. Details of the annulus emitter design, fabrication and tests for reproducibility are discussed in Section 3.3. The performance of the D-Thruster is given in Appendix IV.

The standard emitter is a 1/2 inch diameter annulus nominally operated at +15 kV. Centered within the annulus is a 0.3 inch spherical inner extractor which has been operated between -2 and -5 kV. In addition to providing desirable focusing properties, the inner extractor serves to partially confine the positive potential region to the vicinity of the annular emitter edge. An electron trap electrode, in conjunction with the inner extractor, effectively shields the emitter from electron bombardment. The experimental investigations leading to the trap electrode concept as a means of preventing glow discharge, inner extractor currents, and emitter bombardment by electrons is discussed in Ref. 1. The trap electrode has a 1.25 inch aperture and is located 0.25 inches forward of the outer extractor plate. It is usually operated at -500 volts which has proved sufficient in shielding the thruster from electrons originating from the neutralizer and/or collector surfaces. The outer extractor is a circular plate with an aperture providing a nominal 0.050 inch gap between the extractor and the annulus rim. For vectoring operations, the outer extractor is segmented to provide deflection as well as extraction capability. The design and operation of vectoring electrodes is discussed in more detail in Section 4.2.

TRAP ELECTRODE

OUTER EXTRACTOR / VECTORING ELECTRODES

INNER EXTRACTOR

NEUTRALIZER FILAMENT SHIELD

NEUTRALIZER FILAMENT

THERMOCOUPLE

ANNULUS EMITTER
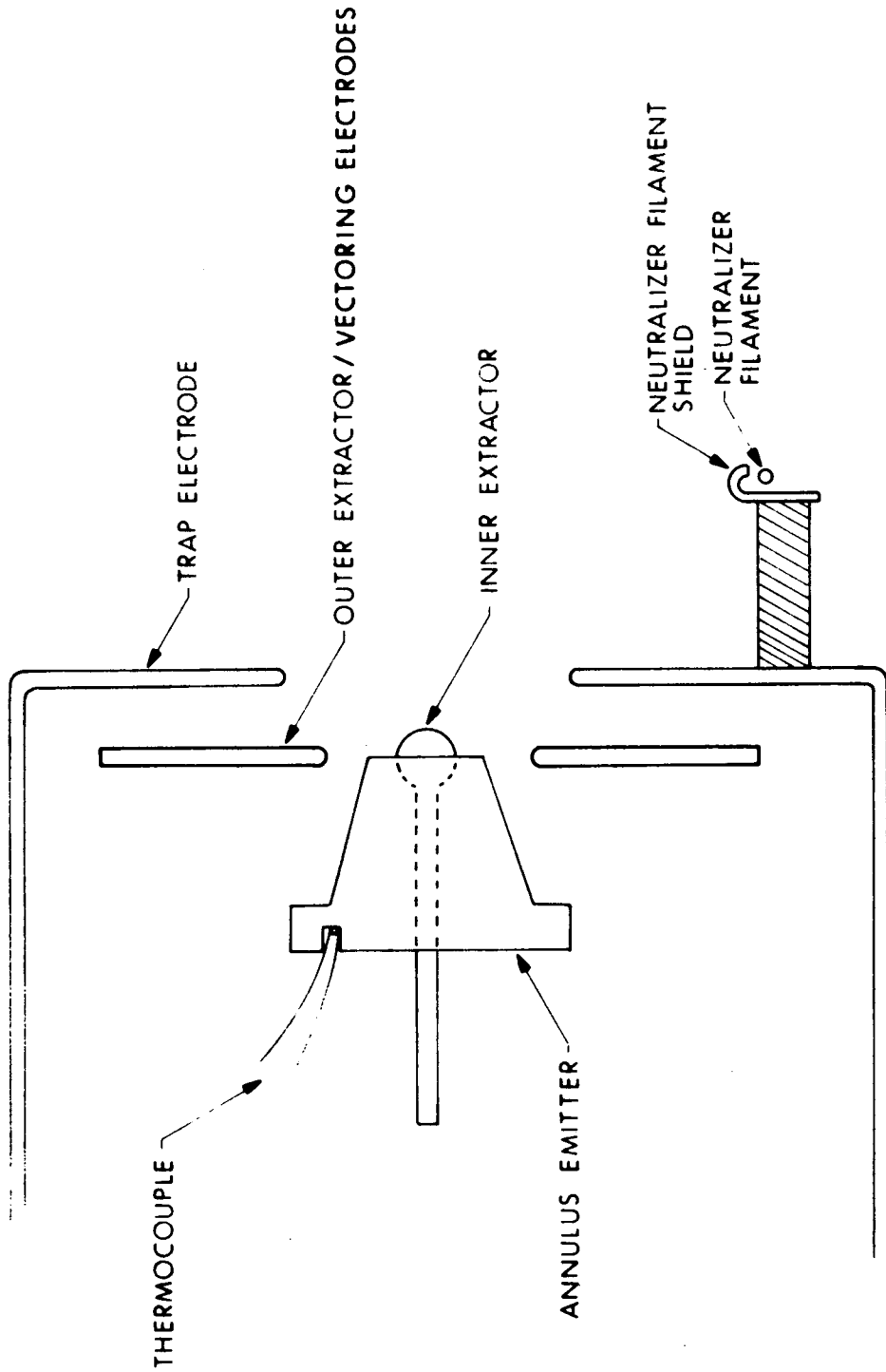
Figure 3. Schematic Representation of Basic Thruster Configuration

4040-Final

12

(a)
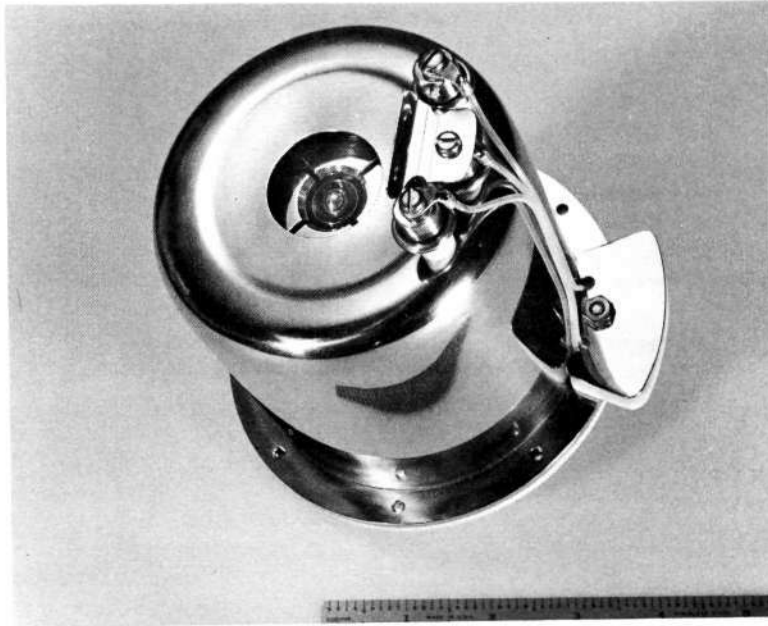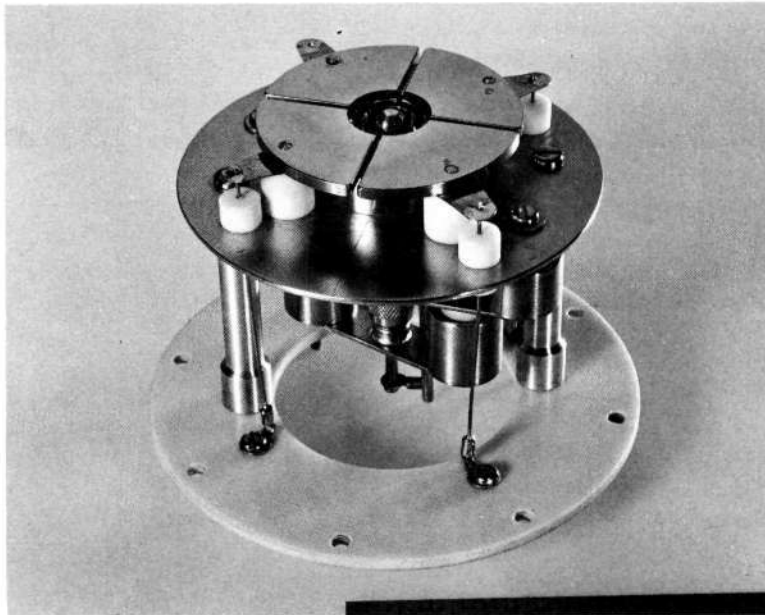
(b)

Figure 4. (a) Colloid Annular Thruster with Neutralizer
(b) Interior of Thruster with Trap Electrode Housing Removed

The thruster assembly includes a neutralizer filament, usually 0.007 inch diameter tantalum wire, mounted on the trap electrode housing and extends one to two inches forward. A neutralizer filament shield is used to prevent the suppression of electrons from the filament caused by the interaction of the negative trap potential with the neutralizer. The tradeoffs involved with floating beam potential and trap electrode voltage along with other neutralizer features are treated in Section 4.3. A shielded thermocouple mounted in the base of the annulus emitter, is used to monitor the annulus temperature.

3.3 EMITTER DESIGN AND FABRICATION

The design of an annulus involving techniques of construction aimed primarily at reproducibility was completed and several emitters were tested. The goals of this emitter study were directed toward the fabrication of annuli with reproducible gap spacings, gap length and gap concentricity. The essential features of the tapered annulus emitter design are displayed in Fig. 5. The mating of the outer annulus sleeving to the inner by use of the taper controls the concentricity to a degree not obtainable using past emitter construction techniques. The surfaces of the annulus sleevings over which the propellant flows are lapped together by rotating the outer sleeving around the inner sleeving using a lapping compound. This produces a uniform gap spacing along the entire flow length of the emitter and therefore a reproducible flow impedance. Insertion of shims (0.0005 to 0.001 inch thickness) between the annulus sleevings determines the gap width. It was observed that shims of different materials having the same thickness result in different permeabilities which is attributed to variances in the compressibilities of the materials encountered during the press fitting of the sleeving surfaces. The gas flow permeability method used in measuring flow properties of emitters is discussed in Appendix I.
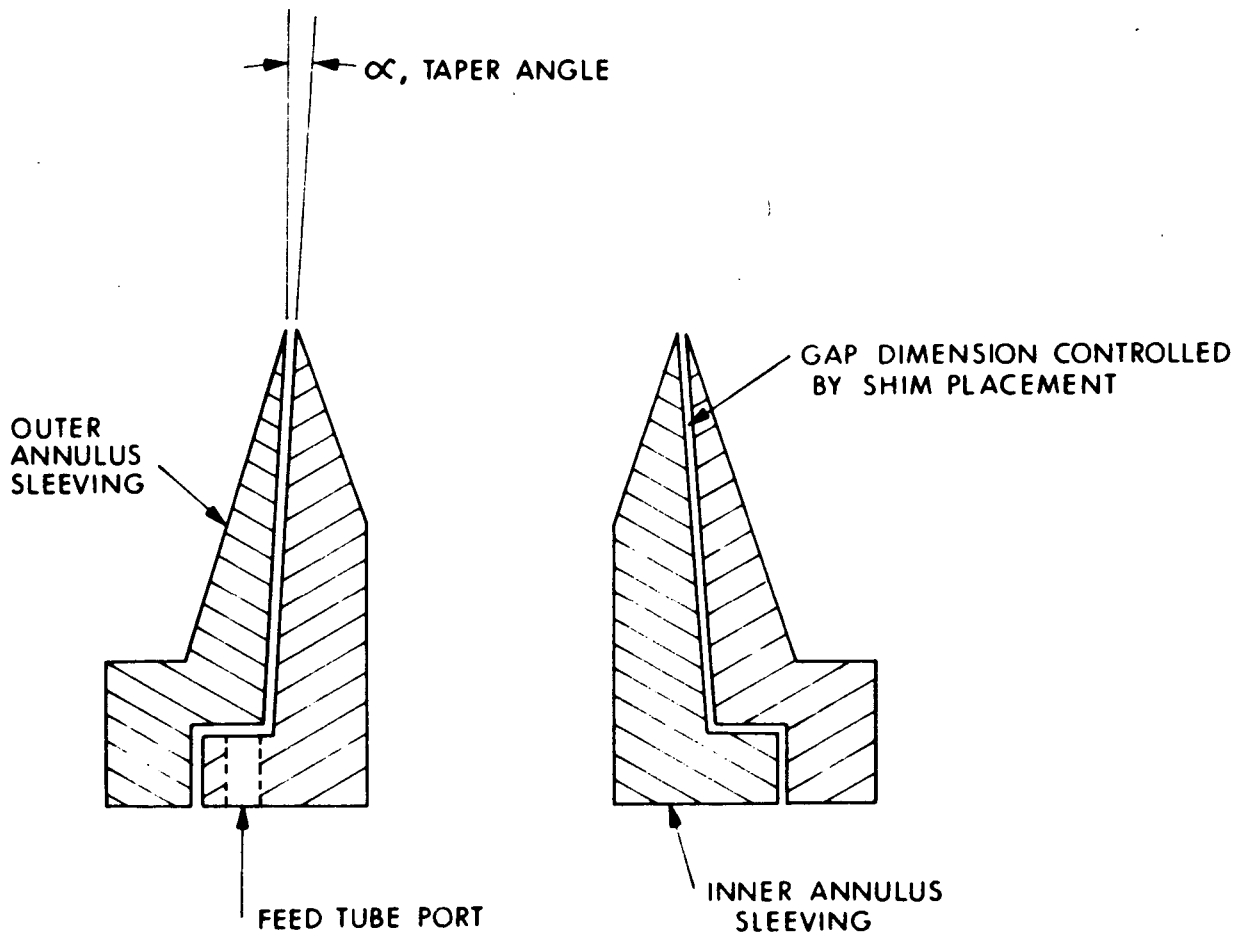
Figure 5. Basic Tapered Annulus Emitter Design (not to scale)

39322

Tapered annulus T01 had a five degree taper angle (α) and an emitting edge thickness of nominally 0.001 inch. The gap spacing was controlled by using shims of various thickness. Prior to lapping the inner and outer sleeving, normalized permeabilities of 21.0 and 2.0 were obtained for gap spacings of 0.001 and 0.0005 inch, respectively. After lapping, normalized permeabilities of 21.0 and 2.9 were obtained for the same spacings. This indicates that the surface condition has a noticeable effect in restricting gas flow when the gap spacing is on the order of 0.0005 inch but was not noticeable for the 0.001 inch gap spacing. However, at 0.0005 inch, an approximate increase of about 50% in permeability was observed. This taper design, together with lapping techniques, appears promising for making reproducible emitters.

A technique for fabricating the edges of annulus emitters from platinum/iridium to obtain more corrosion resistant edges was developed at EOS. The Pt/Ir tipped annulus was assembled by brazing a .020 inch thick Pt/Ir washer onto a 20Cb3 stainless steel cylinder which was the main annulus body. The braze filler was a AuNi compound consisting of 82% Au and 18% Ni with a flow temperature of approximately 1048°C. Following the brazing operation, annulus emitters were constructed using conventional techniques described above. Figure 6 is a cross sectional view showing details of composition and dimensions of the Pt/Ir emitter edge. Tests with emitter T01 and other emitters with the taper design are discussed in Sections 4.1, 4.2 and 4.4.

PLATINUM (90%) / IRIDIUM (10%)

20 Cb 3 STAINLESS STEEL

.020 INCH

.003 INCH

GAP SPACING .0005 INCH

.250 INCH

NIORO
BRAZE
BOUNDARY
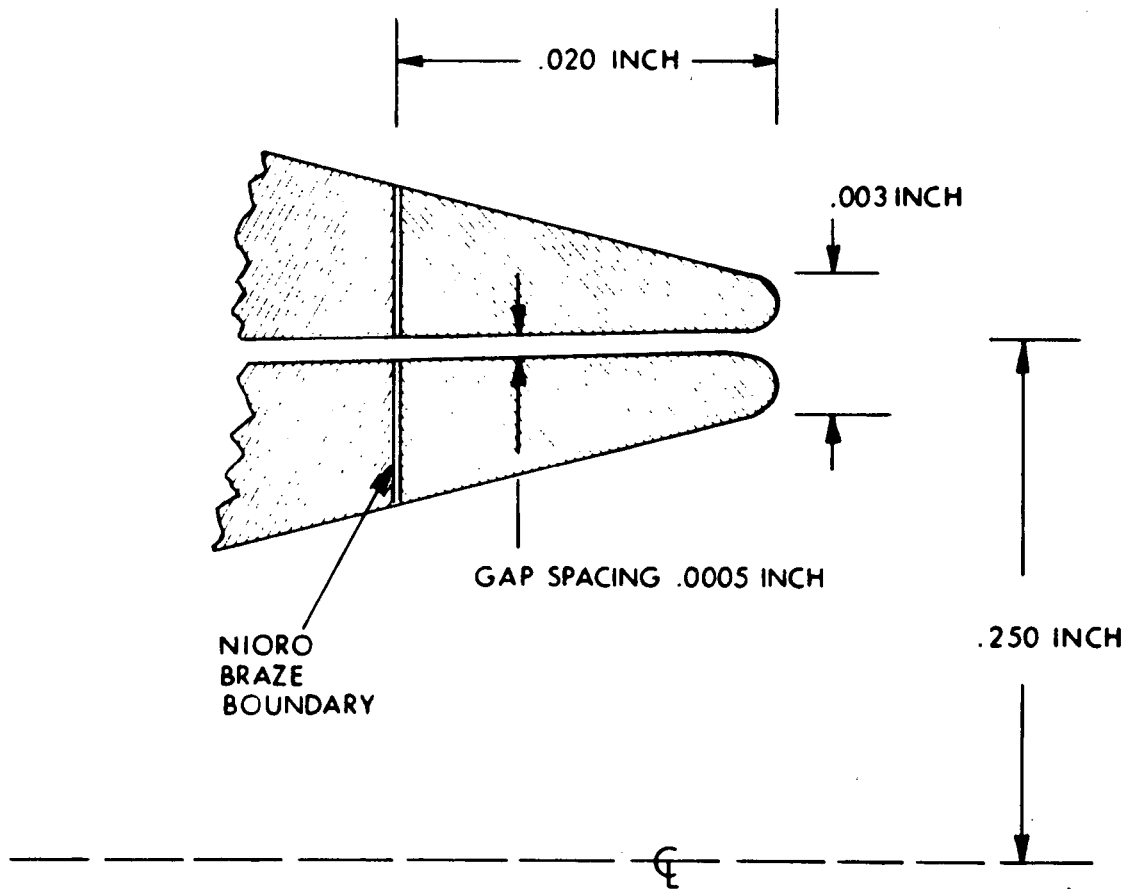
Figure 6. Annulus Emitter Showing Composition and Dimensions
of Emitter Edge

SECTION 4

THRUSTER TESTS

4.1 EMISSION STUDIES

4.1.1 SUMMARY OF PROPELLANT TESTS

Several propellant tests were conducted during this program with the
goal of finding an ionic dopant which could produce higher specific
charge particles (and therefore higher specific impulse) than NaI.
The propellant fluids were tested under similar operating conditions
using the same annulus (A06) and identical inner and outer extractor
geometries. The dopants for these tests were generally selected on
the basis that the total number of dissolved molecules in 100 ml
glycerol be greater than the number in 30 gms NaI in order to test
the hypothesis that undissociated molecules contribute significantly
to the surface charge of droplets by dissociating under the influence
of high fields (see Appendix VI for analysis details). The choice of
which dopant to test was not based on whether the specific or equiva-
lent conductivity of the resulting mixture was higher than that of NaI
since of all dopants tested only KI exhibited a higher equivalent con-
ductivity. Figure 7 was used as an aid in selecting potential dopants
by giving the number of available ions for a completely dissociated
electrolyte in glycerol (N) as a function of the weight of solute in
grams per 100 ml glycerol. Actually N is identical to the total number
of dissolved molecules.
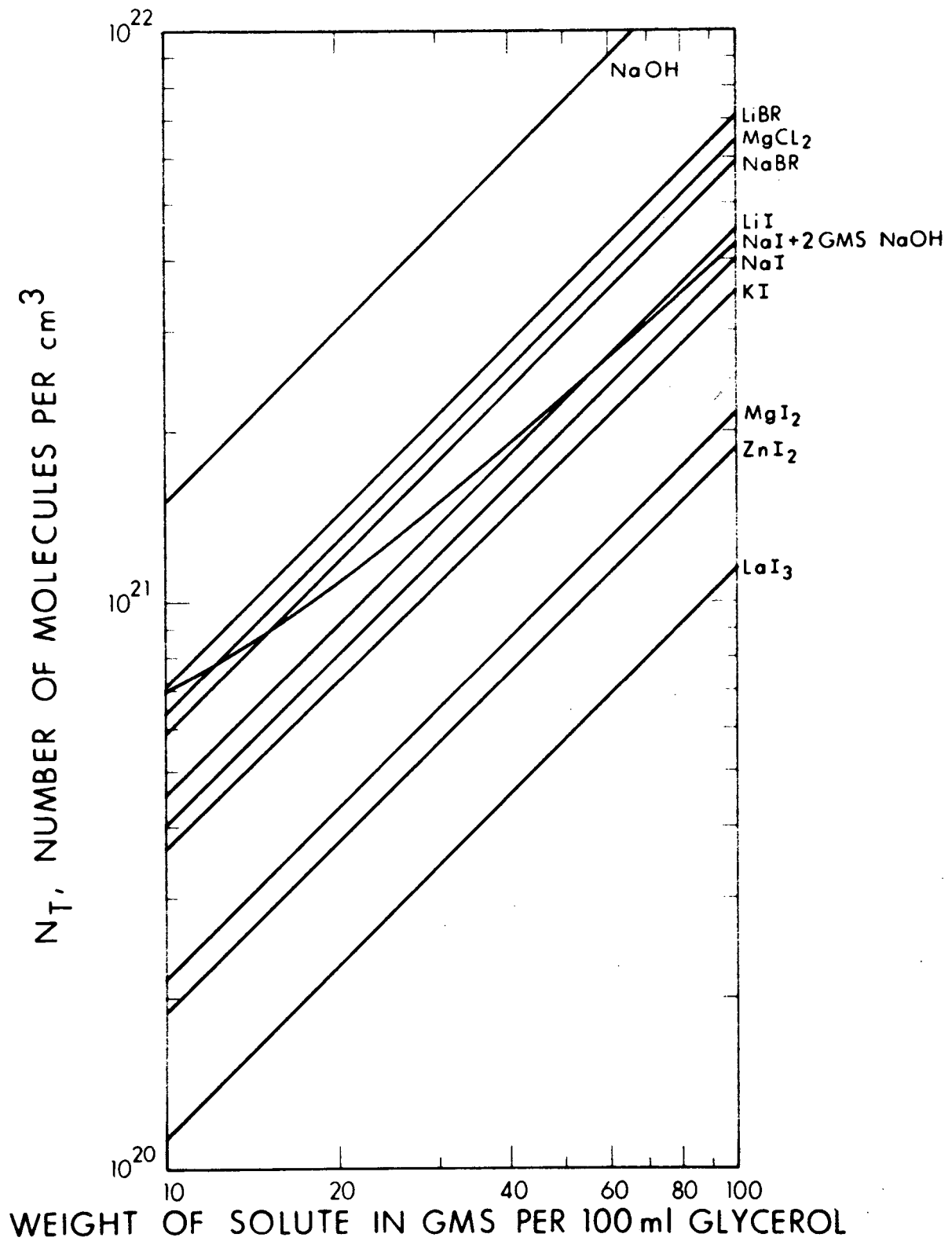
Figure 7. Number of Molecules (Available Ions for a Completely Dissociated Electrolyte) for Various Solute Weights in Glycerol

38740

The specific impulses obtained with various fluids are compared under similar conditions at constant temperature and voltage in Fig. 8. A plot of specific impulse versus mass flow rate for a solution of 30 gms NaI/100 ml glycerol using the same annulus is included for reference purposes. In all cases the specific impulse performance is improved over that of NaI. Note that the addition of 2 gms NaOH increased the specific impulse over the NaI-glycerol mixture by about 450 seconds in the mass flow rate region tested. From Fig. 8 it is apparent that the rate of change of specific impulse with mass flow rate for most of the propellants tested follow similar lines. The LiI propellant, however, exhibited a large ΔI_{sp} with mass flow rate. It was the only one which was not filtered and had a blue-grayish color. When the solution was filtered it yielded a clear fluid. It appears that the coloration was due to undissolved particles which may have produced clogging. Clogging could result in an increase of mass flow per unit emitter length which would explain the character of LiI data illustrated in Figs. 8, 9 and 10. This behavior is also characterized by its unusually low specific perveance index, P, shown in Table I which summarized the results of these tests. The thrust and source current for the various propellants tested are plotted against mass flow rate at constant temperature and voltage in Figs. 9 and 10, respectively.

4.1.2   DESCRIPTION OF INDIVIDUAL PROPELLANT TESTS

30 gms LiI/100 ml Glycerol (Run No. 7011-01)

The specific impulse performance of the LiI doped glycerol propellant at various voltages and temperatures is shown in Figs. 11 and 12, respectively. The results are similar to data obtained with NaI propellant investigated in the past. Figure 11 shows the specific impulse increasing with voltage and Fig. 12 shows the decrease of specific impulse with increasing temperature. This data is an indication that the specific charge for the LiI propellant is decreasing with increasing temperature.
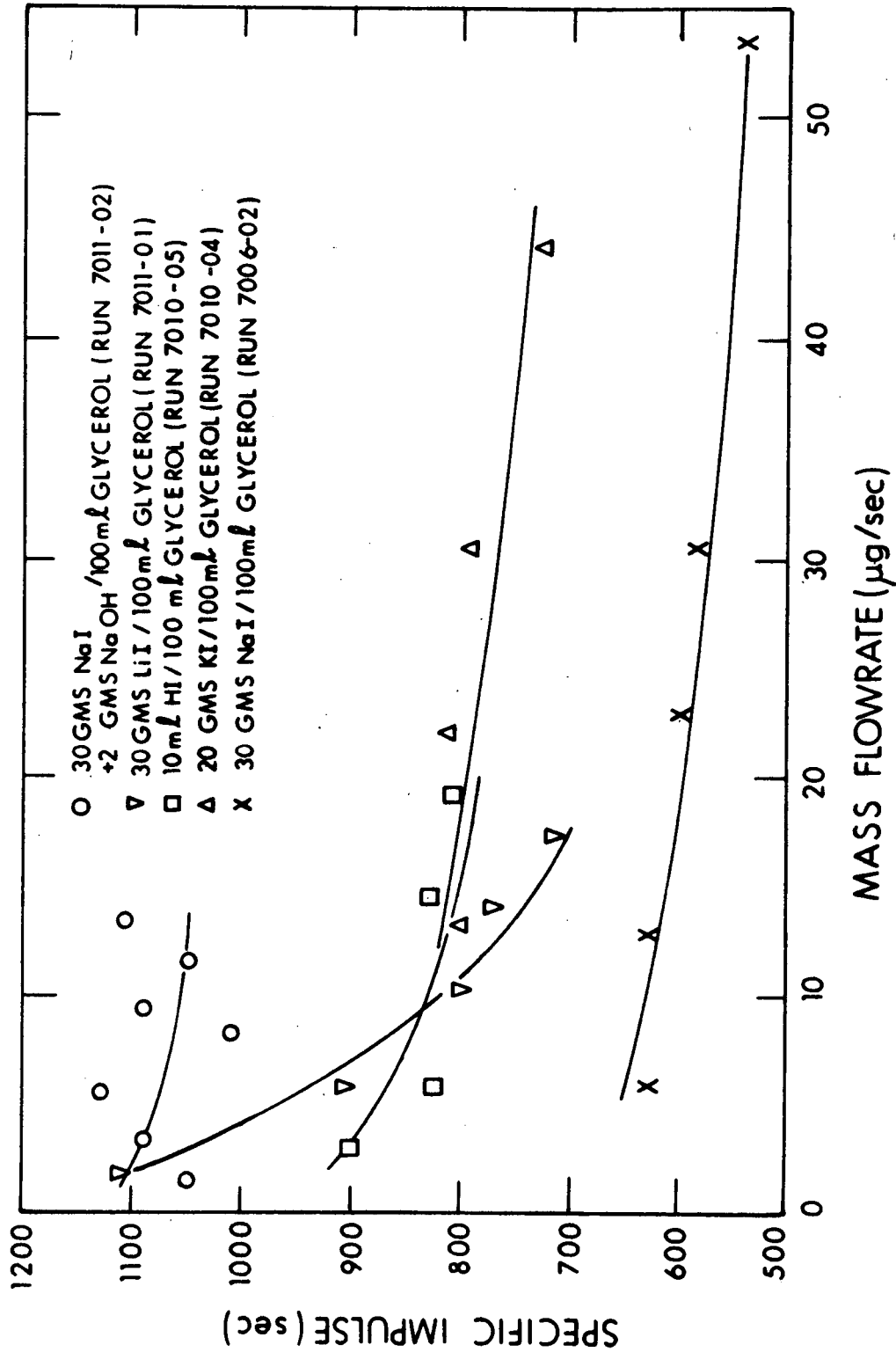
Figure 8. Specific Impulse versus Mass Flowrate Characteristics for Various Electrolytes in Glycerol at Constant Temperature (-1 to +1°C) and Voltage (15 kV) for Annulus A06

40110
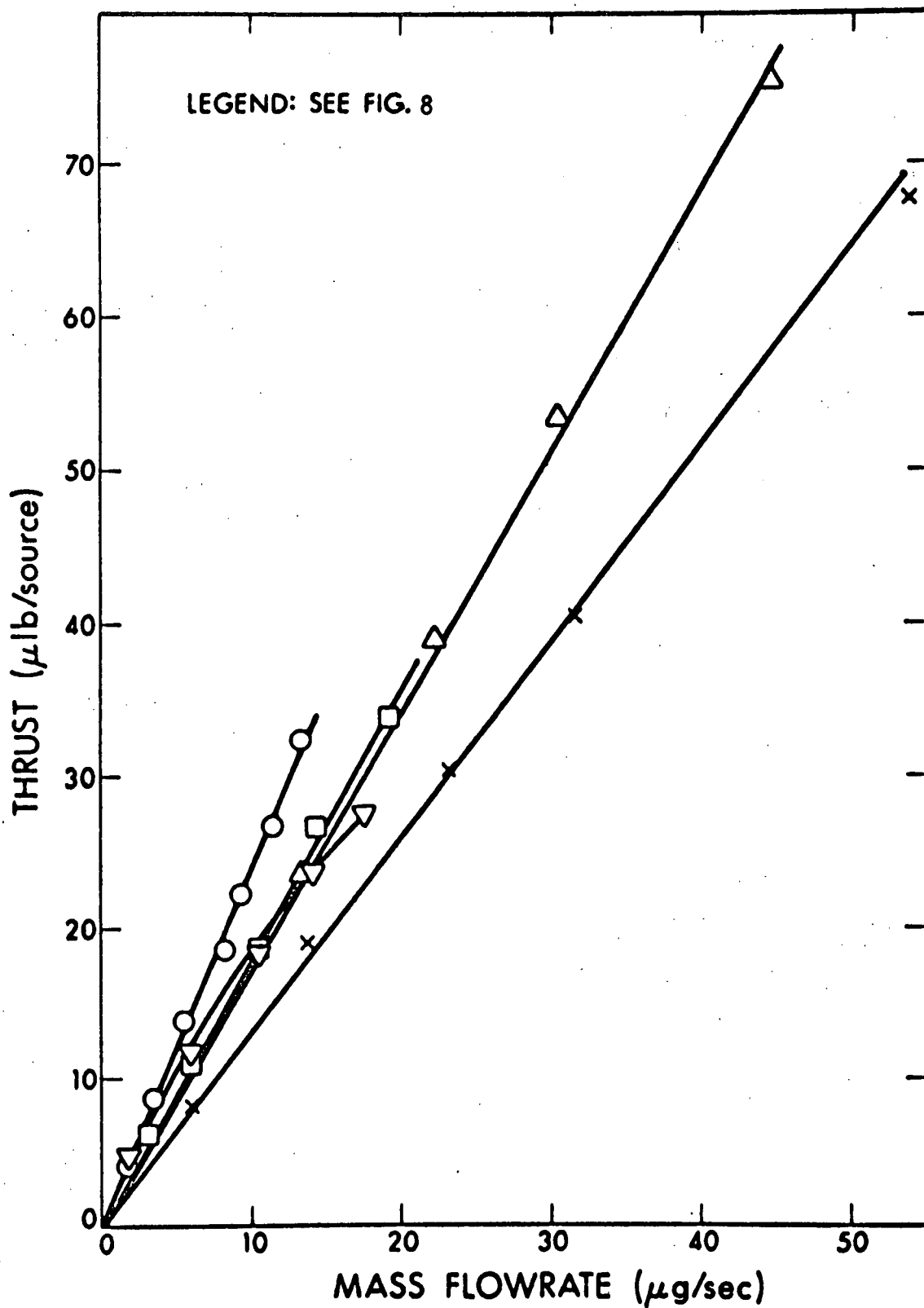
Figure 9. Thrust versus Mass Flowrate for Various Electrolytes
in Glycerol at Constant Temperature (-1 to +1°C) and
Voltage (15 kV) for Annulus A06

Figure 10. Source Current versus Mass Flowrate for Various
Electrolytes in Glycerol at Constant Temperature
(-1 to +1°C) and Voltage (15 kV) for Annulus A06

38737

TABLE I

PERFORMANCE INDICES OF THRUSTER EMITTERS

RUN NO. See Appendix III	EMITTER See Appendix I	PROPELLANT See Appendix II	TEMPERATURE $^\circ$C	$\left(\dfrac{k_o}{\text{A-sec}}\Big/\text{kg-V}\right)^{\frac{1}{2}}$	$\left(\dfrac{P}{\text{A-kg}}\Big/\text{sec-v}^3\right)^{\frac{1}{2}}$
7006-02	A06	F05	0	0.38	63×10^{-13}
7010-04	A06	F11	+1	0.41	97
7010-05	A06	F13	-1	0.48	>70
7011-01	A06	F15	+1	0.55	8.7
7011-02	A06	F16	-1	0.61	>70
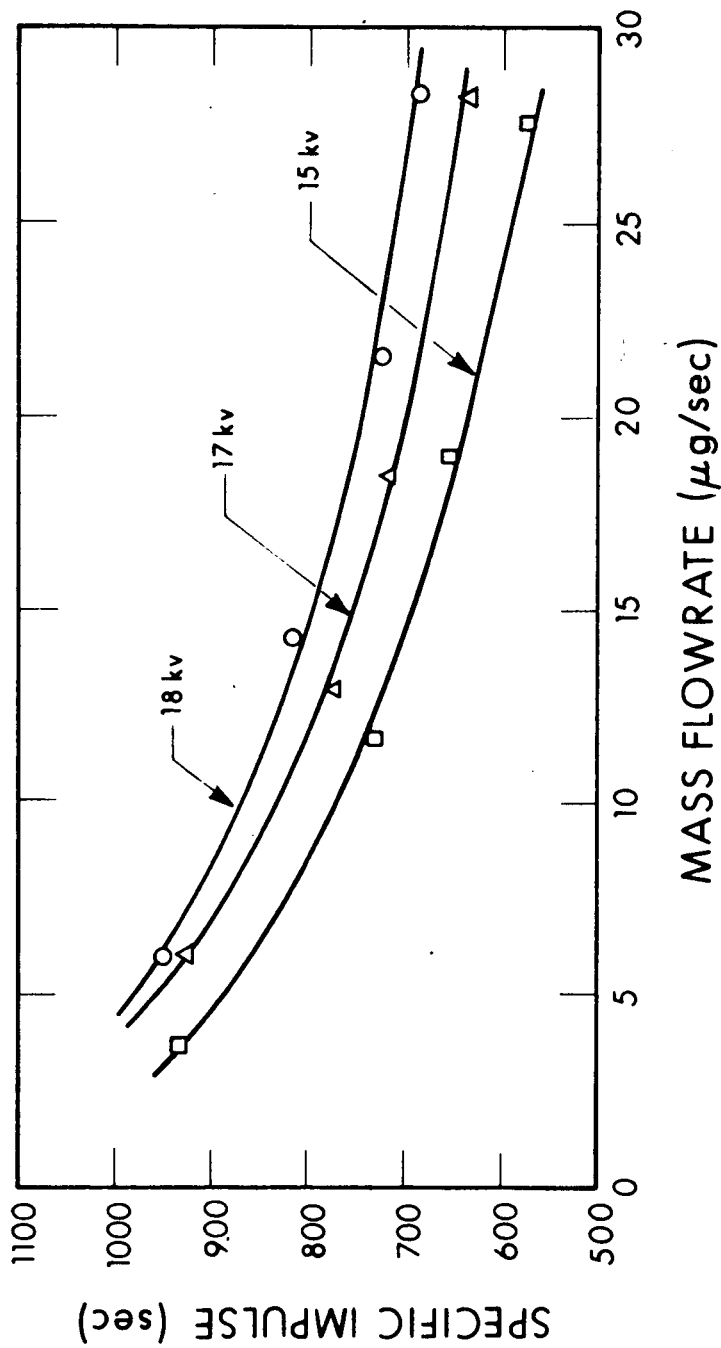
Figure 11. Specific Impulse versus Mass Flowrate for 30 gms LiI/100 ml Glycerol at +10°C for Three Voltages (Annulus A06 – Run 7011-01)
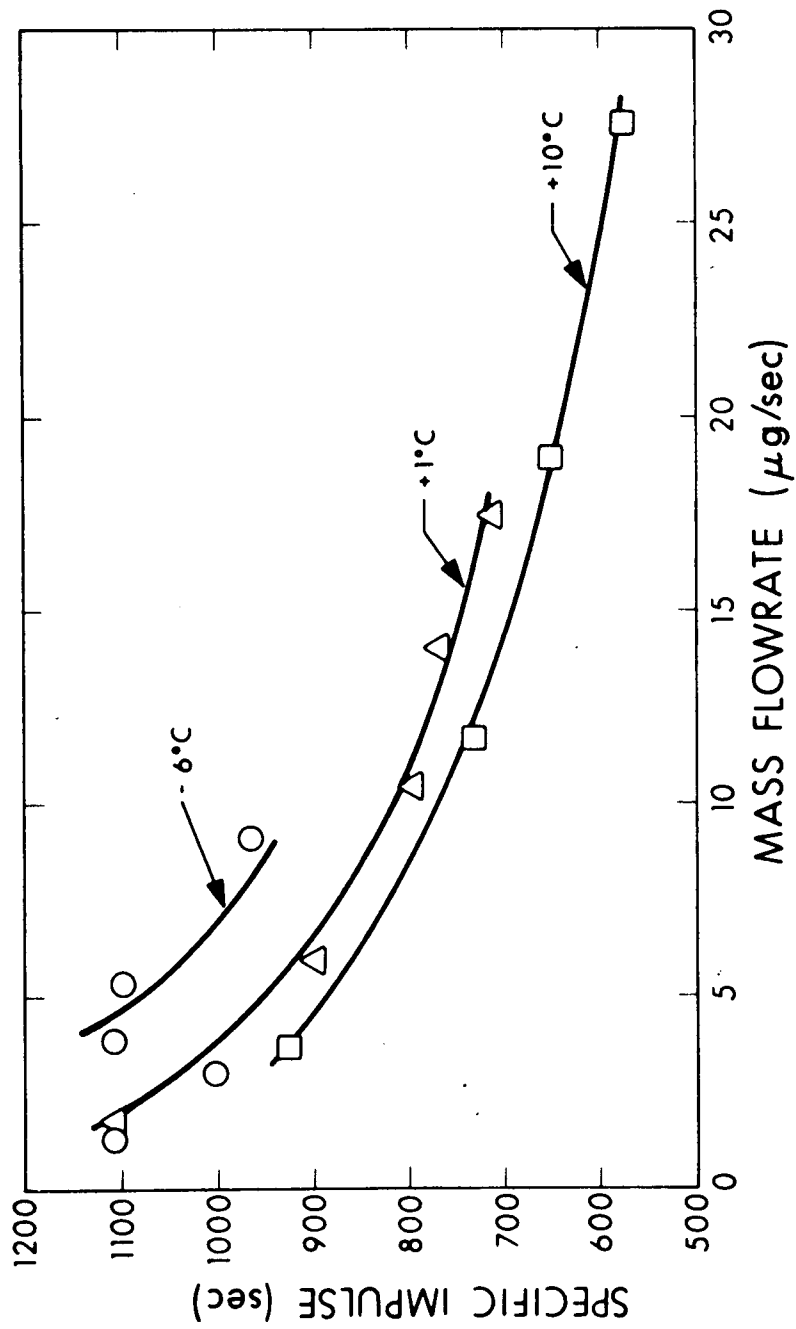
Figure 12. Specific Impulse versus Mass Flowrate for 30 gms LiI/100 ml Glycerol
at 15 kV for Three Temperatures (Annulus A06 - Run 7011-01)

30 gms NaI + 2 gms NaOH/100 ml Glycerol (Run No. 7011-02)

Figure 13 shows the specific impulse versus mass flow rate perfor-
mance for 30 gms NaI + 2 gms NaOH/100 ml glycerol (F16) at various
temperatures and voltages. This dopant-fluid combination has re-
sulted in the highest specific impulse obtained using annulus A06.
NaOH was chosen as a compound for producing a poly-electrolytic solu-
tion because small amounts yield a large number of molecules owing to
its low gram molecular weight. In addition, NaOH and NaI have identical
cations. Examination of the emitter after over 30 hours of testing with
this fluid revealed no traces of material precipitate. Other investiga-
tors have observed varying amounts of precipitate when NaOH was used as
a dopant in glycerol and sprayed with needle emitters (Ref. 5).

30 gms NaI + 3 gms NaOH/100 ml Glycerol (Run 7011-03)

The specific impulse and thrust variation with mass flow rate at 15 and
17 kV emitter potentials for propellant F17 (30 gms NaI + 3 gms NaOH/100 ml
glycerol) using annulus A06 are shown in Figure 14. This data was taken
at a constant emitter temperature of $+10^{\circ}C$ and has an index value of
$k_o=0.52$. Note that a specific impulse of over 1000 seconds was obtained
at a thrust level of 30 μlbs at 17 kV. Although high specific impulses
(>1000 sec) can be obtained using a NaI + NaOH combination in glycerol,
the dc characteristics do not exhibit the stability obtained with NaI
above. The need to quantitatively measure the dc characteristics of a
fluid for purposes of comparing this aspect of performance stability
for various propellant fluids is apparent.
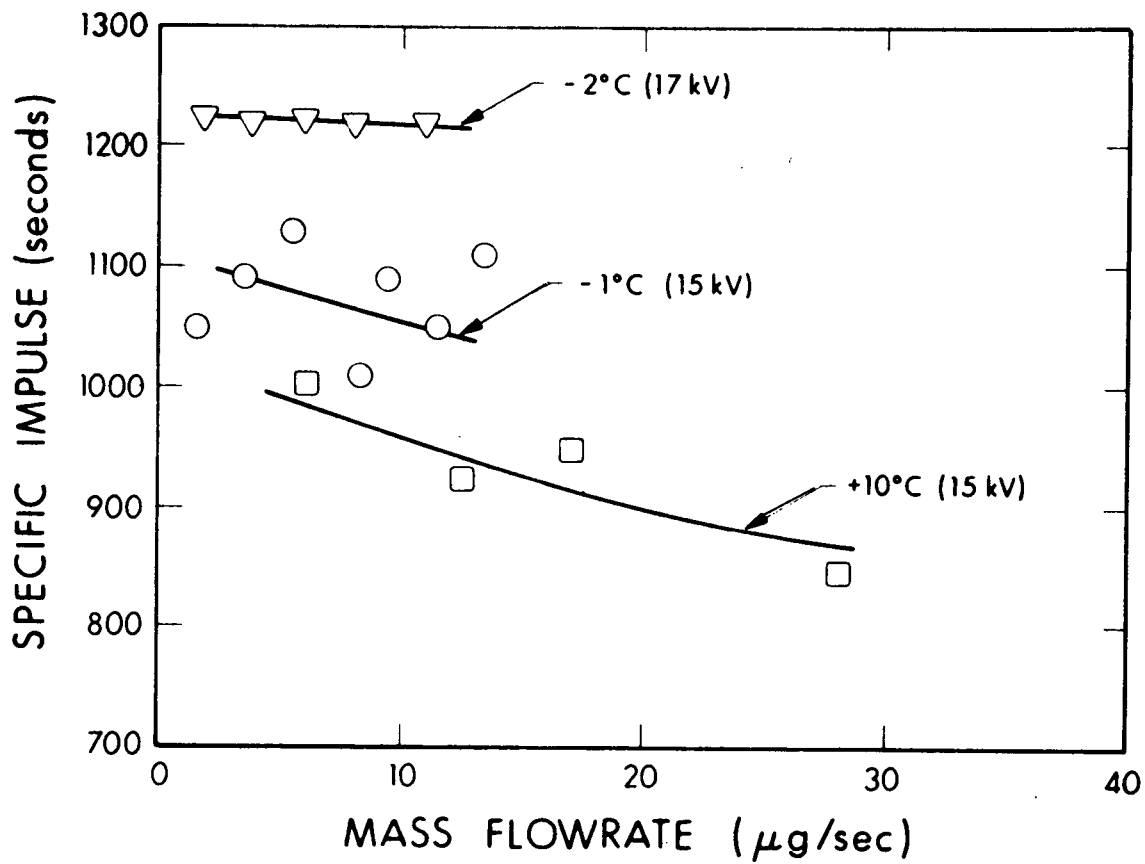
Figure 13. Specific Impulse versus Mass Flowrate for 30 gms NaI plus 2 gms NaOH/100 ml Glycerol at Various Temperatures and Voltages (Run 7011-02)
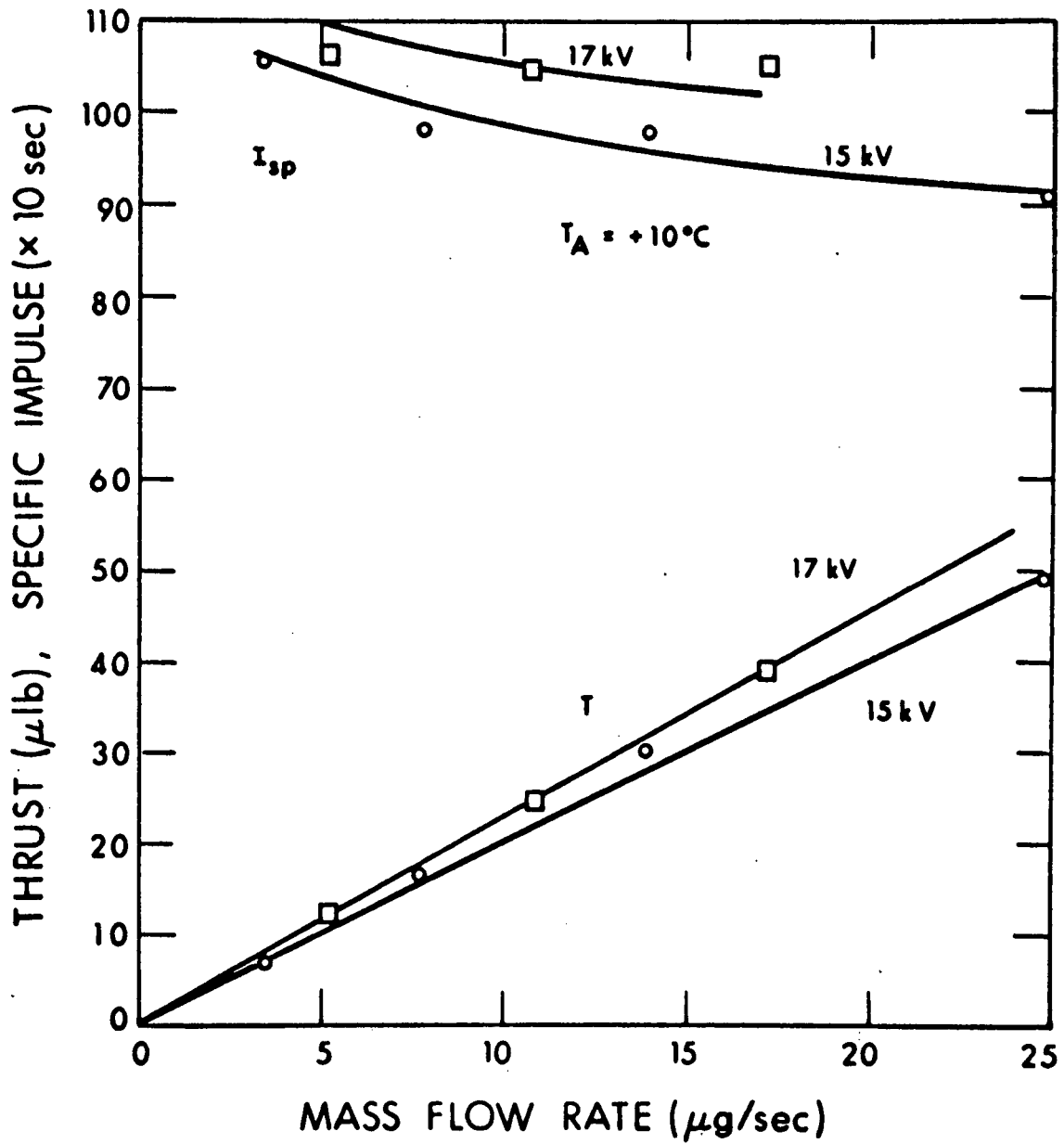
Figure 14. Specific Impulse and Thrust versus Mass Flowrate at Various
Voltages for 30 gms NaI plus 3 gms NaOH/100 ml Glycerol Test
Propellant (Annulus A06, Run 7011-03)

30 gms LiI + 1 gm LiOH/100 ml Glycerol (Run 7012-02)

The specific impulse and thrust variation with mass flow rate at 15, 17 and 18 kV emitter potential for propellant F15A (30 gms LiI + 1 gm LiOH/100 ml glycerol) using annulus A06 are shown plotted in Figure 15. This data was taken at a constant emitter temperature of $0^{\circ}C$ and has a performance index $k_{o} = 0.54$. The dc stability with this fluid compares favorably with that of NaI doped fluids. The specific impulse variation with mass flow rate for propellant F15A as a function of temperature is shown in Figure 16.

CONCLUSIONS

The results of these propellant tests lend support to the hypothesis that higher specific charge (compared to NaI doped fluids) can be obtained by dopants that yield a greater reservoir of dissolved molecules for equal weights of dissolved material. This was predicted by the theory discussed in Appendix VI and has been proven experimentally. The results also indicate that the high field dissociation of molecules to form ions is significant. This was also predicted by theory and, in fact, the field production of ions in excess of those formed by the usual chemical kinetics was shown to be dominating. (See Appendix VI).

Both the experimental and theoretical study provide evidence showing that the search for a fluid capable of producing high specific charge based solely on measurements of "zero field" specific conductivity is not justified. For example, fluids which have lower measured specific conductivities than 30 gms NaI have been experimentally tested to produce higher specific charges under identical operating conditions. The performance of some of the propellant combinations tested during this program has provided valuable data for a better understanding of the nature of electrolytic propellant solutions. To date, lithium iodide appears to be superior dopant for glycerol when compared to sodium iodide.
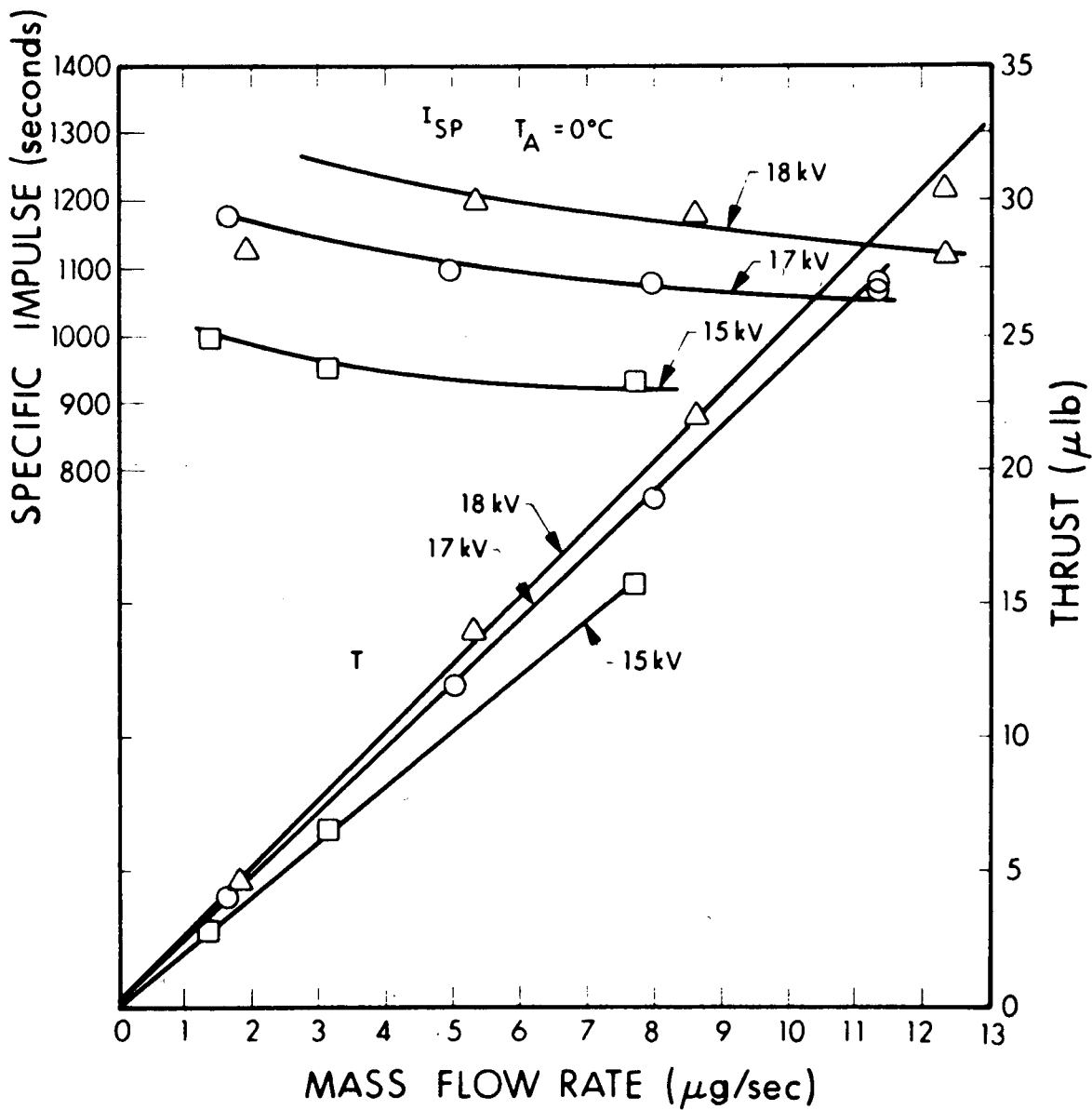
Figure 15. Specific Impulse and Thrust versus Mass Flowrate
at Various Voltages for 30 gm LiI plus 1 gm LiOH/
100 ml Glycerol Test Propellant (Annulus A06,
Run 7012-02)

38938
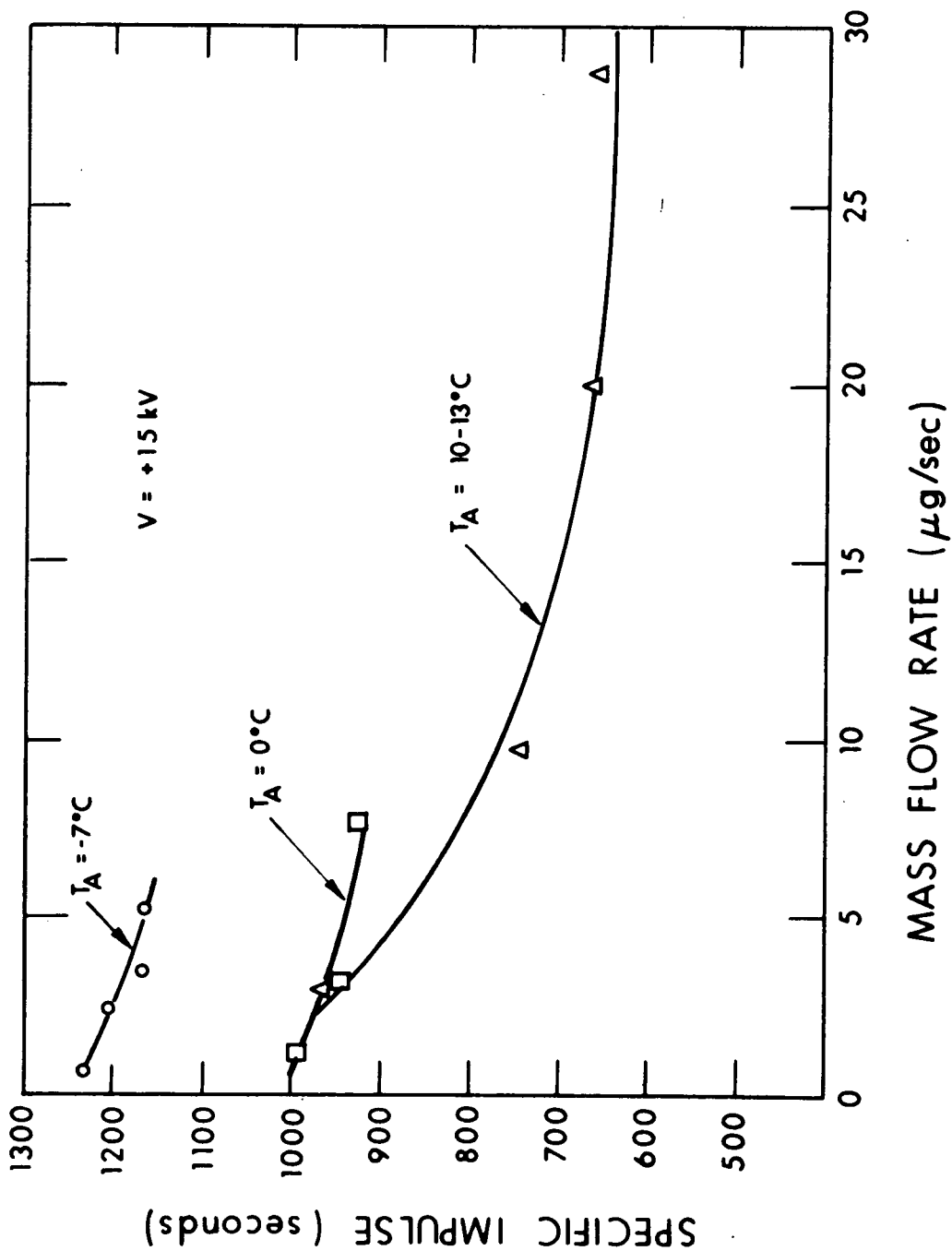
Figure 16. Specific Impulse versus Mass Flowrate at Various Temperatures for 30 gm LiI plus 1 gm LiOH/100 ml Glycerol Test Propellant (Annulus A06, Run 7012-02)

4.2 THRUST VECTORING

Several thrust vectoring studies were performed during the program in addition to the vectoring done during the 1000 hour test. These studies included variations in the deflecting electrode configuration, measurement of beam deflection angles with and without neutralization, examination of beam symmetry by deflecting along two orthogonal axes, and effects on thruster operation when positively biased deflector electrodes were used (as opposed to exclusively negative bias potentials). A method to calculate the amount a beam deflects when the normal beam profile is not preserved was developed. This section begins with a discussion of the scanning detector used to measure beam profiles, the electrode configuration used, followed by discussions of individual tests. The vectoring data from the 1000 hour test is included in Section 5.

Both normal and deflected beam profiles were measured using the scanning collector designed for use in the 2 x 3 ft. vacuum chamber. The probe axis of rotation is located directly above the annulus in an orthogonal plane intersecting the annulus at the tip with the probe sweeping a horizontal arc encompassing approximately 105° at a distance of 8 inches from the annulus as shown in Fig. 17. The three individual curved segments of the collector subtend a total angle of approximately 75 degrees in the vertical plane and could be monitored separately or together. The slot in the front plate of the collector subtends an angle of 1° in the horizontal plane. The schematic diagram of the scanning collector also shows the plate and grid arrangement used to prevent secondary effects on the collector measurements. The scanning collector was swept across the beam using a motorized drive with an electrical signal proportional to the collector position used as the X input to an X-Y recorder. Data was obtained using the current to any or all of the curved collector segments as the Y input.
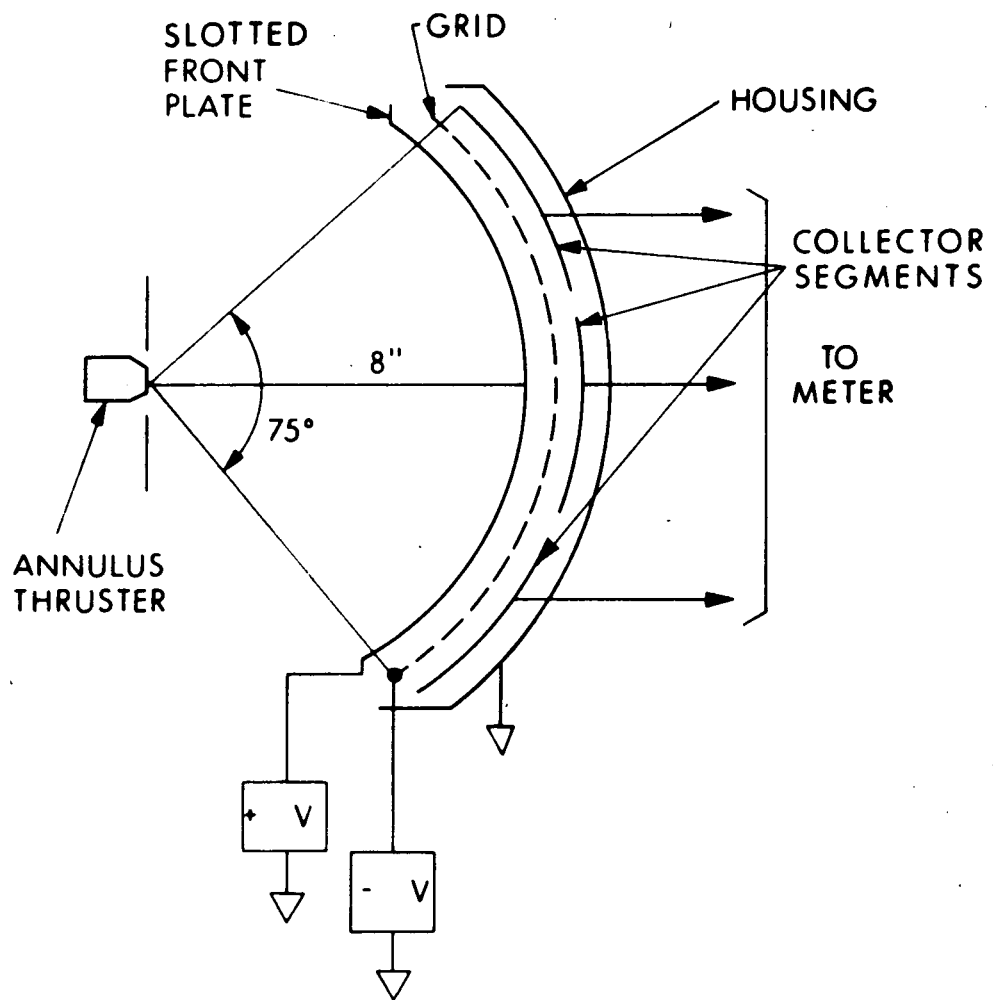
Figure 17. Schematic Diagram of Scanning Detector Probe

The vectoring (outer extractor) electrode configuration is shown in
Fig. 18. The outer extractor is machined into four equal segments from
a 1/8 inch thick stainless steel plate. Gaps between individual segments
are minimized to reduce the effects of high fields at the corners and,
at the same time, maintain a sufficient separation to prevent voltage
break-down across neighboring segments when large deflection voltages
are applied. Using the configuration shown schematically in the figure,
no problems were encountered with drainage currents and electrical break-
down involving the annulus. In operation, the electrodes could be oriented
to provide horizontal or vertical vectoring. Four methods of providing the
required potential differences were examined.

The first method involved holding two of the vectoring electrode segments
(No. 1 and 2) negative but near ground potential and applying a large
negative potential to the other two electrode segments (No. 3 and 4).
Beam profiles were obtained using this vectoring arrangement during Run
7012-04 where net deflection voltages ($\triangle V$) of -2kV and -5kV were used.
For the -5kV deflection voltage (with V_A = 13.6 kV) the peak of the de-
flected beam profile was displaced about 5 to 6 degrees from the normal
beam profile with some distortion from the normal beam profile.

The second method used was to hold three of the electrode segments
(No. 1, 2 and 3) near ground potential and apply a large negative poten-
tial to the fourth segment. Data from Run 7012-05 using this method are
shown in Figs. 19 and 20 where measurements of beam profiles in the normal
and vectored modes were obtained both with and without neutralization.
Figure 19 shows the beam profiles at defecting voltages of 0, -5 and
-7.5 kV (I_A~20 μA and V_A = +15 kV) with no beam neutralization, while
Fig. 20 shows a similar plot with the same parameters when the beam was
neutralized to approximately +80 volts. Note that no significant differ-
ence exists between the two cases, the deflection being ~4° with -7.5 kV
deflection voltage. Since the profile does not change appreciably from
the nondeflected to deflected condition, the deflection angle was estimated
from the peak shift.

1/8 THK. STOCK
316 S.S.

0.650 ± 0.001

45°

2.50

0.050 ± 0.001 GAP

0.650 ± 0.001

1

2

4

3
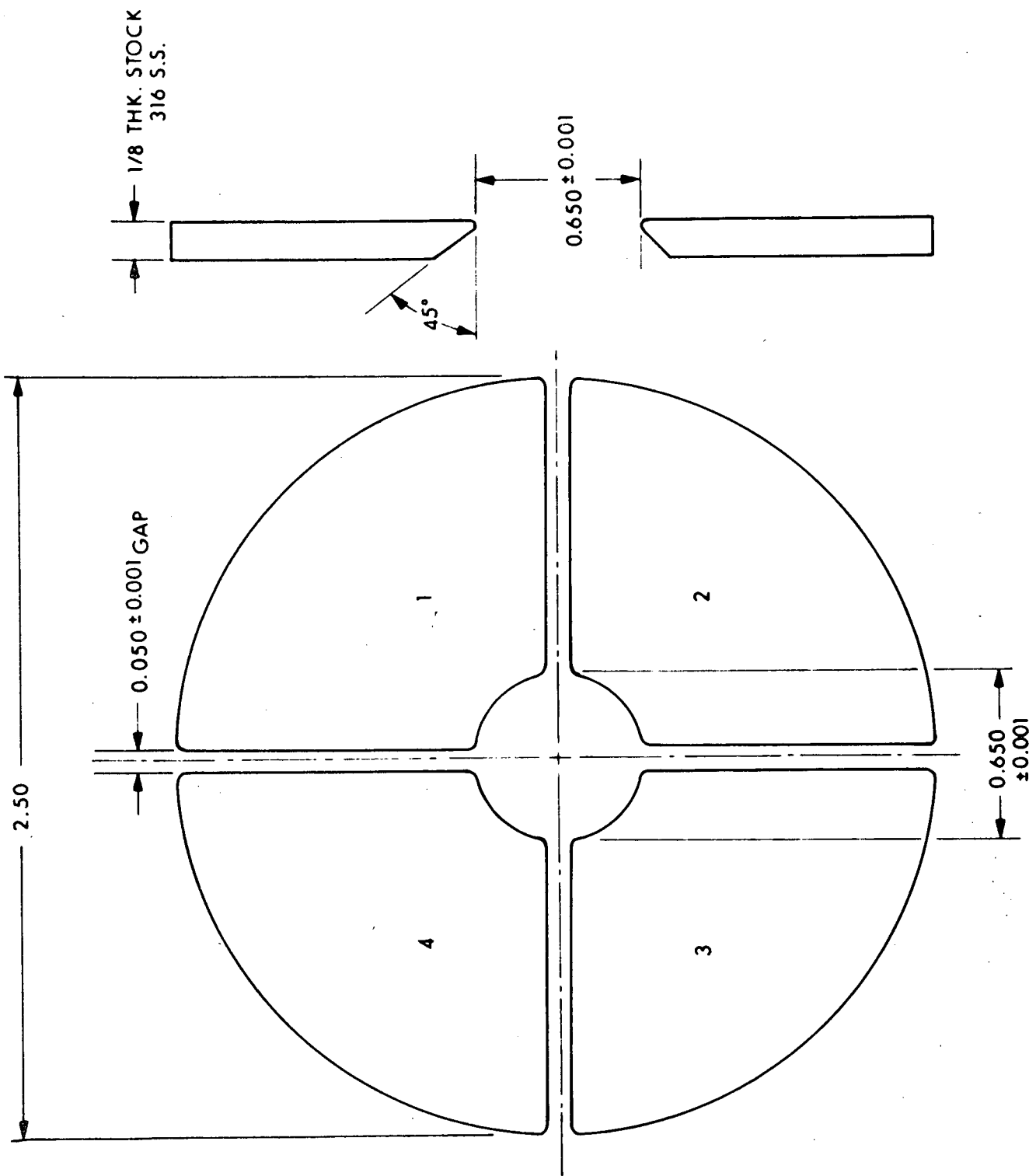
Figure 18. Vectoring Electrode Configuration
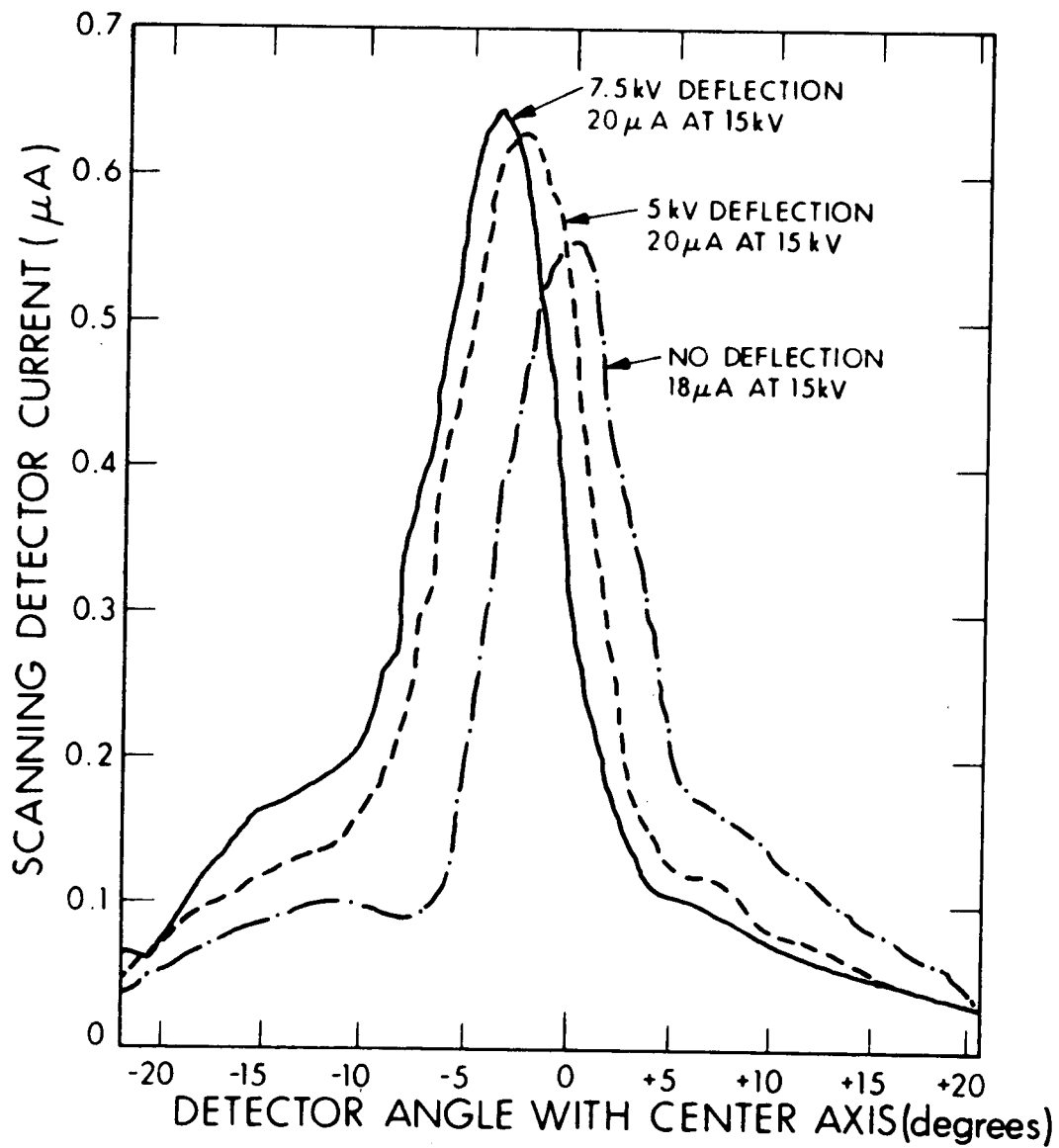
Figure 19. Beam Profiles at Deflecting Voltages of 0, 5, and 7.5 kV with No Beam Neutralization
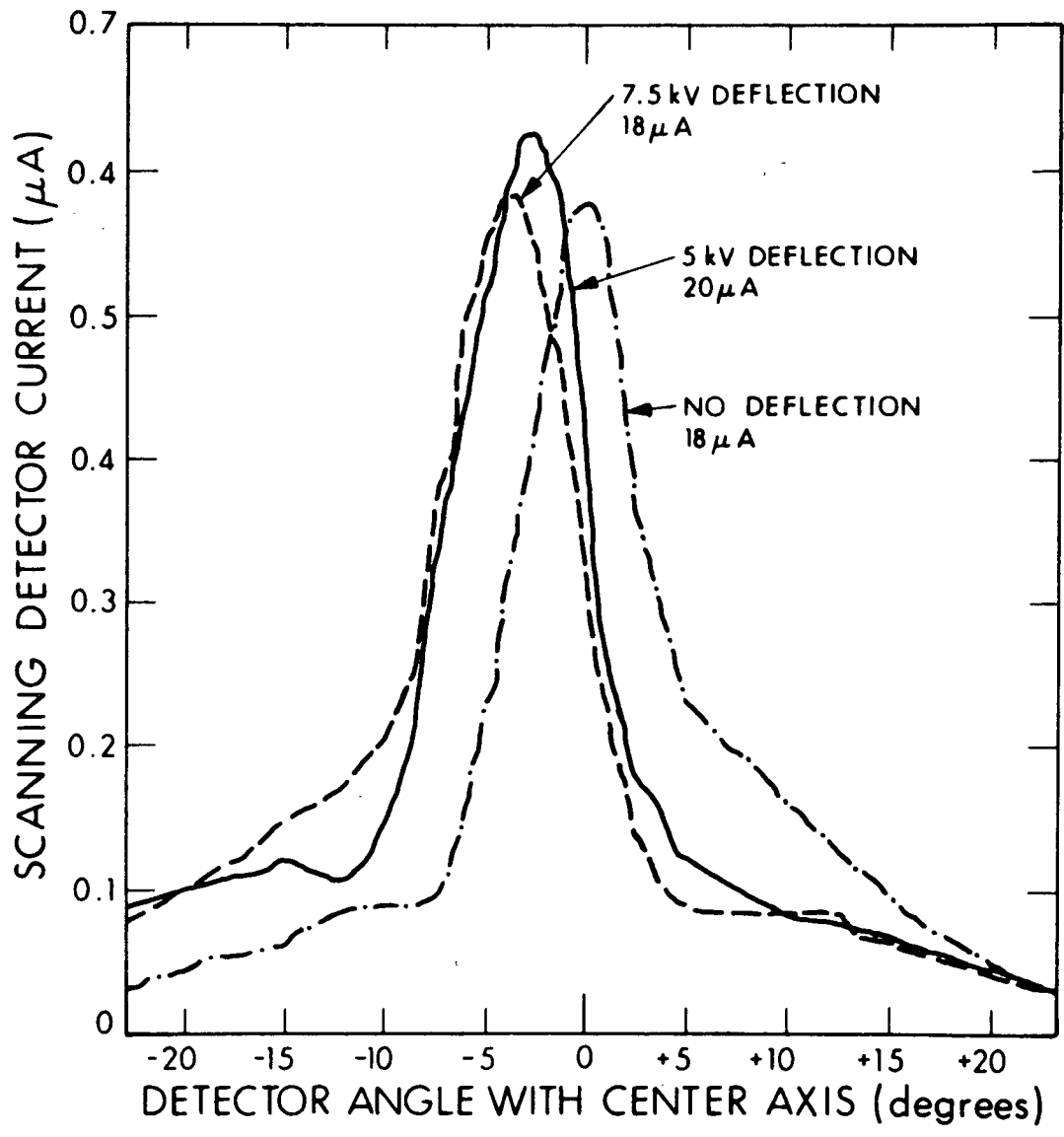
Figure 20. Beam Profiles at Deflecting Voltages of 0, 5, and 7.5 kV with Beam Neutralized to +80 Volts

The third vectoring method used represented a major departure from the first two methods since large deflection voltages of both positive and negative polarity were used. In this method, a large negative voltage was applied to segments No. 1, 2 and 3 and a large positive voltage was applied to segment No. 4. This approach resulted from an attempt to increase the amounts of deflection obtained without applying unnecessarily large deflecting voltage to any one segment. The primary concern was whether electrons from the neutralizer would feed back to the large positive potential region due to the positively biased deflection segment. However, no interaction was observed when the trap electrode was maintained at the proper bias potential. Figure 21 shows both the normal beam profile and the deflected profile for $\Delta V = 10$ kV. All four electrode segments were maintained near ground for the measurement of the normal profile. For the deflected profile, three of the segments were maintained at -5kV and the fourth at +5kV. The change in the beam distribution in the deflected mode is due to this 3:1 asymmetry in deflection geometry. For the condition exhibited in Fig. 21, the amount of deflection can not be estimated by measuring the shift in the peaks. Because of the change in distribution, a more accurate method of calculating the deflection angle was devised and involves the integration technique described below.

Figure 22 is a schematic illustration showing the form of data obtained with a scanning detector probe. The scalar quantity of detector current can readily be transformed into a vector format. In the figure, I_1 and I_2 represent the amount of current contributing to the thrust in the direction θ_1 and θ_2, respectively. We can replace the current I_1 with the vector quantity $\vec{I_1}$ whose magnitude is I_1 and whose direction is determined by the angle θ_1. Therefore, $\vec{I_1}$ can be resolved into its X and Y components and summed over the entire profile according to:
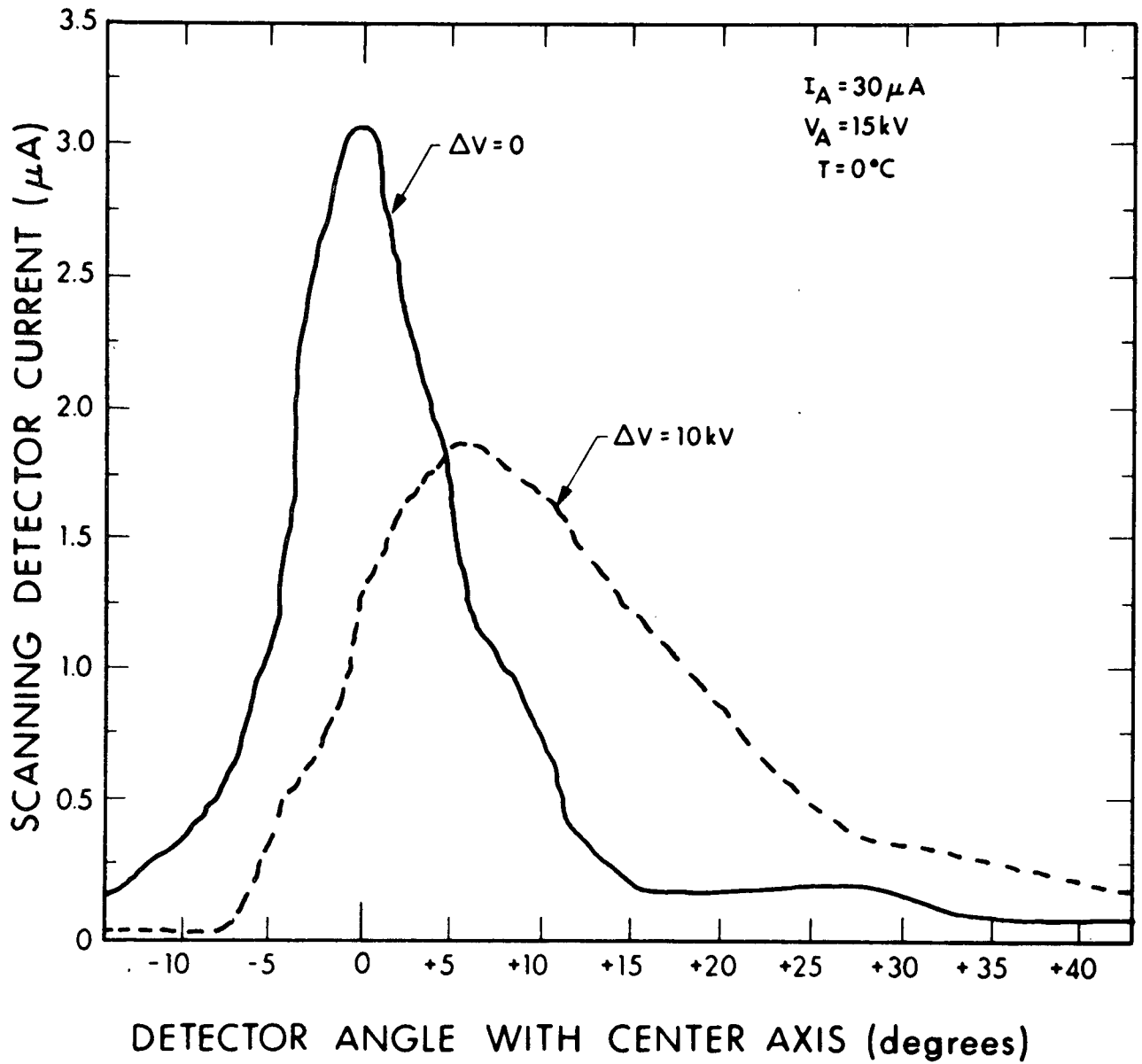
Figure 21. Beam Profiles at Deflecting Voltages of 0 and 10 kV

39330
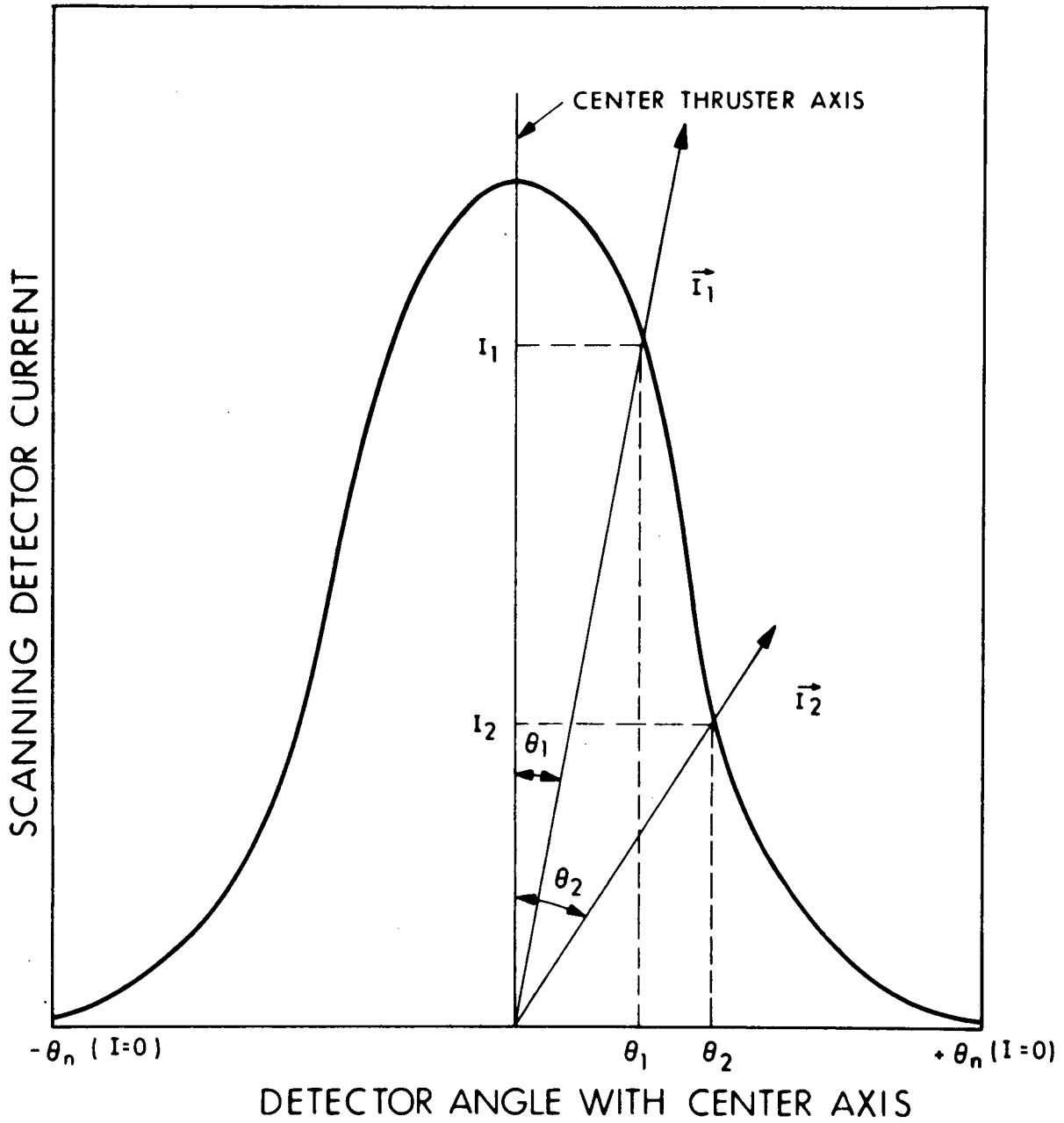
Figure 22. Vector Diagram of Detector Current

$$\begin{array}{ll}
\theta = \theta_n & \theta = \theta_n \\[4pt]
X = \displaystyle\sum f(\theta)\,\sin\theta\Delta\theta; & Y = \displaystyle\sum f(\theta)\,\cos\theta\Delta\theta \\[4pt]
\theta = -\theta_n & \theta = -\theta_n
\end{array}$$

where $I = f(\theta)$. Hence, the direction of the resultant vector is given by:

$$\tan\theta = \frac{X}{Y}$$

When the direction of the central axis is chosen arbitrarily, the net deflection angle as determined from the normal and deflected profiles is:

$$\theta_D = \theta_B - \theta_A = \tan^{-1}\left(\frac{X}{Y}\right)_B - \tan^{-1}\left(\frac{X}{Y}\right)$$

where θ_B is the net deflection angle determined from the deflected profile and θ_A is the angle determined from the normal profile. For perfectly symmetric profiles, only the differences in the peak angle are necessaary to determine the deflection.

The data in Figure 21 was used with the above analysis to determine the amount of deflection. Each profile was divided into sub-intervals of $\Delta\theta = 1.5^\circ$ and numerically integrated. For this case, θ_A was determined to be $2^\circ 26''$ and θ_B was $11^\circ 26''$. Therefore, the amount by which the beam was deflected is given by:

$$\theta_D = 11^\circ 26'' - 2^\circ 26'' = 9^\circ.$$

The fourth method was similar to the third method but with two segments (No. 1 and 3) held negative but near ground potential while a large negative voltage was applied to segment No. 2 and a large positive voltage was applied to segment No. 4. In this way, the asymmetry observed in the third method was avoided and considerably less distortion from the normal profile was obtained when vectoring. This method was chosen for incorporation into the thruster configuration for the 1000 hour test and performed exceptionally well throughout that test. Typical beam profiles obtained with this vectoring method are shown in Section 5 of this report.

4.3   NEUTRALIZER STUDIES

Important characteristics of a neutralizer are efficiency, lifetime, and "coupling". Good coupling (i.e. the ease with which the neutralizer injects its electrons into the "ion" beam) is desirable for it means low beam potential and minimal thrust loss. The efficiency of electron emitters, known as the "heat factor", is measured in terms of electron emission per watt of neutralizer heater power and is usually important because of the power limitations encountered on spacecraft. Lifetime of a neutralizer is important since the colloid thruster system lifetime is limited by the neutralizer lifetime. Unfortunately, the requirements of high efficiency, long life, and good coupling can conflict with each other. Efficiency and long life could require compromise on emitter location while coupling and efficiency could require compromise on emitter size.

For the requirements of this program, it was decided to optimize lifetime and coupling with little effort to achieve efficient operation in terms of the power used to generate the electrons. The neutralizer filament used throughout the program was a 1.5 inch length of 0.007 inch diameter tantalum wire operated at about $2000^{\circ}K$. This emitter configuration was selected on the basis of emission capability and demonstrated reliability in both the ATS microthruster system and SERT II emissive probe systems.

The coupling to the ion beam attained with such thermionic emitters is dependant upon the emission capability as well as the location of the emitter with respect to the ion beam and the thruster electrode configuration as well as the electrode potentials. To examine the variation of the coupling with these parameters, two sets of neutralizer configurations consisting of three emitters mounted ~120° apart were tested in conjunction with the performance mapping of Annulus A10. For the majority of the data obtained the nominal annulus voltage was 15 kV and the nominal annulus current was ~60 μA with low (<1 μA) extractor and trap electrode currents.

For the initial series of tests, two of the neutralizer emitters were mounted a distance of one inch downstream of the trap electrode and the third neutralizer emitter 1/2 inch downstream of the trap electrode, with all the emitters located so that the trap electrode served as a radiation shield between the hot emitter and most of the annulus. In addition, one of the two neutralizer emitters located one inch from the trap electrode was shielded from the trap electrode potential using an additional electrode which also acted as a radiation shield to prevent excessive heating of the emitter. This shield electrode was grounded through a current meter.

The degree of neutralization or the effectiveness of the coupling of electrons from each neutralizer with the beam was determined by electrically isolating the segmented collectors and the TOF collectors from ground and measuring the voltage between the collectors and ground using a high impedance voltmeter. This collector "floating voltage" (V_c) is defined as beam potential. The values obtained ranged from > +1kV with the emitters cold and from +20V to +140V with an emitter at ~2000°K. As expected, the coupling of electrons from any of the neutralizer configurations to the beam was dependent upon the potential of the trap electrode, the position and shielding of the emitter, and the emitter temperature. Voltage on the trap electrode greatly suppressed electron emission from the two unshielded emitters with this effect reduced for

the shielded configuration. Typical variation of the beam potential as a function of trap electrode potential is shown in Fig. 23 for the shielded emitter configuration. An extrapolation of these data indicates a beam potential of zero should occur for a trap electrode voltage of about -30V. However, it is impractical to operate at voltages more positive than -100V since the trap effectivenss is reduced.

For the next series of tests, the shielded ("control") emitter was not changed and two other electron emitters (also shielded from the trap electrode) were installed as shown in Fig. 24. Note that the emitters were located so that one was in close proximity to or in the beam and could "see" most of the annulus, one was located just out of the beam and was shielded from "seeing" most of the annulus by the trap electrode, and the third emitter was located a considerable distance from the beam and was completely shielded from the annulus.

In general, the lowest beam potentials were obtained for the electron emitter located the furthest from the beam i.e. No. 3,   so this type configuration was chosen for the 1000 hour test. Typical values of beam potential obtained at V_A = +15 kV, V_{IX} = -5.5 kV, V_{Trap} = -200V, and for an emitter heating current of 2.0A were:

Configuration	Beam Potential
1	+64 V
2	+48 V
3	+32 V

The variation of beam potential with the annulus current was also examined. Typical results are shown in Fig. 25 for a neutralizer (emitter) heating current of 2.0A. Note that increasing beam current produces a decrease in beam potential over the range of interest to the 1000 hour test.
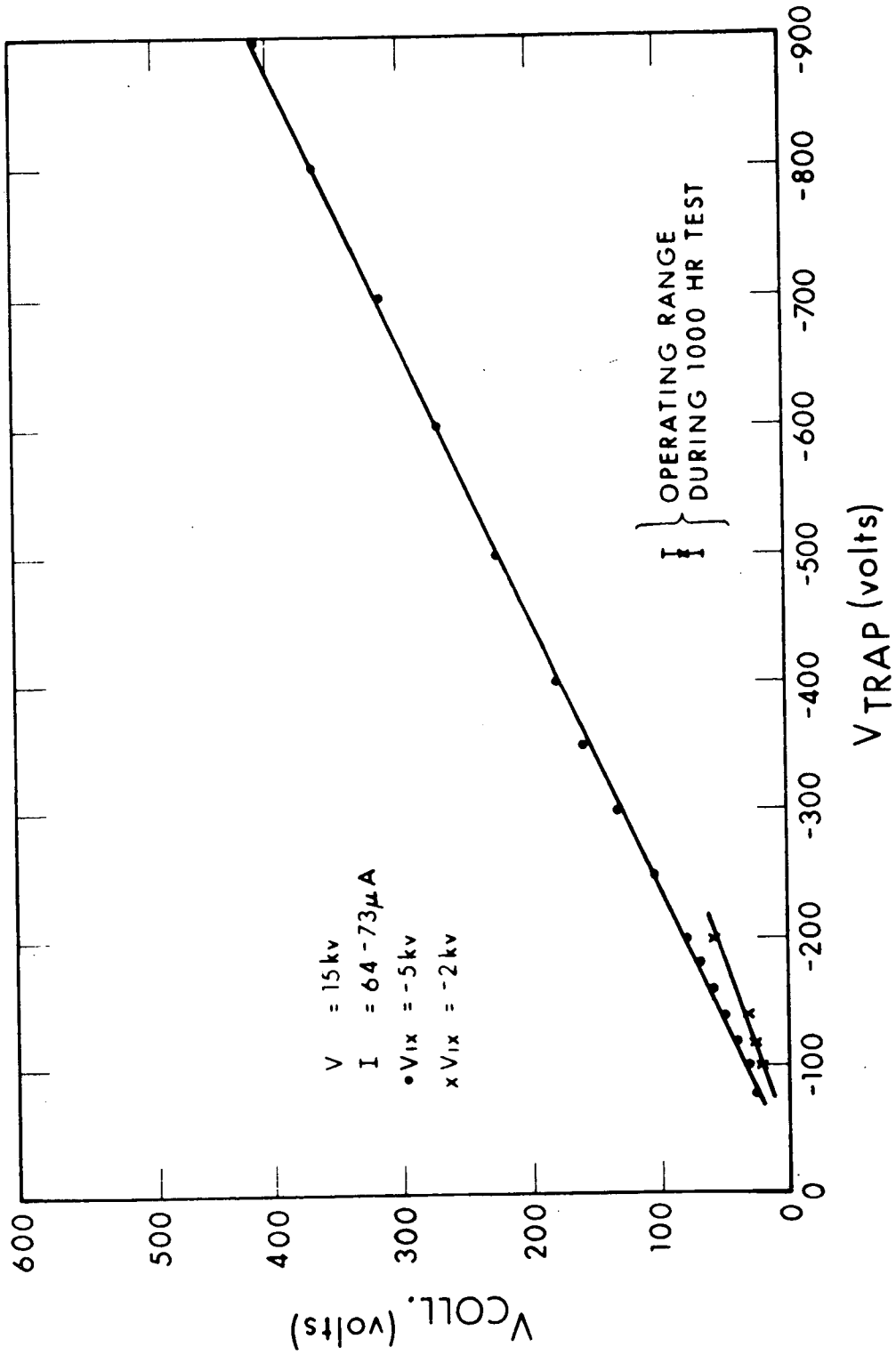
Figure 23. Variation of Floating Collector Voltage (V_{Coll}) versus Annulus Trap Electrode Voltage (V_{shield})
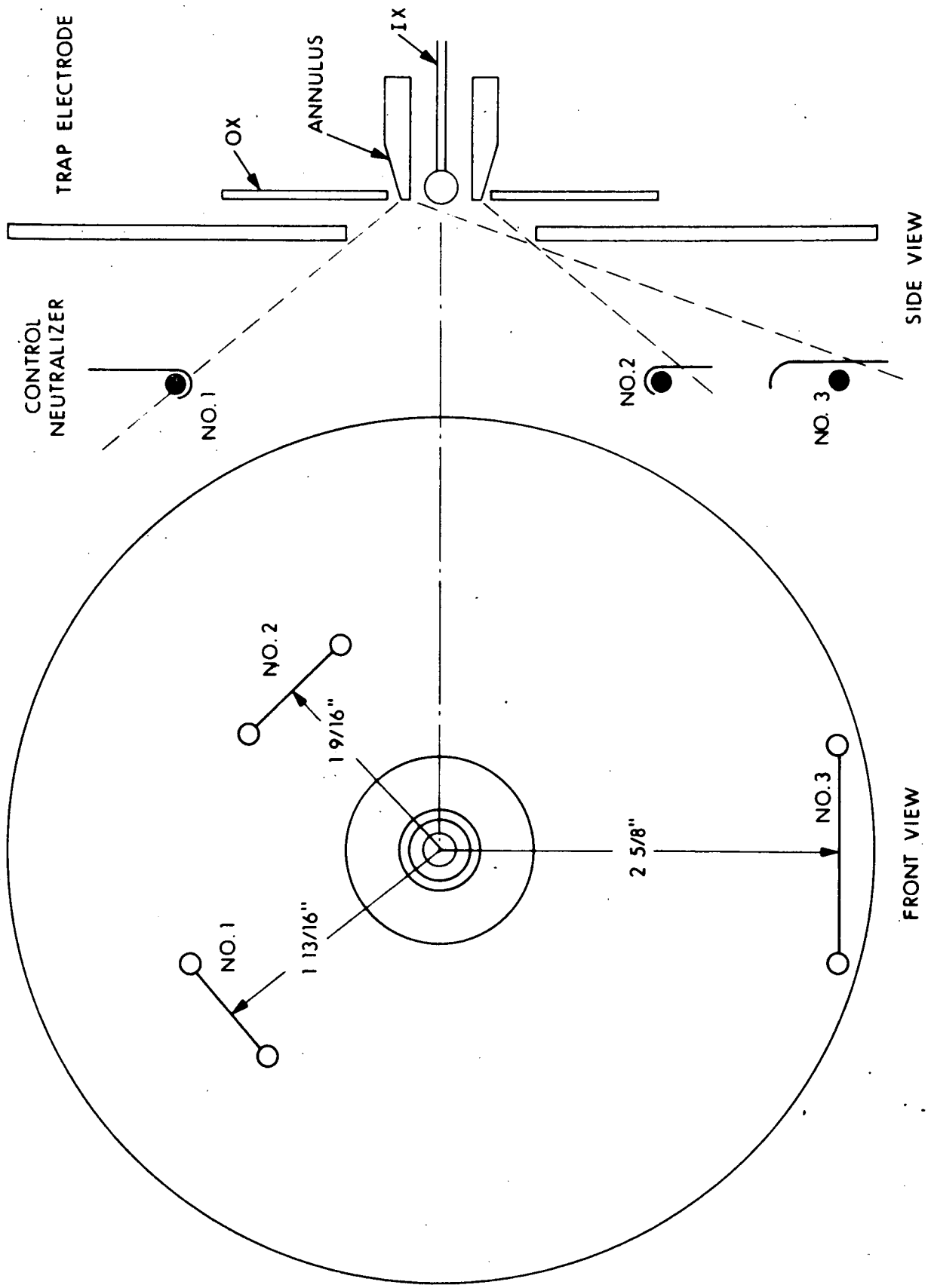
Figure 24. Neutralizer Configurations

38731
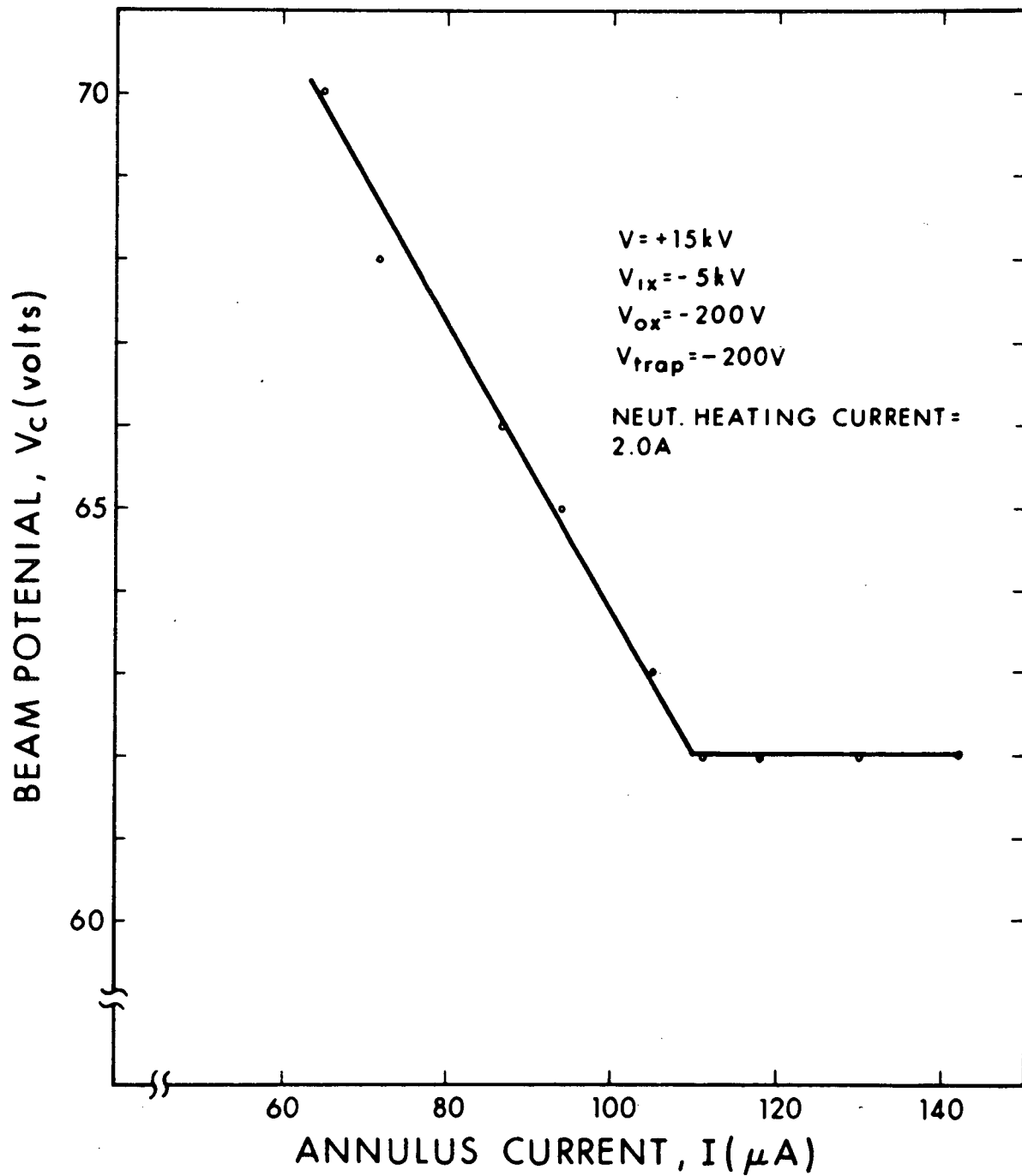
Figure 25.   Beam Potential as a Function of the Annulus Current

The variation of beam potential with annulus voltage is shown in Fig. 26. The data plotted are not at constant values of annulus current and are therefore somewhat distorted but the general tendency can be seen. Since the beam tends to converge with increased voltage, the beam potential appears to decrease with increasing beam current density.

Further tests showed improvements in coupling were possible by moving the emitter further downstream from the thruster. Based on these tests and upon the desire to keep the emitter close to the thruster, the emitter for the 1000 hour test neutralizer was located two inches from the trap electrode.

4.4   120 HOUR TEST

A colloid thruster equipped with a neutralizer and a segmented extractor (used to perform beam vectoring in two orthogonal directions) was operated operated for 120 hours continuously. This test was performed as part of the overall preparation for the 1000 hour test. The specific objectives for this test were to examine the following: a new tapered annulus emitter design (T03); test the performance of lithium iodide doped glycerol propellant (F21); examine the total thruster operational stability; determine the thermal equilibrium associated with neutralizer operation and evaluate the new instrumentation installed for use on the duration test.

During the first 50 hours of operation, beam vectoring studies and performance mapping were accomplished. Thruster operational performance is displayed in Fig. 27, where thrust and specific impulse are plotted against mass flow rate. The arrows in the figure indicate the level (15 kv) chosen for thruster operation over a period of approximately 70 hours. The annulus current at this level was 60 µA corresponding to a
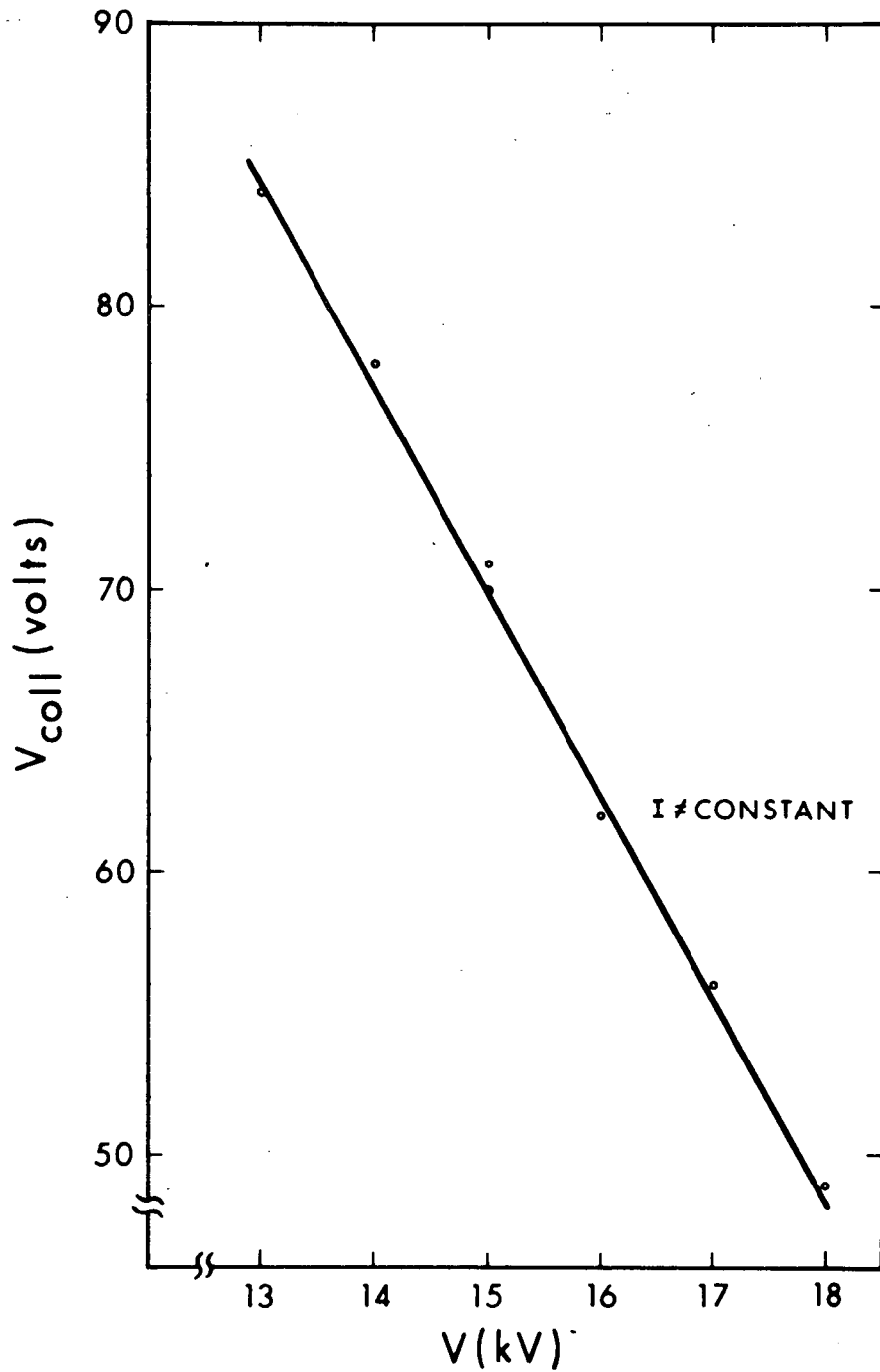
Figure 26. Variation of Beam Potential with Annulus
Accelerating Voltage
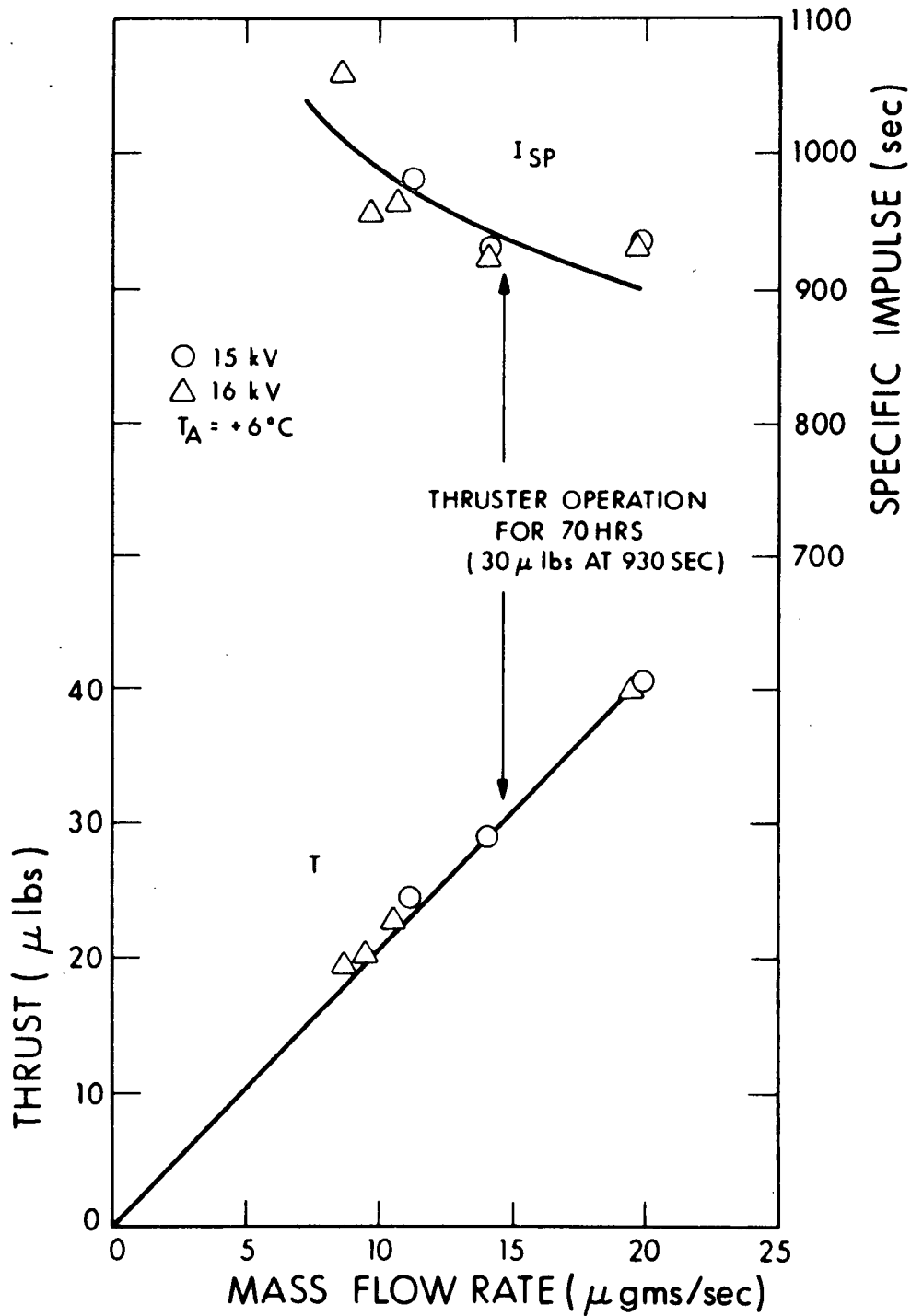
Figure 27. Thruster Performance for Annulus Emitter TO3, Run 7012-07

thrust of 30 μlb and a specific impulse of 930 seconds at a mass flow of 14.5 μgms/sec. The thruster was operated with neutralization where the neutralizer emission current under the operating conditions described above was 67μA and the floating collector potential was +90 volts. In the cryogenic liner environment, with no external heat sources other than radiation and conduction through insulating supports from the neutralizer assembly, the thruster reached an equilibrium temperature of +6°C. Performance stability of the emitter propellant, neutralizer and thermal environment was excellent.

Beam vectoring and profile studies were performed early during the 120 hour run. The beam profile was examined when the collector system was grounded and compared with the profiles measured as a function of floating collector voltage when the beam was neutralized. The results of these tests indicate that the central beam profile is not affected appreciably.

Previous vectoring studies involved deflection in the horizontal plane. During this test, the beam was deflected vertically and detected using the three collector segments of the scanning collector shown in Fig. 17 of section 4.2. Although the resolution of the detector is less when measuring vertical deflections (determined by the 25° segments), vertical deflection (downward) was clearly verified. It was observed that the current to the top segment decreased to zero, the peak current to the center collector decreased by about a factor of three, and the peak current to the bottom collector increased by about a factor of three. From symmetry arguments, the amount of beam deflection in the horizontal plane, measured with excellent resolution can be assumed for the vertical plane when identical deflecting voltages are applied.

4.5   EMITTER DEPOSITS

Concern about the formation mechanism of emitter deposits experienced at other laboratories prompted an investigation into the cause of the black, tar-like deposits. Since this problem had been eliminated in Phase I,

C.2

experiments were designed to show cause and effect. Two experimental approaches were pursued; the first was to examine the possibility of thermal decomposition of the glycerol based propellant, and the second was to use an energetic electron beam to simulate the effect of electrons backstreaming to the emitter resulting the decomposition of the propellant.

The thermal decomposition experiment, performed by heating of the propellant from ~30°C to >400°C at a pressure of ~50 microns, indicates that thermal effects alone do not produce any black deposits since the glycerol rapidly evaporated at the high end of the experimental temperature range leaving a grey residue. This residue (possibly NaI salt) was amorphous appearing and was quite hydroscopic.

The electron beam experiment was performed using the arrangement shown in Fig. 28 and consisted of an electron gun, a deflection magnet, and a target. The electron gun was operated to give a 250μA, 1 keV electron beam to the target. The magnet was used to deflect the electron beam onto the target and thereby keep any thermal radiation from the electron gun from reaching the target. The target was electrically isolated and thermally controlled so that the electron current could be directly measured and the target temperature could be maintained constant. After ~15 minutes of bombardment by 250μA, 1 keV electrons produced a color change in the glycerol based propellant to give a black, tar-like appearance.

From these experiments, the black, tar-like deposits observed on emitters are believed to be produced by propellant decomposition caused by electron bombardment. The electrons responsible for this effect could be backstreaming electrons from the neutralizer or collector surfaces.
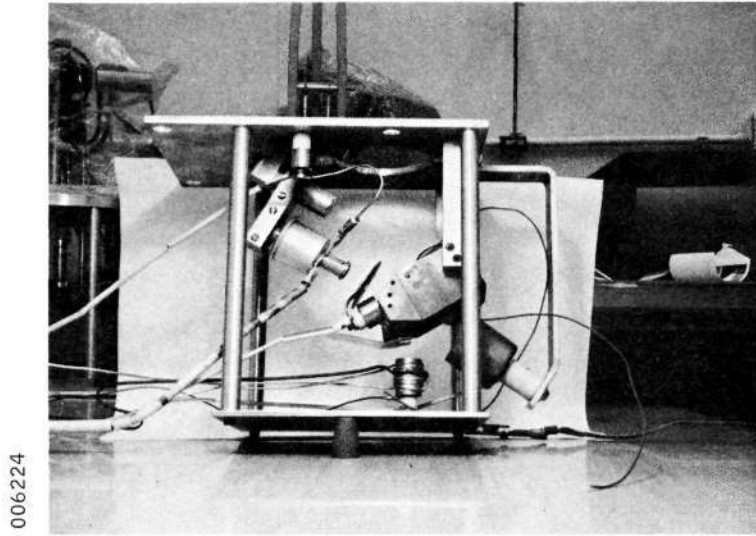
Figure 28. Photograph of Apparatus to Produce
Tar by Electron Bombardment

From these experiments and from examinations of collector and grid surfaces, both exposed and protected from direct impingement by the beam, it is felt that an optimization of the shielding of the annulus from back-streaming electrons will provide the best conditions for minimization of this type emitter deposit. Note, however, that this shielding will not eliminate the backstreaming of such deposit material from the collector which may be significant for long duration tests in the laboratory. However, in the environment of outer space, where the beam termination processes do not involve a physical collector surface, such effects should be negligible.

SECTION 5

1000 HOUR THRUSTER TEST

A neutralized thruster was operated for 1000 hours to determine long
term stability, reliability and to examine possible degradation trends
and lifetime. The thruster system and measurement techniques used in
the test were based upon the previous work in Phase I and the first
part of Phase II.

The test was extremely successful with no difficulties encountered,
absolutely no sparking throughout the test period, and no degradation
in performance. Vectoring was performed periodically with no difficult-
ies in operation. Termination of the test was intentional at 1023 hours
in order to examine the thruster condition. No erosion of the emitter
edge had occurred and no tar deposits were observed.

5.1 THRUSTER SYSTEM

The basic thruster that was tested, shown schematically in Figure 3 of
Section 3.2, consisted of: (1) a platinum/iridium tipped annulus,
(2) a electron trap electrode, (3) a spherical inner extractor, (4) a
segmented outer extractor used in periodic thrust vectoring, (5) lithium
iodide doped glycerol propellant, and (6) two neutralizer filaments.
These various components are discussed below and photographs of the
thruster are shown in Section 5.6 (Fig. 40 and 41 in Section 5.6).

Several annular emitters with platinum (90%) iridium (10%) edges were
constructed for possible use in this test. The selection of the emitter
used in the test was based on a comparison of photomicrographs showing
the edges at 100 times enlargement and upon the gas flow permeability of
the completed annulus. Photomicrographs of the emitter selected (PT05)
are shown in Figure 29. These pictures, showing portions of the emitter
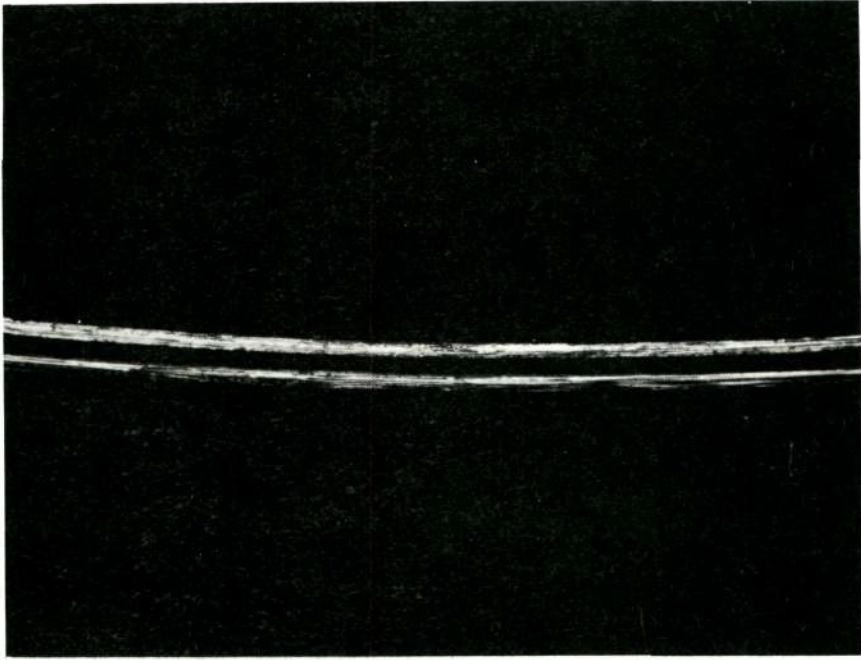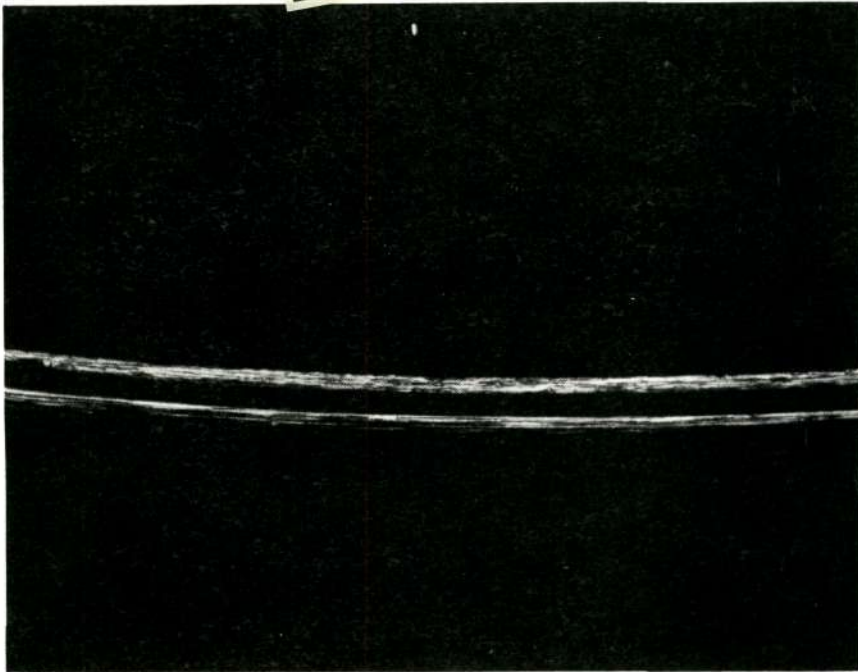
006264

Figure 29.   Photomicrographs (X100) of Annulus Emitter
(PT05) before 1000-hour Test

57

edges located 45° apart, illustrate the condition of the emitter before operation The normalized permeability of the annulus selected was 6.0 which was desirable based upon data obtained in previous tests.

An essential component of the thruster assembly, important for maintaining stability, is the electron trap electrode. The trap electrode concept was first applied at our laboratory after investigations proved that backstreaming electrons caused glow discharge phenomenon, inner extractor currents, annulus heating, and tar deposits. A trap electrode therefore was included on our thruster since the negatively biased outer and inner extractors only minimize and do not eliminate backstreaming electrons. Basically, the trap electrode used for the test was a circular plate with an aperture large enough to prevent beam impingement (1.25 inch diameter) and mounted 0.25 inch beyond the plane of the outer extractor. This trap electrode was operated at -500V throughout the test.

The inner extractor used for the test was spherical having a 0.313 inch diameter designed to eliminate high field breakdown. In addition to having a desirable focusing effect, the negative potential of -2kV at the inner extractor significantly reduced the penetration of the annulus field beyond the trap electrode. This served to enhance the shielding of the thruster system.

The segmented outer extractor configuration described in Sec. 4.2 was used during the test to perform the required thrust vectoring. The soundness of using this configuration was substantiated by the successful vectoring operatings periodically performed throughout the 1000 hour period. The effectiveness of the trap electrode in preventing electrons originating from neutralizer operation or from collector surfaces in the chamber from reaching the annulus/extractor plane permitted the use of positive voltages on these electrodes during beam vectoring. As a result, lower voltages (both positive and negative) could be utilized for vectoring than would have been possible without the trap

electrode. Results from the beam vectoring exercises are discussed
in Section 5.5.

The propellant used consisted of a mixture of 30 gms lithium iodide
dissolved in 100 ml glycerol. Lithium iodide was selected as the ionic
dopant for glycerol based on our establishment of the superior spraying
characteristics of this propellant combination. For the same amount of
dopant dissolved in equal volumes of glycerol, a higher specific impulse
can be achieved using lithium iodide compared to sodium iodide under
identical thruster operating conditions (Sec. 4.1). In addition to the
experimentally determined advantages of using lithium iodide, analytical
investigations of propellant behavior (Appendix VI) predicted superior
performance of lithium iodide over sodium iodide. The performance of the
lithium iodide propellant during the test was excellent and further justi-
fied this choice of propellant.

The neutralizer assembly consisted of a 0.007 inch diameter tantalum
filament with a grounded shield. The neutralizer shield was necesary to
prevent the electric field from the negatively biased trap electrode from
suppressing the filament emission current. A redundant filament was avail-
able as a backup, however, the one neutralizer operated satisfactorily for
the duration of the test.

5.2   INSTRUMENTATION AND DATA PROCEDURE

The 1000 hour test was performed using the same vacuum facility and much
of the instrumentation used during the component development stages of
the program. Thus the standard TOF configuration was used (shown sche-
matically in Fig. 2) despite the obvious disadvantage, from a duration
test standpoint, of coating the emitter edge with backscattered material
because of terminating the colloid beam a distance of only 0.5 meter
from the thruster. It was felt that maintaining the collector at a dis-
tance which has given reliable and reproducible TOF data was the more
important consideration since we were confident that electrons from the

neutralizer could not reach the thruster and decompose material
backscattered from the collector.

The test facility had several logic relays included as part of the
interlock system which is part of an alarm system. These include pro-
visions for emergency power generation as well as interlocks relating
to annulus and extractor performance levels. A redundant neutralizer
system which would automatically activate another neutralizer in the
event of the failure of a neutralizer was also included.

The principal additions to the instrumentation for this test were
meters and recorders for use in continuously monitoring several
thruster performance parameters. The recorders were of the sampling
type, giving a printout approximately once a minute per channel. The
parameters continuously recorded in this way included:

V,	Annulus Voltage
I,	Annulus Current (at power supply)
V_{IX},	Inner Extractor Voltage
V_{Trap},	Electron Trap Electrode Voltage
V^+, V^-	Deflection Voltages (Monitored only when vectoring)
P_F,	Feed System Pressure
P_{VAC},	Vacuum System Pressure
V_c,	Floating Collector Potential
I_N,	Neutralizer Emission Current

In addition to continuously recording these parameters, data was manu-
ally recorded on a periodic basis including those times when TOF or
other significant events were examined (such as beam vectoring). The
manually recorded data included some of those parameters which were
monitored continuously such as V, I, P_F, P_{VAC}, V_c, and I_N. Other
manually recorded data were the annulus temperature (T_A), inner extractor

current (I_{IX}), trap electrode current (I_{Trap}), and the currents to the individual outer extractor segments (I_1, I_2, I_3, I_4). The manually recorded data point frequency changed as the test progressed, varying (on the average) between about one data point every two hours for the first 120 hours, to one data point approximately every six hours after 200 hours.

TOF data was taken at the same time as many of the manually recorded data points during the first 120 hours. The TOF frequency was then reduced to approximately one every four hours between 120 hours and 300 hours and after 300 hours, it was further reduced to 12 hour intervals. TOF data was obtained in the conventional way of recording the current decay to the TOF collector after pulsing the annulus voltage to ground. The current decay was displayed on an oscilloscope and recorded on film with subsequent evaluation using a computer program. Hand calculations were also performed at the time the TOF data was obtained to aid as a basis for maintaining the desired operational levels. For this test, the automatic Data Acquisition System (DAS) was not used as the long term reliability had not been demonstrated.

The vacuum facility and instrumentation functioned well over the 1000 hour test period. The only problems encountered during the test were instrumental however. During the test, it was necessary to change annulus current (I) meters once and to have an oscilloscope repaired as the cooling fan motor failed causing the oscilloscope to overheat with subsequent deterioration of scope performance. The deterioration appears to have primarily affected the RC characteristics which were then reflected on the tail of the TOF traces obtained.

5.3 PERFORMANCE OF 1000 HOUR TEST

The stable performance without any signs of degradation was the significant achievement of over 1000 hours of continuous operation with a single emitter annulus thruster. The data clearly shows the excellent stability of thruster operation with reliable thruster performance indicated by smooth operation completely free from emitter and/or electrode arcing or glow discharges of any kind. Absence of arcing was attributed to careful thruster conditioning by extensive outgassing before the test was initiated and to thruster design.

The thruster operated at performance levels near the performance specifications of the program. The average performance parameters based on 115 data points taken periodically over 1000 hours operation are listed below:

Average Values

$$I = 64.8 \ \mu A$$

$$V = 15.2 \ kV$$

$$I_{sp} = 1160 \ sec.$$

$$T = 24.8 \ \mu lbs$$

$$q/m = 6.82 \times 10^3 \ coul/kg$$

$$\dot{m} = 9.81 \ \mu g/sec$$

$$\eta = 63.1\%$$

Performance and control variable data are shown in Fig. 30, where the thrust (μlbs), current (μA), specific impulse (seconds), emitter voltage (kV), and feed system pressure (Torr) are plotted against time (hours).
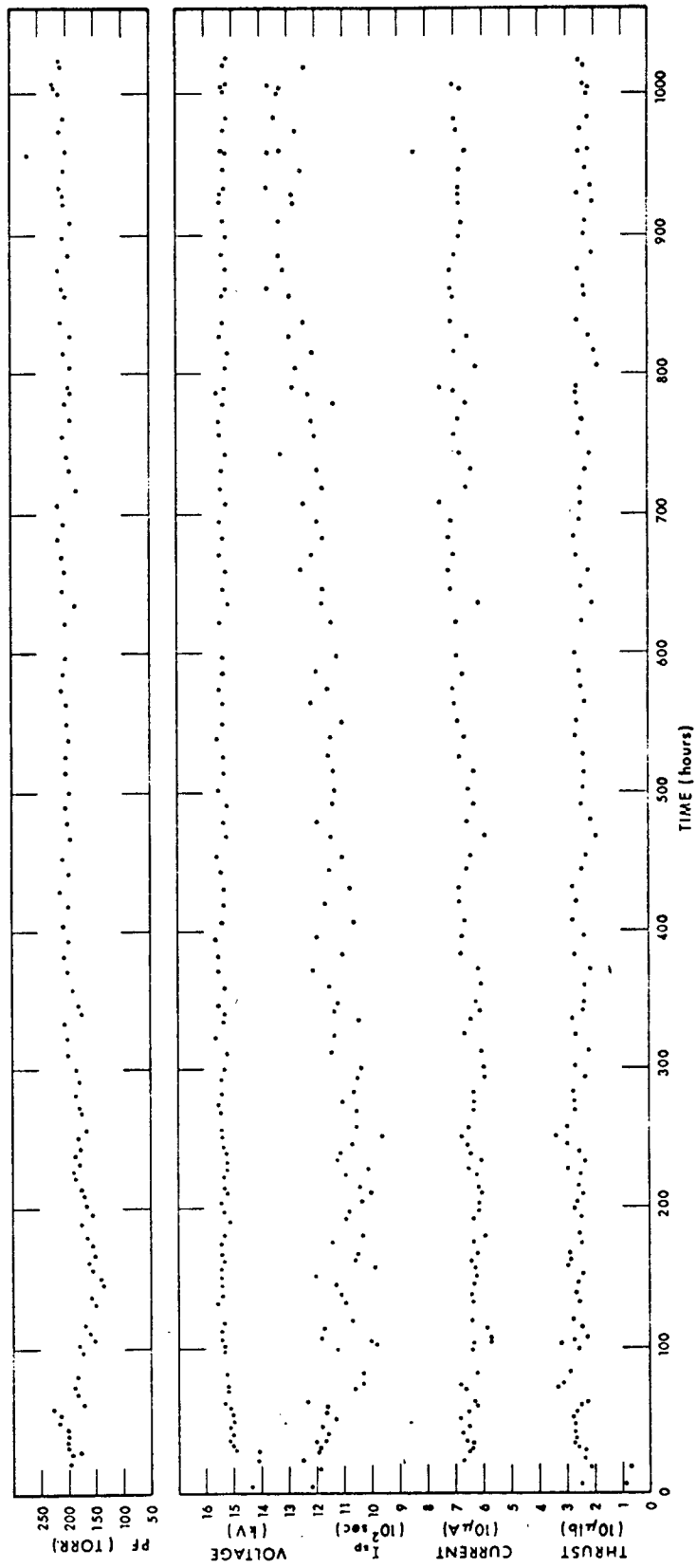
Figure 30. Performance Data as a Function of Time for 1000-hour Test

39906

The data shown reflects the excellent thruster stability with those fluctuations observed primarily the result of environmental changes external to the vacuum system. Examination of the data shows no tendency toward thruster degradation. Fluctuations in the emitter voltage were due to variations in line voltage. Variations in the mass flow rate did produce systematic scatter which was primarily due to feed pressure changes and emitter temperature changes. Adjustments in feed pressure were periodically made to offset a small pressure leak in the feedline. This variation is seen in the feed pressure data in Fig. 30. The emitter temperature which varied between -5 and 5°C showed a diurnal variation which was directly correlated with the changes in room temperature that occurred between day and night. Thus most of the data scatter is directly attributed to the environmental changes which were observable because of the stability and reliability of the emission characteristics of this annular emitter. This scatter could have been reduced by using more sophisticated flow regulation techniques than used in the present test. Complicated normalization techniques to account for the mass flow rate variation with temperature have been used in reporting life time test data at another laboratory (Ref. 6), but the overall stability achieved during the present test was so good that it was not even obscured by this systematic scatter.

The performance during the 1000 hour period is summarized in Figure 31 which shows the thrust and specific impulse as a function of $\dot{m}$. The data being a representative part of all the data extends over a narrow range of $\dot{m}$ (7 to 12 μg/sec.) making it difficult to precisely determine the charge generating index (k_o) and the specific perveance index (P). Two theoretical curves are shown both with a value of k_o = 0.8 (coul/kg-V). The upper curve is for $P = 24 \times 10^{-13} \left(\dfrac{A^2 - kg}{coul-V^3} \right)^{1/2}$ and the lower for

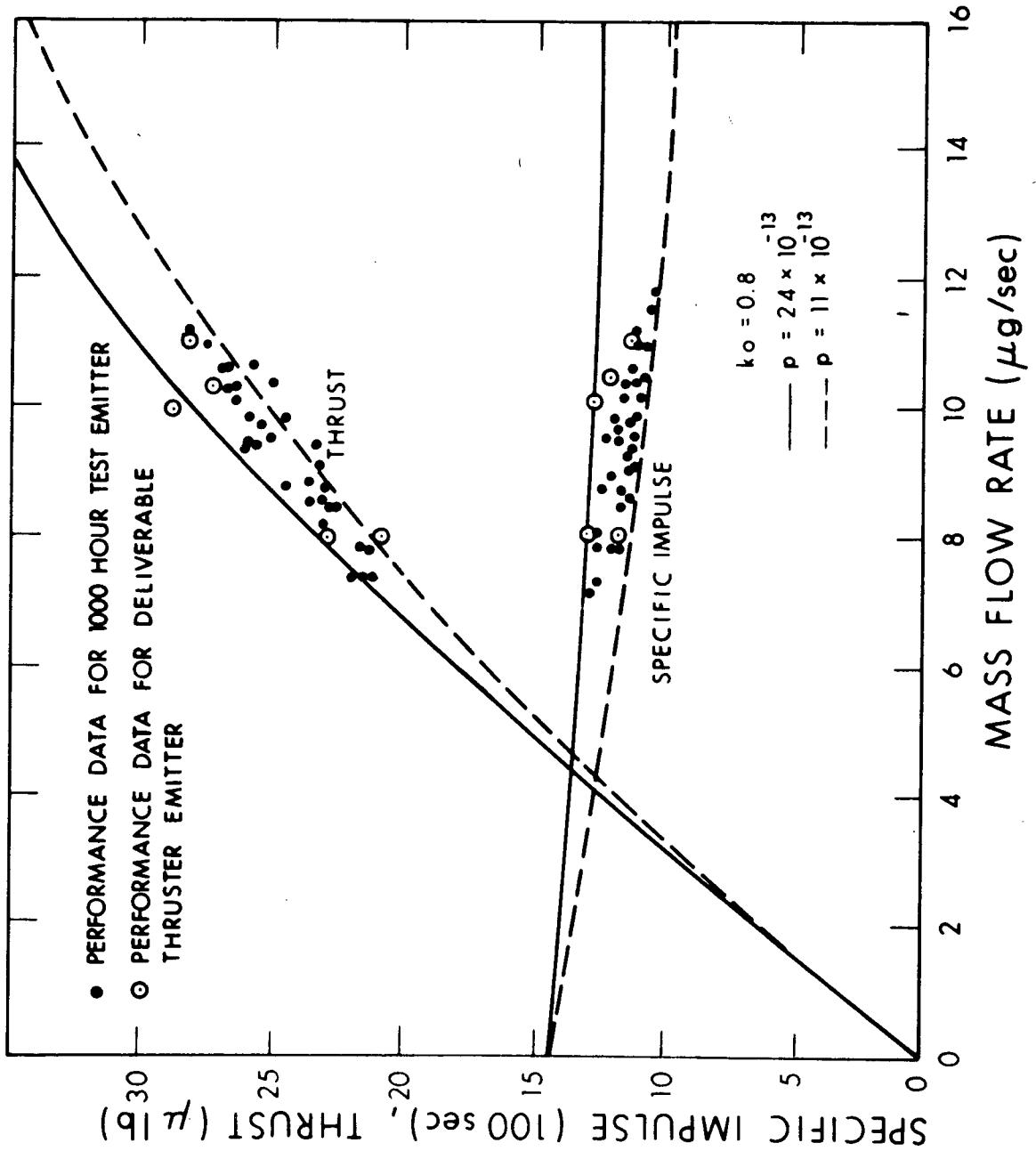$P = 11 \times 10^{-13}$. These curves were calculated using Eqs. 1, 2, 5 and 6 (Section 2.2).

Figure 31. Performance Data for 1000-hour Test

The encompassing of the data points by the two theoretical curves shows that a part of the data scatter is systematic in that the average change in thrust and average change in specific impulse are analytically related to a change in $\dot{m}$. Furthermore, at a given value of $\dot{m}$, the higher performance data occurred toward the end of the run as seen in Figure 30 where the specific impulse increased with no change in average voltage or feed pressure. This change is reflected in Figure 31 for both thrust and specific impulse, where the lower data points occurred early in the run and higher ones occurred toward the end of the run. The value of P therefore increased to reflect the enhanced performance. This could be due to more complete wetting of the emitter tip. It could also be construed that this annulus had a run-in period which was appreciably longer than 1000 hours and would therefore not show any degradation until well after the run-in period. Based upon this performance and complete lack of erosion observed at the termination of the test the lifetime could be extrapolated more than order of magnitude in time. In addition the increase in performance could, in another 500 to 1000 hours, result in specific impulses close to 1500 sec at thrust levels above 30 μlb.

At the end of the 1000 hr period the emitter was subjected to performance mapping by varying the voltage and feed pressure. The results in Figure 32 show data points that generally extend above the $k_o = 0.8$, $P = 24 \times 10^{-13}$ curve shown in Figure 31. The straight line thrust curve indicates values of $k_o = 0.8$, $P \sim 80 \times 10^{-13}$. Thus the increase in performance observed may be characterized by an increasing value of P from 11 to $\sim 80 \times 10^{-13}$. As P increases the thrust data becomes more linear and the specific impulse more constant over the measured mass flow rate range. Note how the decreasing $\dot{m}$ data in Figure 32 is better than the data for increasing $\dot{m}$. This hysteresis is a further indication that an increase in P due to better wetting at the emitter edge occurs. Data was also taken at higher voltage (16.2 kV) to increase the specific impulse. The highest value achieved was 1470 sec at 12.5 μlb of thrust.
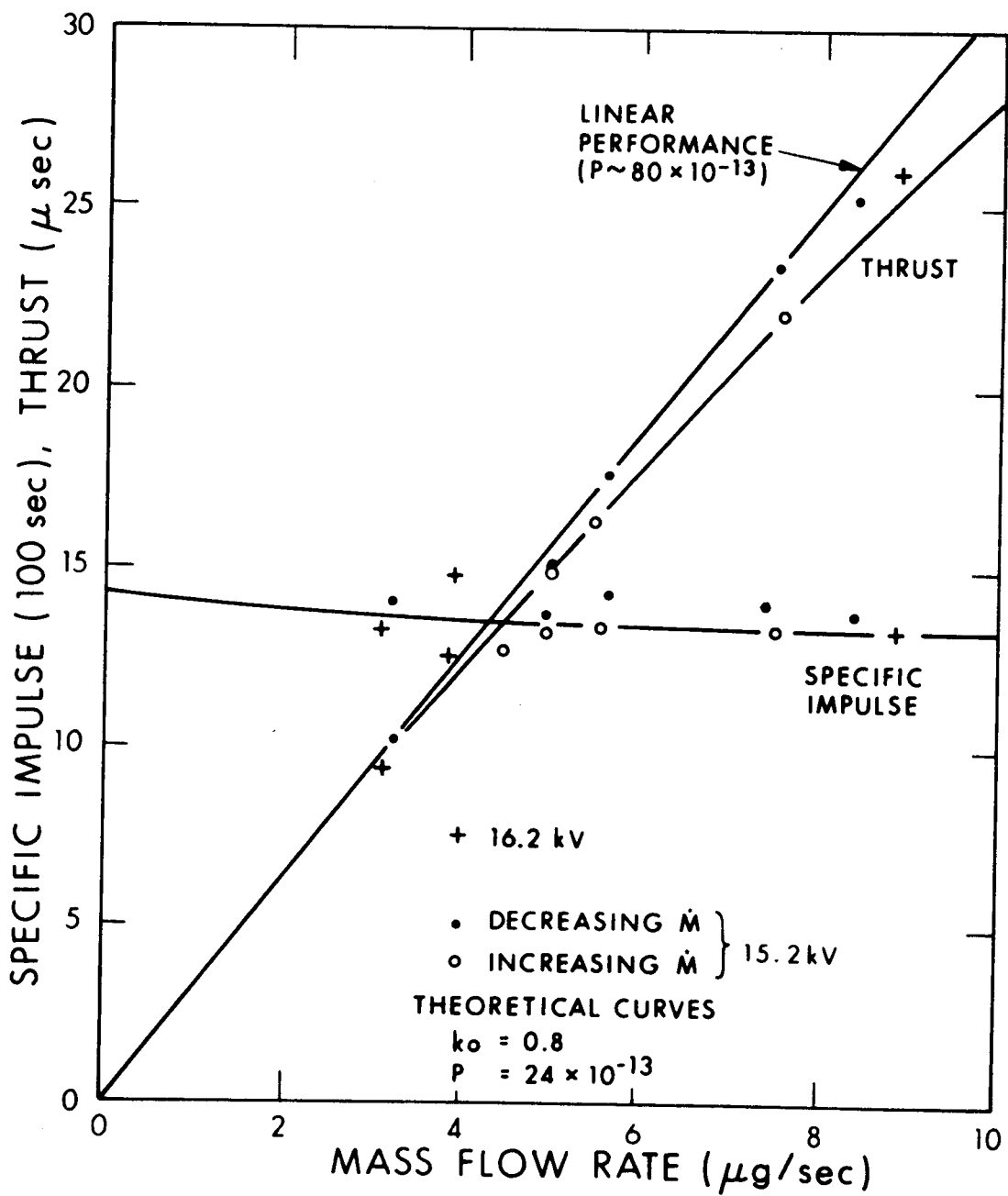
Figure 32. Performance Mapping, End of 1000-hour Test

Figures 33 and 34 show representative TOF traces and performance values obtained by computer calculations. Note the successive changes in the traces with time. The trace at 119 hours is quite linear to about 40 μsec with a near asymptotic tail. After some 300 hours the current decay in the region between 20 and 40 μsec decreases making the trace more concave. Three quarters of the way through the test the tail appears to shorten with a linear portion occurring for the first 30 μsec. This behavior continues until the end of the test. The general trend was toward increasing specific impulse as discussed above.

5.4   NEUTRALIZATION

The neutralizer configuration used during the test was similar to those used in previous tests. The neutralizer filament was a 1.5 inch length of 0.007 inch diameter tantalum wire and was selected on the basis of demonstrated reliability in both the ATS microthruster system and the SERT II emissive probe systems. The electron emission capability at the operating temperature of ~2000°K was several milli-amperes (purposely over an order of magnitude larger than the annulus current) to insure optimum neutralization. The neutralizer filament was positioned two inches downstream of the trap electrode and was electrically shielded from the trap electrode by a grounded shield. Without the shield, the electric field from the negative trap electrode would partially suppress electron emission from the neutralizer and effect the degree of neutralization obtained. A back up neutralizer was also included with automatic switching in case of failure, but was never used. The two neutralizers can be seen in Section 5.6 (Figure 40a).

In the usual operating mode the neutralizer filament was maintained at operational temperature with the TOF collectors and segmented collectors electrically connected to ground through a high impedance (10^7 ohm) voltmeter. In this way, a single "floating" potential enclosure was seen by the colloid beam and neutralizing electrons. The primary
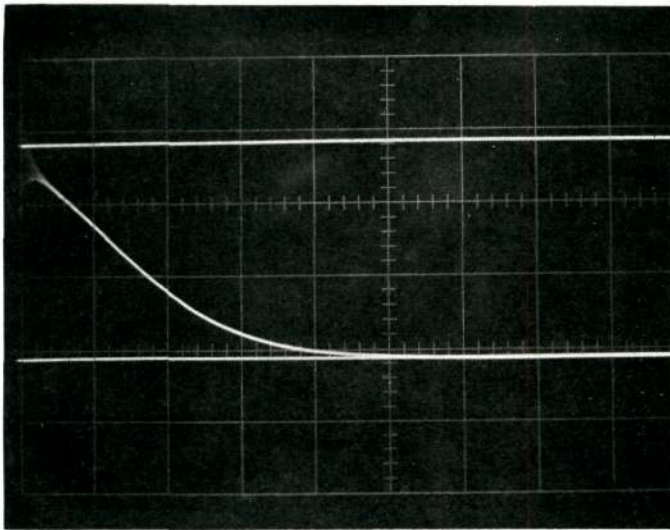
TOF #47 - Elapsed Time = 119.0 hr

Vert: 20 µA/cm - Horz: 20 µsec/cm

V_A = 15.3 kV - I_A = 64 µA

I_{sp} = 1070 sec - T = 27.4 µlb

$\dot{m}$ = 11.6 µgm/sec

$\langle\frac{q}{m}\rangle$ = 5.51 x 10^3 coul/kg
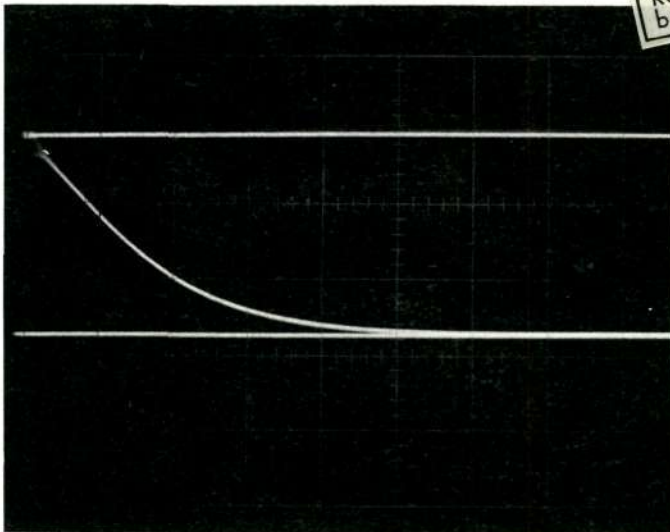
TOF #82 - Elapsed Time = 311.5 hr

Vert: 20 µA/cm - Horz: 20 µsec/cm

V_A = 15.2 kV - I_A = 60 µA

I_{sp} = 1140 sec - T = 21.7 µlb

$\dot{m}$ = 8.6 µgm/sec

$\langle\frac{q}{m}\rangle$ = 6.97 x 10^3 coul/kg
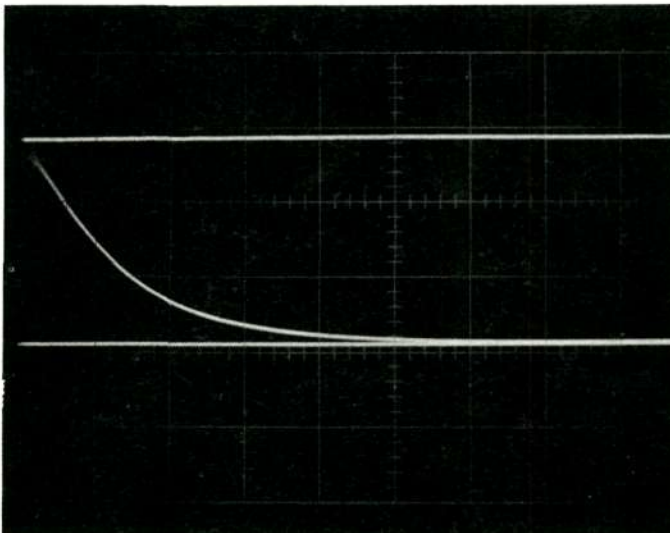
TOF #99 - Elapsed Time = 502.3 hr

Vert: 20 µA/cm - Horz: 20 µsec/cm

V_A = 15.5 kV - I_A = 65 µA

I_{sp} = 1130 sec - T = 23.8 µlb

$\dot{m}$ = 9.57 µgm/sec

$\langle\frac{q}{m}\rangle$ = 6.79 x 10^3 coul/kg

006266

Figure 33.   Time-of-Flight Photographs with Reduced Data for 1000-hour Test
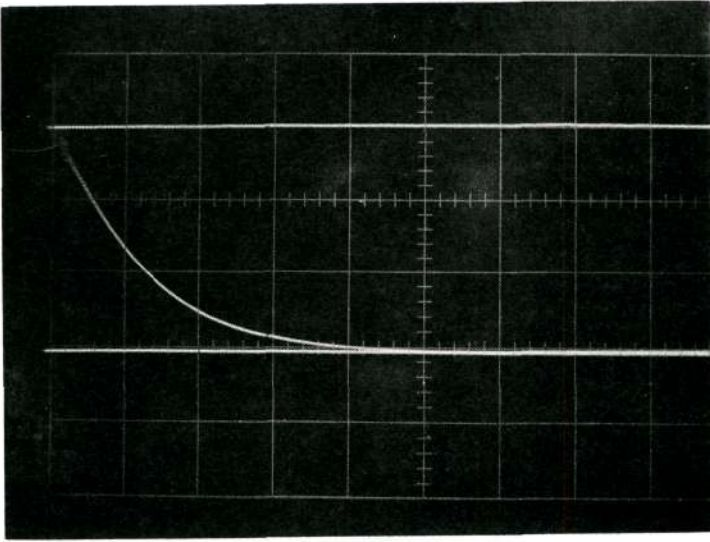
TOF #119 - Elapsed Time = 742.3 hr

Vert: 20 μA/cm - Horz: 20 μsec/cm

V_A = 15.2 kV - I_A = 68 μA

I_{sp} = 1320 sec - T = 21.4 μlb

$\dot{m}$ = 7.35 μgm/sec

$\langle \frac{q}{m} \rangle$ = 9.25 x 10^3 coul/kg
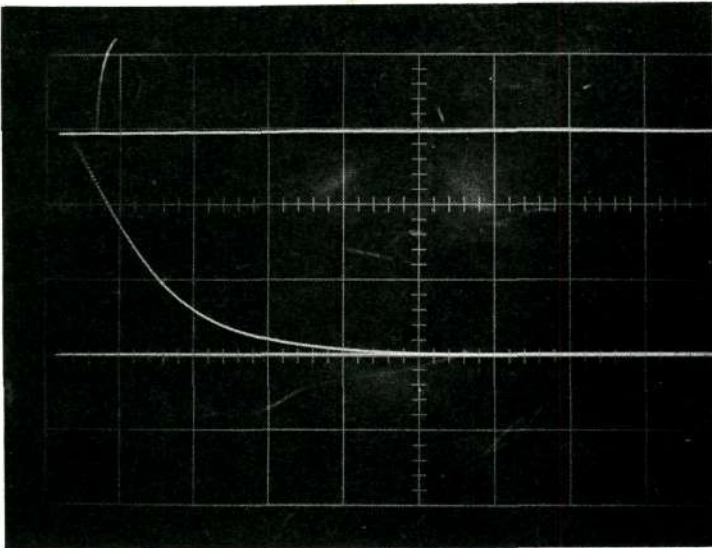
TOF #146 - Elapsed Time = 1000.1 hr

Vert: 20 μA/cm - Horz: 20 μsec/cm

V_A = 15.3 kV - I_A = 64 μA

I_{sp} = 1340 sec - T = 22.7 μlb

$\dot{m}$ = 7.70 μgm/sec

$\langle \frac{q}{m} \rangle$ = 8.31 x 10^3 coul/kg

006267

Figure 34. Time-of-Flight Photographs with Reduced Data for 1000-hour Test

measure of neutralization was the collector floating potential (V_c) which was continuously monitored throughout the test.

The floating potential of the unified collector assembly showed only minor variations throughout the 1000 hour duration of the test with an instrumental problem after about 225 hours producing the largest change observed. Prior to the 225 hour point, the operation had been very smooth with the floating potential (V_c) nominally +60V and the annulus current-neutralizer emission current difference (ΔI) was 10 μA at the nominal annulus voltage (V) of 15.2 kV. When either V or I increased, then V_c would show a corresponding decrease. At the 225 hour point, one portion of the segmented collector assembly shorted to ground inside the vacuum system and after isolating that segment from the rest of the floating enclosure the value of V_c increased to +80V with no major change in ΔI. The value of V_c gradually increased throughout the remainder of the test with the floating potential about +100V when the test was terminated. These higher values are directly attributed to the presence of the grounded segment in the floating potential enclosure.

5.5 THRUST VECTORING

During the 1000 hour test, reliable thrust vectoring was demonstrated and measurements of the beam profile were made periodically. The scanning probe detector used to measure beam deflection and the deflecting electrode configuration are described in Section 4.2. Although vectoring itself caused no difficulties, the frequency of vectoring measurements was minimized to avoid deleterious backscattering of material when the scanning probe passes directly in front of thruster surfaces. The probe motion described an arc with a radius of 20 cm from the emitter.

The beam deflection data presented in this section was analyzed by computer using the equations outlined in Section 4.2. Briefly, the equations convert the scalar quantities measured by experiment to a vector format to determine thrust vector orientation. The data from the thrust vectoring measurements are summarized in Table II. Listed in the table are the elapsed running time at which thrust vectoring was performed; θ_D, the deflection angle of the beam; ΔV, the deflection voltage; V and I, the annulus voltage and current at the time of thrust vectoring and the full width of half maximum (FWHM) of the normal profile.

TABLE II

THRUST VECTORING PARAMETERS

	TIME (Hours)	θ_D (Degrees)	ΔV (kV)	V (kV)	I (μA)	FWHM (Degrees)
1	164	-5.3	8	15.1	65	7.5
2	353	+5.8	8	15.4	60	5.5
3	687.7	+4.0	8	15.4	72	5.5
4	1004	-5.1	8	15.2	70	7.5

The beam was deflected in a horizontal plane to the left and right of the thruster axis for a total included angle of approximately 11°. Note from the table that, although some beam spread with time was observed, the FWHM remained nearly constant. The net deflection voltage of 8 kV was obtained by placing ±4 kV on opposite electrodes with the remaining two electrodes operated at -200 volts. The annulus current was only slightly affected by application of deflection voltages.

Figures 35 through 38 show the normal beam profile and the vectored beam profile for the four thrust deflection measurements listed in Table II. In the figures the scanning probe current is plotted as a function of detector angle from the centerline of the normal beam.
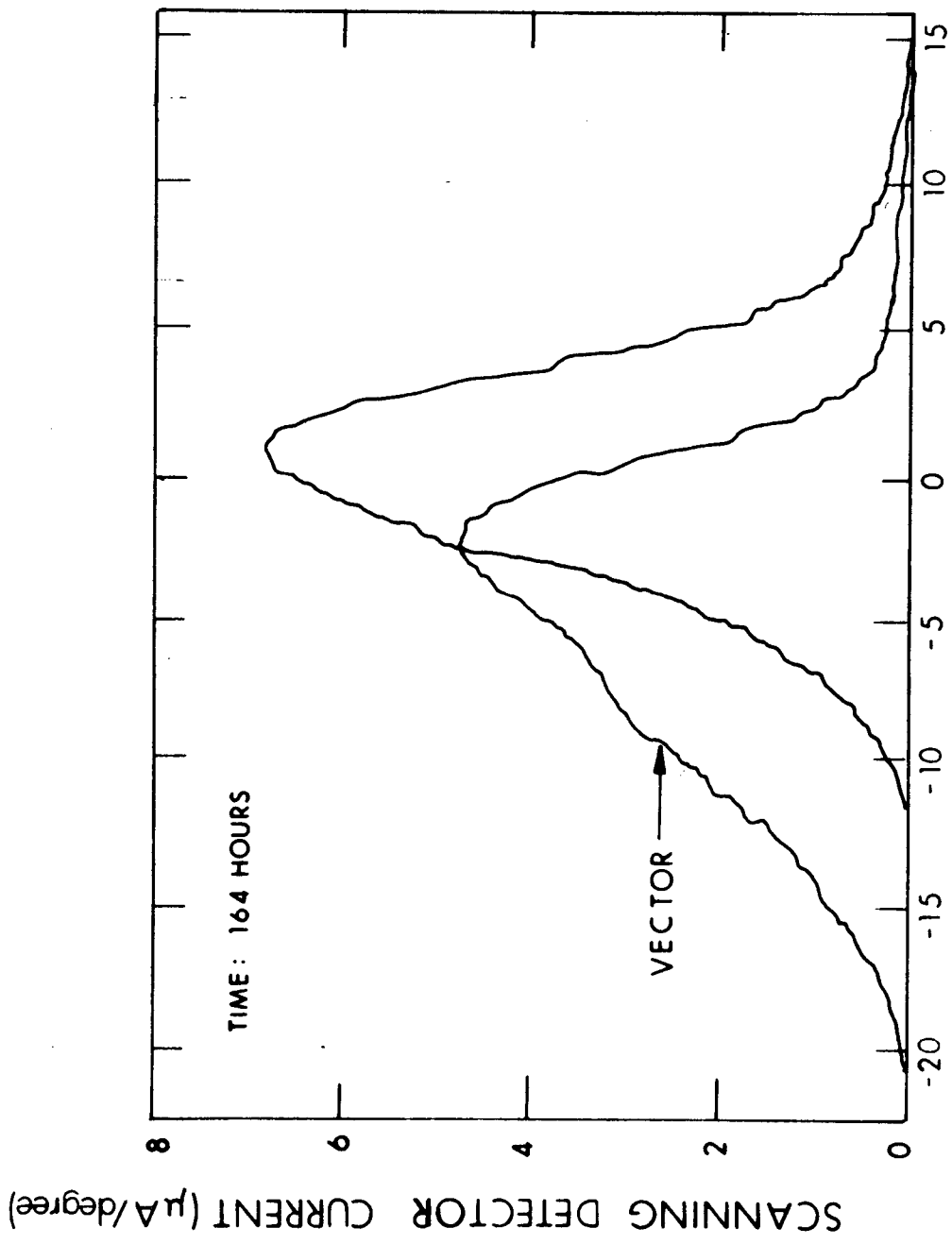
Figure 35. Normal and Vectored Beam Profiles at 164 Hours
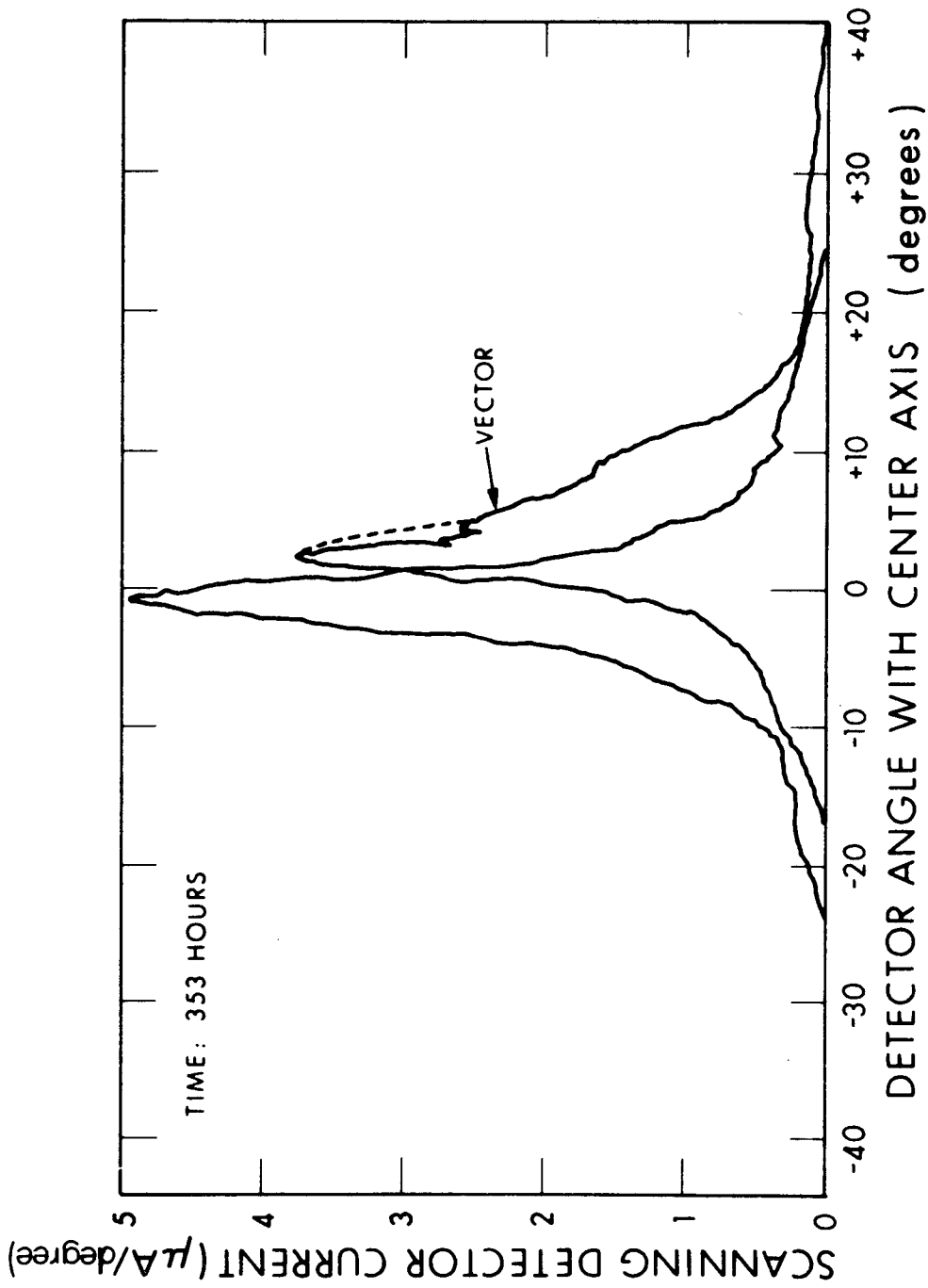
Figure 36. Normal and Vectored Beam Profiles at 353 Hours
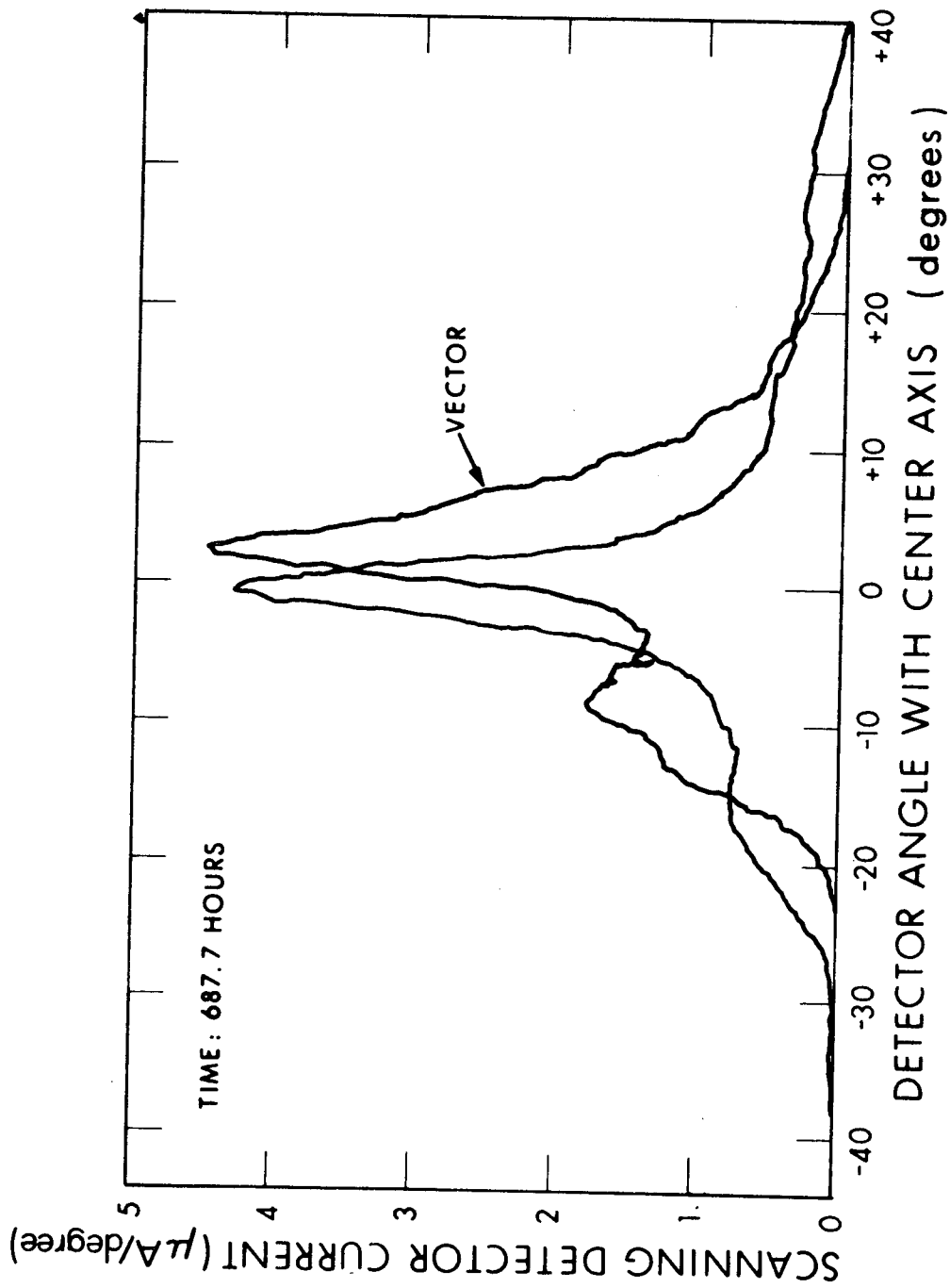
Figure 37. Normal and Vectored Beam Profiles at 687.7 Hours
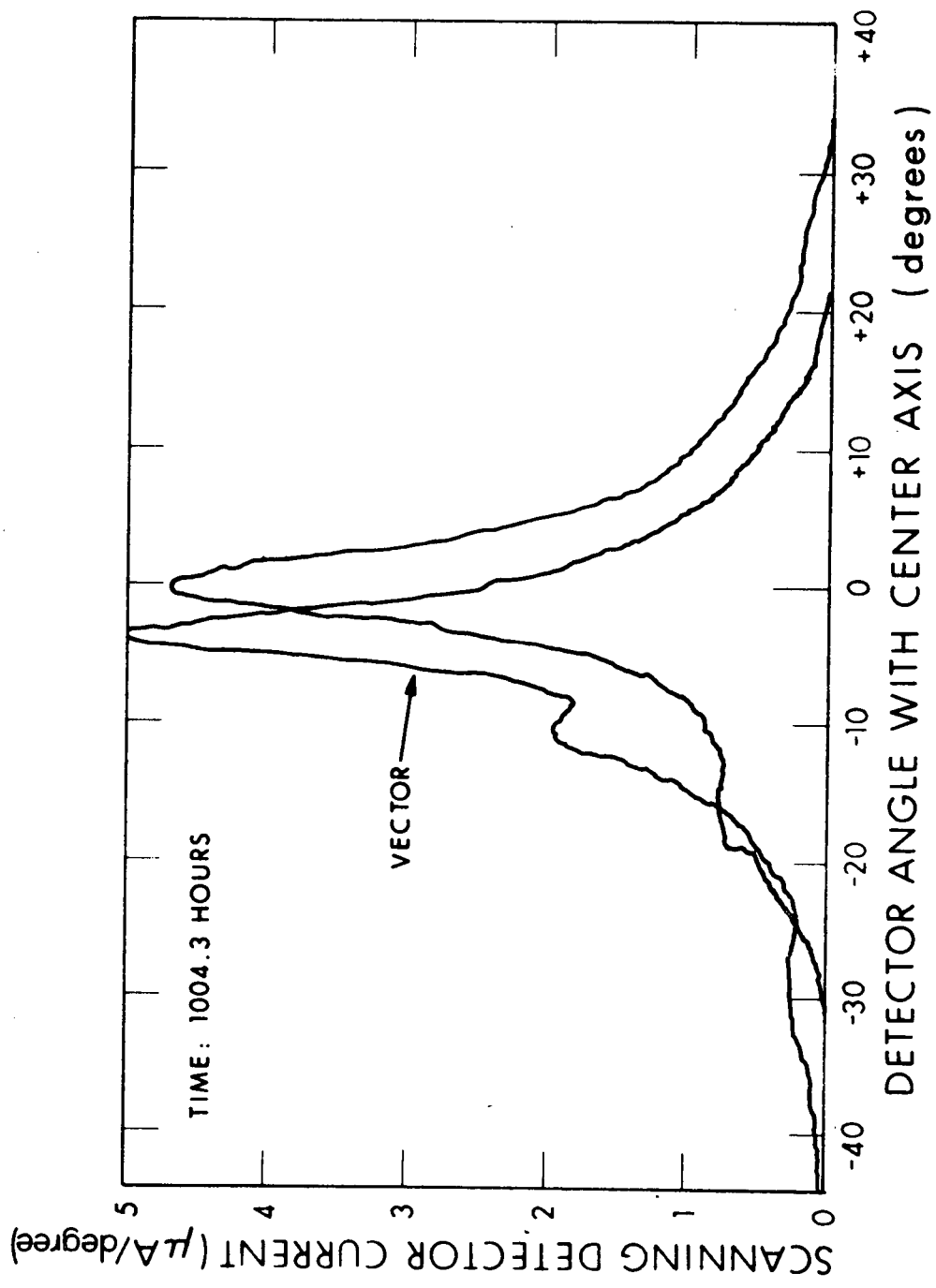
Figure 38. Normal and Vectored Beam Profiles at 1004.3 Hours

This data was recorded using an X-Y recorder where the signal proportional to angle was obtained from the motorized probe assembly and the current signal was obtained using an electrometer.

In all instances both the normal and vectored profiles showed Gaussian-like distributions. This similarity was used to quantitatively compare the beam profile with a true Gaussian distribution assuming that the ideal or optimum beam profile approaches a Gaussian distribution. Due to diverging fields at the emitter tip, space charge considerations, and perhaps other factors, actual beam profiles are expected to deviate from a true Gaussian. One measure of the amount of deviation is the ratio of the beam profile area contained beyond the FWHM (i.e. the wing area) to the total profile area. This is termed a beam profile factor (BPF) which when normalizing to a Gaussian distribution is given by

$$ BPF = \left(\frac{A_{fwhm}}{A_{Total}} \right)_{Beam} \Big/ \left(\frac{A_{fwhm}}{A_{Total}} \right)_{Gaussian} $$

For a Gaussian distribution 23.8% of the total area lies beyond the area contained within the FWHM (in the wing area). The normalized BPF has been calculated for normal beam profiles measured during the 1000 hour test and is plotted in Fig. 39 as a function of time.

At 164 hours the beam shape was very nearly Gaussian. Although not measured, a Gaussian distribution was assumed at time zero. As can be seen from Fig. 39, the trend in the beam profile is toward greater deviation from the Gaussian BPF until a maximum deviation was reached at 690 hours. Thereafter, the measured profile was found to continually improve (beam spread decreased) up to the time the test was terminated.
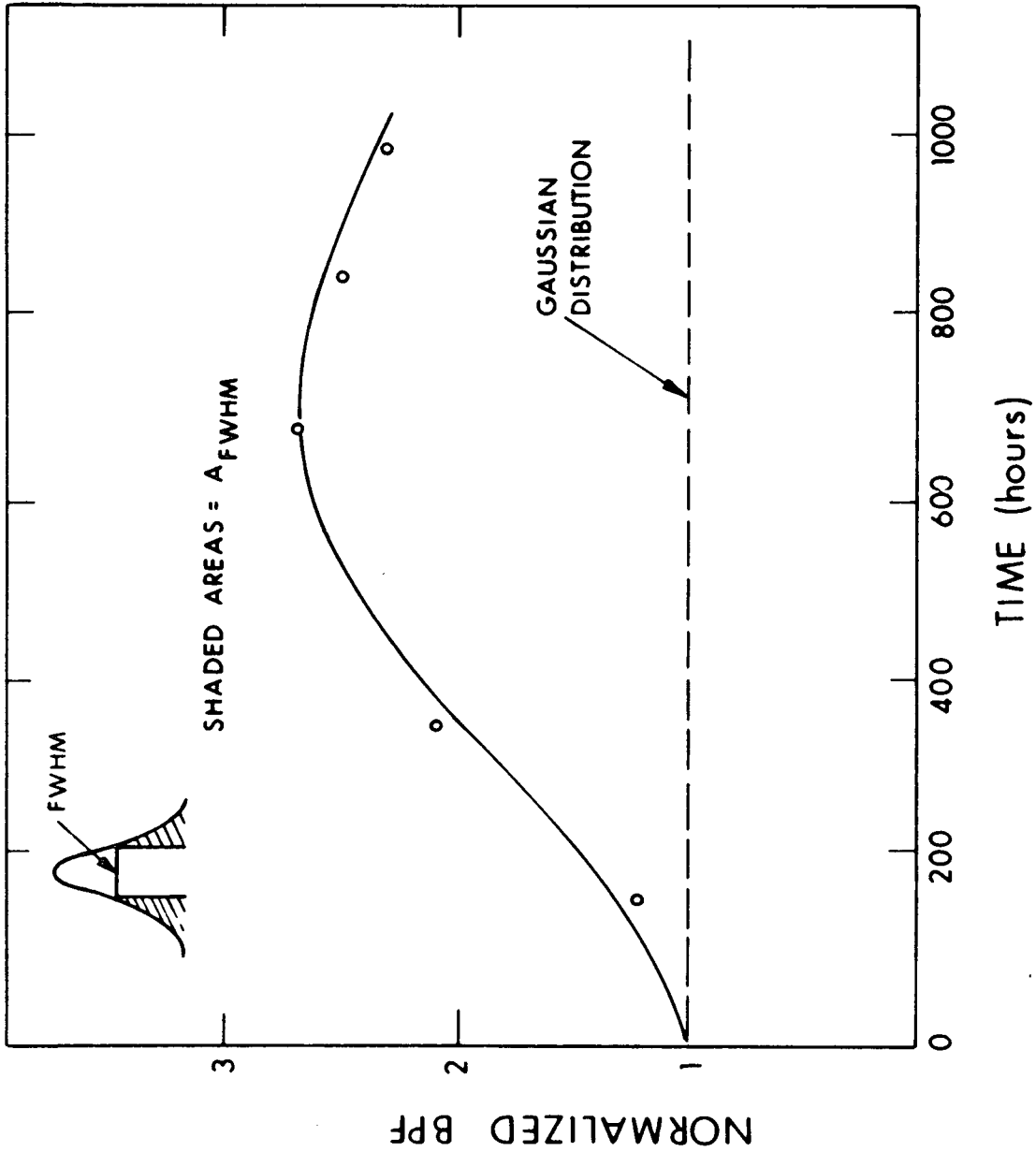
Figure 39. Normalized Beam Profile Factor (BPF) as a Function of Time

5.6   POST TEST THRUSTER EXAMINATION

After 1023 hours of continuous operation, the thruster test was volun-
tarily terminated to visually observe the condition of the thruster.
Figure 40 shows photographs of the thruster system as it appeared
after removal from the test chamber. Note from Fig. 40a. that back-
scattered material from the collectors was primarily deposited on the
trap electrode. The area on the trap electrode shielded by the neutral-
izer configuration remained clean. The area of the deflection electrodes,
inner extractor, and emitter was left relatively clean. This can be seen
more clearly in Figure 40b. which shows a closeup of the emitter and deflec-
tion electrodes. Figure 41 shows the interior of the thruster assembly with
the trap electrode housing removed. Note the backscatter deposits where
the electrodes were exposed.

Examination under a microscope and by photomicrographs at 100x enlarge-
ment, showed the annulus emitter condition to be generally excellent.
In addition, there was no indication of emitter plugging which is con-
sistent with the reproducibility of performance observed. Photomicro-
graphs of the annulus showing the emitter edges before and after clean-
ing are shown in Figures 42 and 43 respectively. Figure 43 should be
compared with Figure 29 showing the emitter edges before the 1000 hour
test to observe the excellent resistance to corrosion exhibited by the
annulus. The irregularities at the emitter edges and in the emitter
gaps seen in the photomicrographs of Figure 42 are due to propellant
fluid. A small deposit on those portions of the annulus across from the
four corners of the vectoring electrodes was observed. These deposits
did not appear to affect thruster performance, and should not affect the
performance appreciably even if the annulus were to be become totally
clogged at these points because they represent only a small part of the
total emission area. One short region of the emitter edge looks as
though it provided less emission than the rest. This region may not
have wetted properly or may possibly have changed with time providing
the increase in the performance index, P discussed in Section 5.3.

(a)
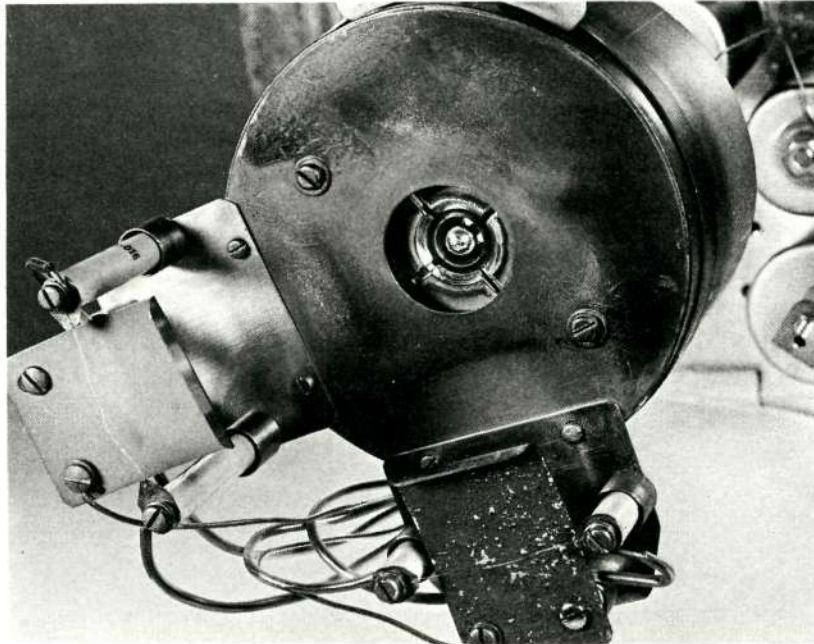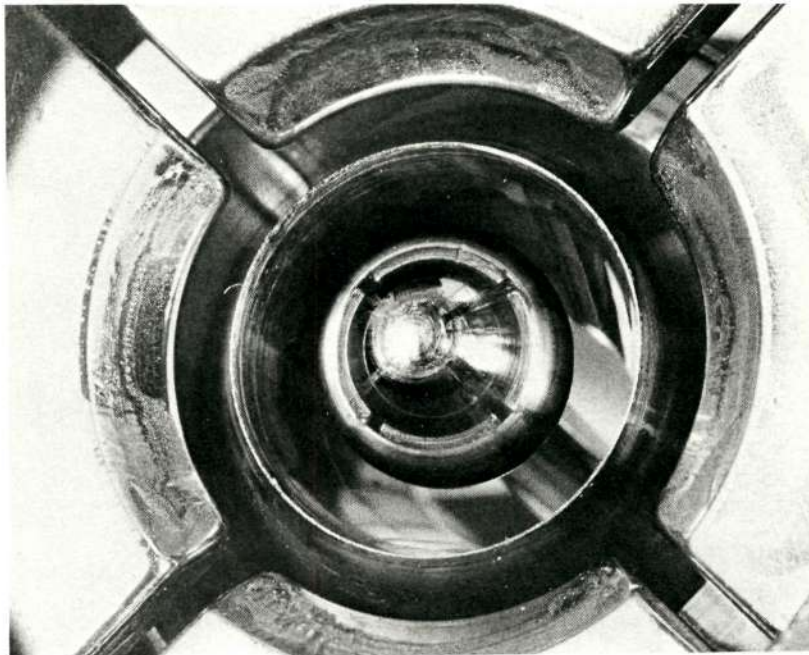
(b)

Figure 40. (a) Annulus Thruster Assembly after 1000-hour Test
(b) Close Up of Trap Electrode

80
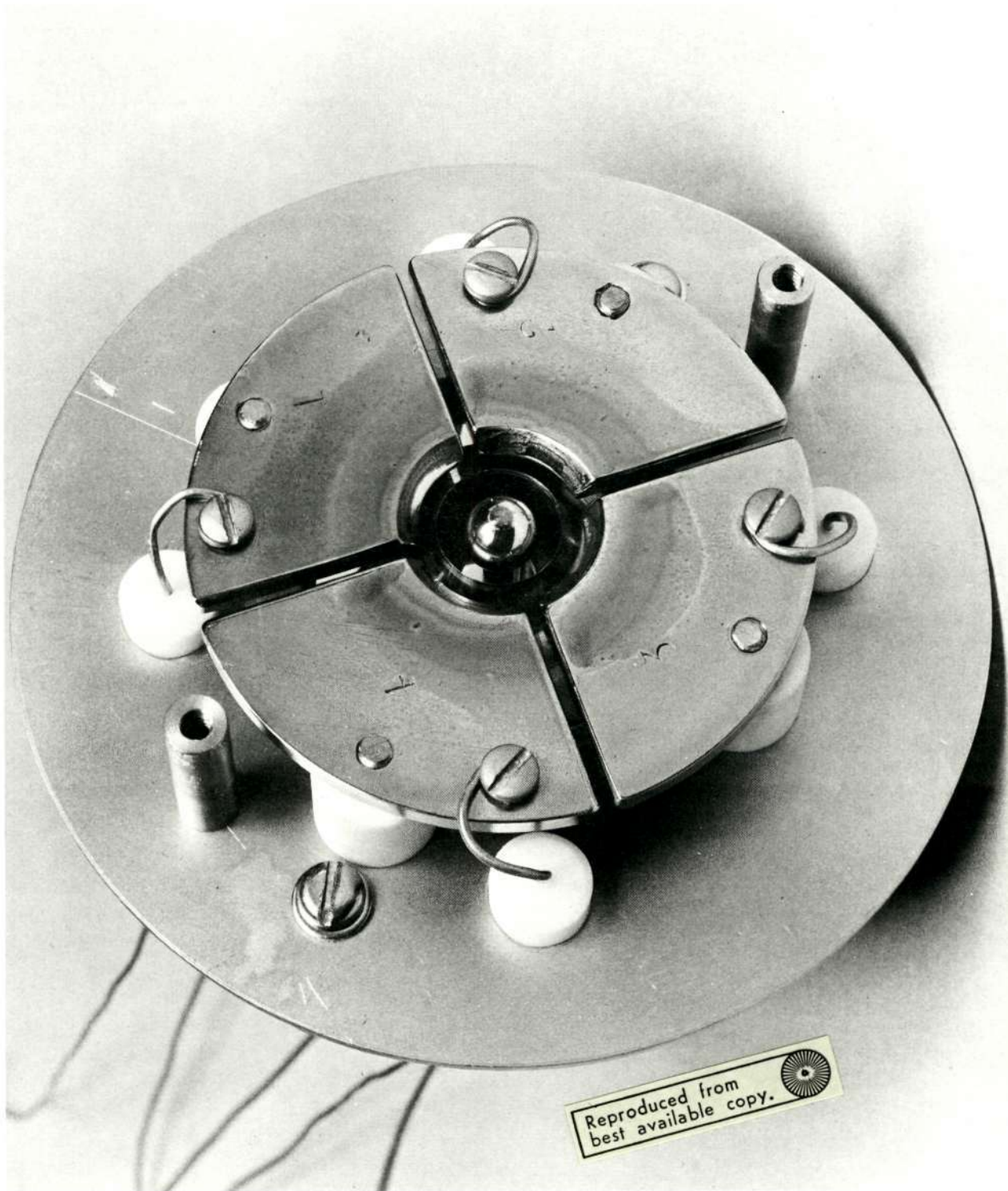
Figure 41.   Interior of Annulus Thruster Assembly with Trap Electrode
Housing Removed

81
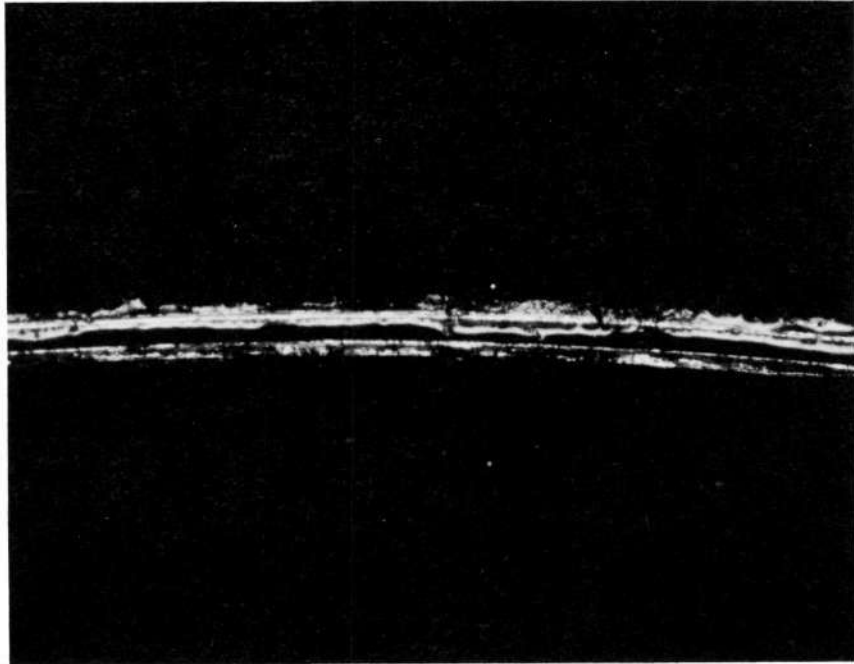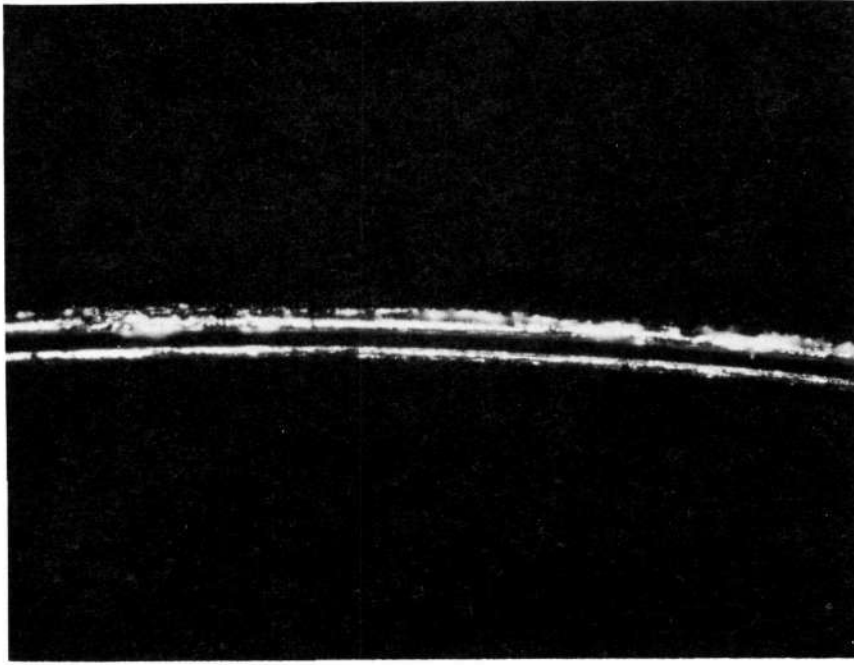
Figure 42. Photomicrographs (X100) of 1000-hour
Annulus Emitter before Cleaning
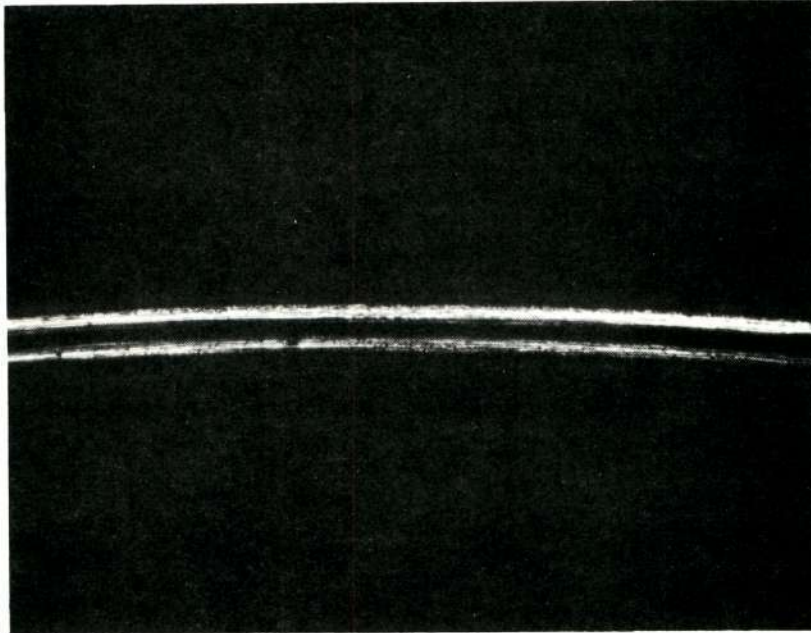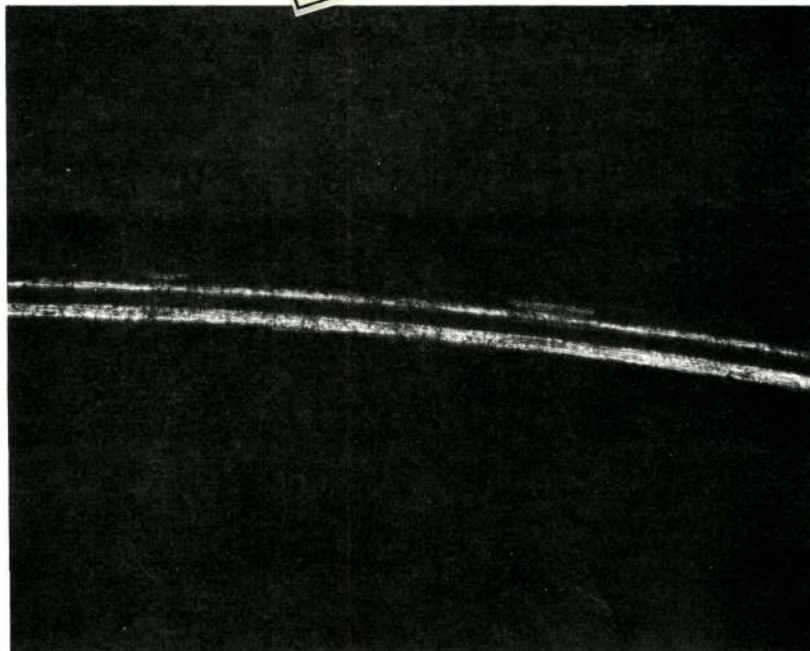
006268

Figure 43.   Photomicrographs (X100) of 1000-hour
             Annulus Emitter after Cleaning

APPENDIX I

ANNULAR EMITTER GEOMETRICAL AND FLOW PROPERTIES

The geometrical and flow properties of the emitters tested on the program (Phase II) are included for reference purposes. The notations used are defined as follows: h is the annulus gap, a is the emitter edge thickness and ℓ the length of the gap. All dimensions are given in inches. The normalized permeability is defined by

$$\text{Normalized permeability} = P_A/P_N$$

where P_N is inversely proportional to the time for a given volume of gas to flow through a standard needle (0.004 inch i.d. and 1 cm long). P_A is the permeability of an annulus for an equal flow (volume) of gas.

Emitter Identification	Emitter Material	Critical Dimensions	Normalized Permeability
A06	20Cb3	h $\sim$ metal-to-metal fit ℓ = 0.02 a $\sim$ 0.001	10
A10	20Cb3	h = 0.001 ℓ = 0.100 a = 0.001	4.5
T01	20Cb3	h = 0.0005 ℓ = 0.4 a = 0.001 $\pm$ 0.0005	2.9 (lapped)
T03	20Cb3	h = 0.0005 ℓ = 0.4 a = 0.002 $\pm$ 0.0005	6.3 (lapped)
PT04	Pt (90%) Ir (10%)	h = 0.0005 $\ell \cong$ 0.4 a = 0.001 to 0.003	4.8 (lapped)

Emitter Identification	Emitter Material	Critical Dimensions	Normalized Permeability
PT05 (1000 hr Annulus)	Pt (90%) Ir (10%)	h = 0.0005 ℓ = 0.4 a = 0.001 $\pm$ 0.0005	6.0 (lapped)
PT07 (Deliverable Thruster)	Pt (90%) Ir (10%)	h = 0.0005 ℓ = 0.4 a = 0.001 $\pm$ 0.0005	7.8 (lapped)

4040-Final

PROPELLANT BATCH TABLE (PHASE II)

BATCH NO.	DOPANT/FLUID	SPECIFIC CONDUCTIVITY $10^{-4} \, \Omega^{-1} \, cm^2$	EQUIVALENT CONDUCTIVITY $\times 10^{-1} \, \Omega^{-1} \, cm^2$	REMARKS
F07	30 gms NaI/100 ml Glycerol	2.5	1.25	Filtered, outgassed
F08	20 gms LiBr/100 ml Glycerol	2.0	0.86	Filtered, outgassed
F09	20 gms LiCl/100 ml Glycerol	1.2	0.24	Filtered, outgassed
F10	30 gms LiBr/100 ml Glycerol	2.0	0.55	Filtered, outgassed
F11	20 gms KI/100 ml Glycerol	4.2	3.49	Not filtered, outgassed 7 days
		3.6	2.99	Filtered, outgassed 4.5 hours
		2.7	2.24	Outgassed additional 5 days
F12	30 gms KI/100 ml Glycerol	4.3	2.39	Not filtered, outgassed overnight
		4.2	2.33	Filtered, outgassed overnight
F13	10 ml HI/100 ml Glycerol	>10	----	HI (47-50%); filtered, outgassed
F14	10 gms HIO$_3$/100 ml Glycerol	0.25	0.44	Filtered, outgassed; reacted chemically with glycerol to give strong odor.
F15	30 gms LiI/100 ml Glycerol	1.35	0.60	Not filtered, outgassed (blue-grayish color not filtered).
F15A	30 gms LiI + 1 gms LiOH/100 ml Glycerol	1.4	0.52	Filtered, outgassed; 1 gm LiOH added to F15 (Solution clear when filtered).
F16	30 gms NaI + 2 gms NaOH/ 100 ml Glycerol	3.05	1.22	Filtered, outgassed.

APPENDIX II

PROPELLANT BATCH TABLE (PHASE II)

continued

BATCH NO.	DOPANT/FLUID	SPECIFIC CONDUCTIVITY $10^{-4} \Omega^{-1} cm^2$	EQUIVALENT CONDUCTIVITY $X10^{-1} \Omega^{-1} cm^2$	REMARKS
F17	30 gms NaI + 3 gms NaOH/ 100 ml Glycerol	2.9	1.05	Filtered, outgassed
F18	22.4 gms MgI$_2$/75 ml Glycerol	---	----	Reacted chemically with glycerol forming block viscous liquid still forming bubbles after 3 days outgassing.
F19	30 gms NaI + 1 gm NaOH/ 100 ml Glycerol	2.68	1.19	Filtered, outgassed
F20	1 gms LiOH/100 ml Glycerol	2.75	6.60	Filtered, outgassed
F21	30 gms LiI/100 ml Glycerol	0.90	0.40	Filtered, outgassed at 180°C for 7 hours.
F22	30 gms LiI/100 ml Glycerol	---	---	1000 hr life test fluid
F23	30 gms LiI/100 ml Glycerol	---	---	Deliverable thruster fluid.

COLLOID THRUSTER TEST RUNS

(PHASE II)

Run No.	Emitter	Propellant	Remarks
7010-01	A10	F07	Neutralizer tests. Three neutralizer configurations tested. Floating collector voltages less then 50V achieved at 15kV at annulus currents greater than 70uA. Tradeoff of beam coupling with trap electrode voltages, V, V_{ix}, V_{ox} and P_f investigated.
7010-02	A10	F10	Test to study characteristics of 30 gm LiBr/100 ml glycerol propellant. Examination of emitter showed fluid to be very corrosive $I_{sp} > 1000$ obtained at $+2.5^{\circ}C$ at low thrust levels. Insufficient data taken due to early test termination.
7010-03	A10	F10	Continuation of neutralizer tests. Good beam coupling observed (<50V) with shielded neutralization configuration.
7010-04	A06	F11	Propellant test. Performance mapping of 20 gms KI/100 ml glycerol.
7010-05	A06	F13	Propellant test. Performance mapping of 10 ml HI/100 ml glycerol.
7011-01	A06	F15	Propellant test. Performance mapping of 30 gms LiI/100 ml glycerol.
7011-02	A06	F16	Propellant test. Performance mapping of 30 gms NaI + 2 gms NaOH/100 ml glycerol.
7011-03	A06	F17	Propellant Test. Performance mapping of 30 gms NaI + 3 gms NaOH/100 ml glycerol.

COLLOID THRUSTER TEST RUNS

(PHASE II)

Run No.	Emitter	Propellant	Remarks
7011-04	A06	F19	Propellant test to examine 30 gms NaI + 1 gm NaOH/100 ml glycerol with 0.400 in. conical inner extractor. Test terminated early due to nonuniform spraying characteristic originating at a small area along emitter edge.
7012-01	A06	F19	Propellant Test. Performance mapping of 30 gms NaI + 1 gm NaOH/100 ml glycerol using a smaller diameter conical extractor than used in previous test.
7012-02	A06	F15A	Propellant Test. Performance mapping of 30 gms LiI + 1 gm LiOH/100 ml glycerol. 0.313 in. dia. spherical extractor used.
7012-03	T01	F07	Tapered Emitter Test. Higher specific impulse obtained with this design as compared to A06.
7012-04	A06	F07	Thrust Vectoring Tests. Beam deflected at -2 kV and -5 kV. Peak shift of ~5 to 6 degrees observed at -5 kV. Beam profile measured as a function of feed pressure.
7012-05	A06	F07	Thrust Vectoring Tests. Beam deflected about 4° at -7.5 kV with and without beam neutralization.
7012-06	T03	F07	Thrust Vectoring Tests. Beam deflected by 9° using both positive and negative deflection voltages simultaneously with beam neutralization.
7012-07	T03	F21	Annulus operated 120 hours continuously. LiI doped propellant shows excellent stability. Tapered emitter performance mapping done. Thrust vectoring in 2-orthogonal directions done.

4040-Final

Run No.	Emitter	Propellant	Remarks
1000 Hr.	PT05	F22	An annulus emitter was operated continuously for over 1000 hours. Average performance levels were: I_{sp} = 1160 sec, T = 25 ulbs. The beam was neutralized and thrust vectoring was demonstrated periodically with $\pm 5^{\circ}$ deflection.
Deliverable Thruster Test	PT07	F23	An emitter built to reproduce the operation of the 1000 hour emitter was tested. Good reproducibility was achieved as performance levels for the 1000 hour annulus were duplicated.

APPENDIX IV

D-THRUSTER SYSTEM

A laboratory thruster system was designed to duplicate the operation of annulus PT05 as measured during the 1000 hour test. The critical dimensions and materials were duplicated to test the reproducibility of the design and only structural and mounting features were altered to allow for testing in a laboratory other than ours. The thruster system was fabricated and tested and demonstrated excellent reproducibility of design and fabrication. The test also included operation at higher voltages than those used previous in our laboratory in in an effort to increase the specific impulse. The results were successful although the increase was not as large as expected based upon analytical considerations.

Description of Thruster Components

The deliverable annular colloid thruster unit is shown schematically in Figure IV-1. The following list identifies the basic thruster components where the item number corresponds to the numbers in the figure.

1. Inner extractor
2. Annular emitter
3. Outer extractor/vectoring electrodes
4. Trap electrode housing
5. Insulator shield
6. Support plate
7. Insulator
8. Pin vice support for inner extractor rod
9. Silicon glass laminate back plate
10. Propellant feed tube
11. Support rod for inner extractor
12. Aluminum support rod
13. Neutralizer filament shield
14. Neutralizer filament wire
15. Annulus support housing
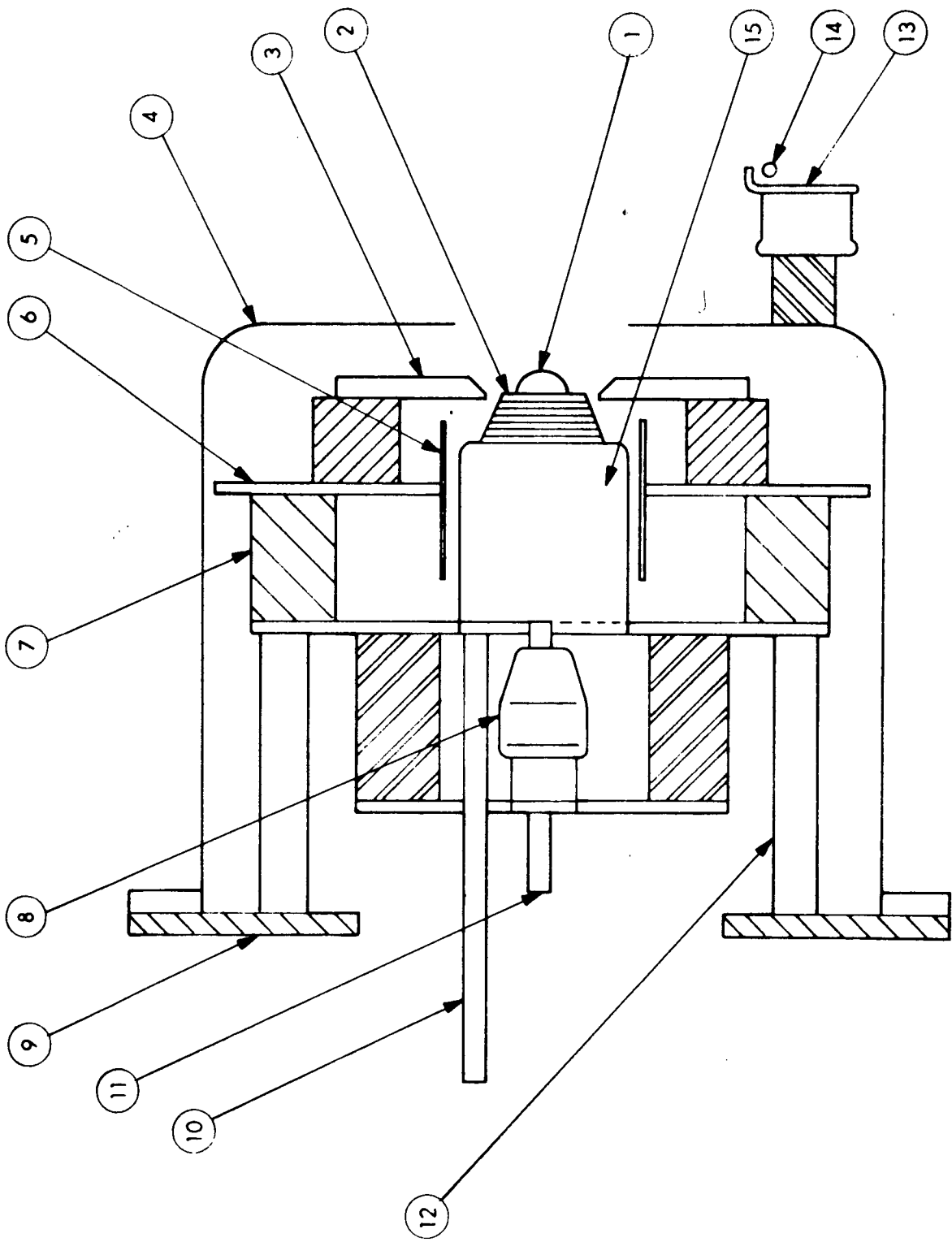
Figure IV-1. Annular Thruster Cross Section

The trap electrode housing (4) has a 1.250 inch aperture and mounts directly to the silicon glass laminate back plate (9). By mounting in this manner, the trap housing can be removed to facilitate modification or examination of other thruster components. The pin vice (8) used to support the inner extractor rod (11), allows axial and radial adjustments used for alignment of the inner extractor (1) within the annulus. Electrical connections for thruster operation terminate at the silicon glass laminate back plate. These terminals include connections for the four individual vectoring segments (V1, V2, V3, V4), the inner extractor and the trap electrode. Attached to the trap electrode mounting ring are the terminals used to make electrical connections with the neuttalizer filament (14) and neutralizer filament shield (13). In the present thruster configuration, no provision is available for making source high voltage connections at the back plate. It is intended the source high voltage connection be made on the propellant feed tube.

The inner extractor is spherical with a 0.313 inch diameter. The outer extractor/vectoring electrodes are machined from a circular stainless steel plate 2.50 inch diameter by 0.125 inch thick which is divided into four segments. When mounted and properly aligned, the spacing between neighboring segments is kept at 0.050 inches with a circular center opening of 0.650 inches. The colloid emitter is a platinum/iridium tipped annulus with a radius of curvature of 0.250 inch. The emitter has edge dimensions of 0.001 inch and a propellant feed gap of 0.0005 inch.

Thruster Operation Procedure

After mounting the thruster in a test chamber it is recommended that the thruster assembly be allowed to outgas in vacuum (10^{-6} Torr or lower) for at least 24 hours before thruster operation is initiated using the following sequence.

1. Apply trap electrode voltage (nominally -500 volts).
2. Apply outer extractor voltage (-200 volts on V1, V2, V3, and V4).
3. Apply inner extractor voltage (nominaly -2kV).

4. Apply annulus voltage (set at +15 kV for initial operation).

5. Set feed system pressure to initiate spraying at low level.

When operation in a neutralized mode is desired, the collector must be electrically isolated from ground and the neutralizer power applied (usually occurs after step 5 above). For the recommended 2 amp neutralizer heating current it may be necessary to reduce the trap electrode voltage to achieve sufficient beam coupling. The trap electrode should not be adjusted to the extent electron feedback to the emitter is observed. For vectoring operations, voltage combinations are applied to the V1, V2, V3, and V4 electrodes shown schematically in Figure IV-2. Usually one pair of opposing segments are held at -200V and the other pair of segments are used for deflection by applying high voltage. It is recommended that the thruster assembly be mounted within a ground screen to prevent electron impingment on electrical leads, vacuum flange terminal bushings, etc. located at the rear of the thruster.

Thruster Tests

The thruster unit, which is very similar to the 1000 hour thruster, was performance mapped at source voltages of +15, 17.5 and 20 kV. The emitter for this thruster was fabricated with the intentions of reproducing the gas flow permeability of the 1000 hour annulus. The normalized permeabilities for the 1000 hour and deliverable thruster emitters were 6.0 and 7.6 respectively. An indication of the reproducibility achieved is also reflected by the 15 kV data in Figure IV-3, where the thrust and specific impulse obtained with this thruster are compared with the performance of the 1000 hour hour thruster. The test indicates that the charge-to-mass ratio of the particles did not increase appreciably with voltage. An observed increase in specific impulse at 17.5 kV and 20 kV over that of 15 kV was apparently due to the increase in accelerating voltage.

4040-Final
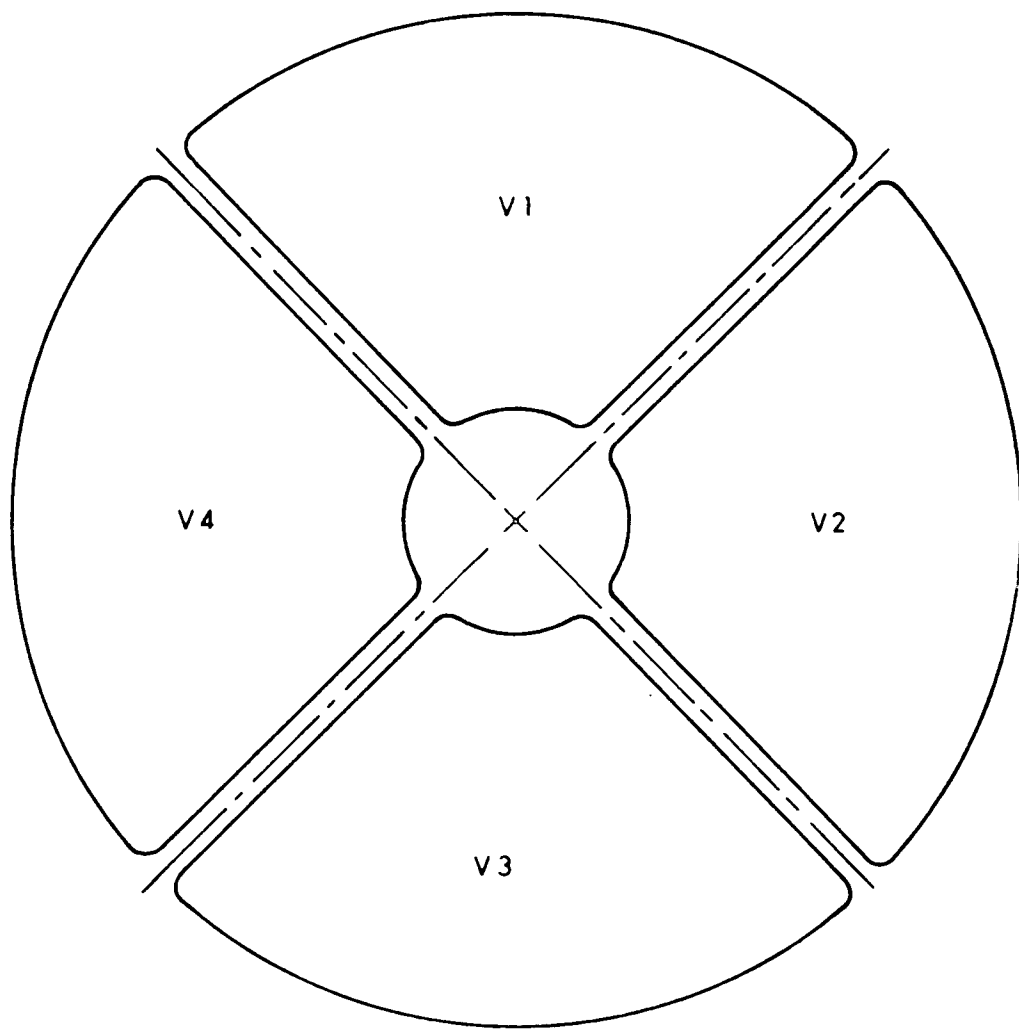
Figure IV-2. Vectoring Electrode Configuration

40922
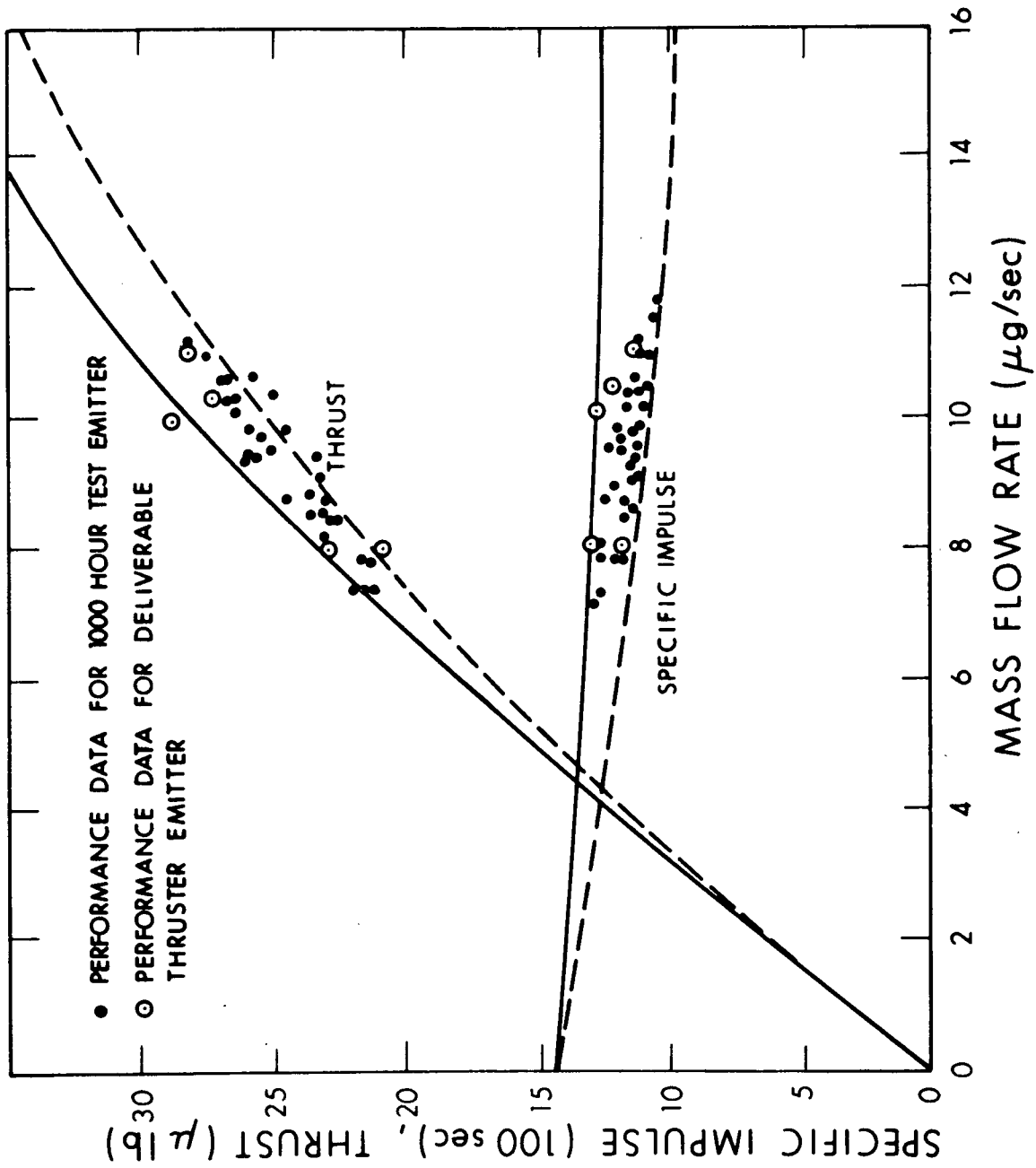
Figure IV-3. Comparison of Performance Data for 1000-Hour Test and B Thruster Emitters

APPENDIX V

MASS FLOW METER

An analysis of the operation of the thermal-differential mass flow
meter design used at EOS was performed to isolate those physical para-
meters which are most critical in determining flow meter sensitivity.
Consider a small capillary tube of thermal conductivity k and length ℓ
whose ends ($\pm \ell/2$) are maintained at a constant temperature T_o. The
tube is filled with a liquid of thermal conductivity k' and specific
heat capacity, C. The center of tube is maintained at a temperature,
T_{center} by a point source heating element. If the fluid is stationary,
the steady state temperature distribution is determined from the familiar
heat equation:

$$\triangle^2 T = 0. \tag{V-1}$$

The solution of Eq.(V-1) is a simple ramp distribution symmetric about
the discontinuity at X=0, the mid-point of the tube (see Fig. V-1).

When fluid is moving through the tube an asymmetry in the temperature
distribution about X=0 results. If the fluid is moving with a velocity
v, corresponding to a mass flow rate $\dot{m}$, along the X axis of the tube,
then conservation of heat flow requires:

$$(kA + k'A') \triangle^2 T = \dot{m}C \, \triangle T, \tag{V-2}$$

where A is the area of the tube and A' is the area of the fluid.

Equation (V-2) can be reduced to a problem in one dimension by introducing
the following assumption: Temperature gradients perpendicular to the
direction of flow are assumed equal to zero. This assumption may be
justified by requiring the diameter of the capillary tube to be small

(fluid velocity also assumed small). By letting

$$\alpha = \frac{\dot{m}C}{(kA + k'A')},$$ (V-3)

Eq. V-2 can be expressed as

$$\frac{d^2T}{dX^2} = \alpha \frac{dT}{dX} .$$ (V-4)

The solution of Eq. V-4 is

$$T = \alpha^{-1} \exp (\alpha X + C_1) + C_2$$ (V-5)

Applying the boundary conditions to the flow in the capillary tube, that

$$T = T_o \text{ when } X = \pm \ell/2 \text{ and } T = T_{center} \text{ at } X = 0$$

the solutions for the steady state temperature distribution to the left and right of the discontinuity become

$$T(X)_L = \frac{\Delta T \exp (\alpha X)}{[1 - \exp (-\alpha\ell/2]} - \frac{\Delta T}{[1 - \exp (-\alpha\ell/2]} + T_{center},$$ (V-6)

and

$$T(X)_R = \frac{\Delta T \exp (\alpha X)}{[1 - \exp (\alpha\ell/2]} - \frac{\Delta T}{[1 - \exp (\alpha\ell/2]} + T_{center},$$ (V-7)

where

$$\Delta T = T_{center} - T_o .$$

The temperature sensor location on each side of the heater where the maximum temperature difference occurs is

$$X = \ell/4$$ (V-8)

or the maximum temperature difference will be measured when the temperature sensors are located half way between the heat source and the end of the capillary tube maintained at $T=T_o$ and that this result is independent of the fluid velocity.

Typical temperature distributions as a function of position along the metering tube for flow and no-flow conditions are shown plotted in Fig. V-1. The temperature profile for the condition of flow were calculated using Eqs. V-6 and V-7. The figure illustrates the basic principle of operation for the thermal-differential mass flow meter. Since the sensor (thermocouple, thermistor, sensitor, etc.) located at $\pm \ell/4$ depends on a temperature difference for signal, no signal results when the fluid is stationary. A signal is obtained when the distribution is distorted due to removal of heat to the left of tube center. The signal, termed the maximum sensor signal, is the difference between the temperatures at $\pm \ell/4$.

The variation in maximum sensor signal as functions of the annular area and thermal conductivity of the metering tube wall, as well as the temperature at the tube center were also examined for a mass flow rate of 20 μgm/sec.

In Fig. V-2, the maximum sensor signal as a function of thermal conductivity of the metering tube is shown on a log-log plot. Note that the sensor signal increases with decreasing tube thermal conductivity. This suggests that a maximum signal would be obtained by placing the sensor in the fluid itself.

The sensor signal as a function of the annular area of the metering tube wall (proportional to tube wall thickness) is shown in Fig. V-3. This indicates that for optimum design of the flow meter tube, the wall thickness should be maintained as thin as possible. Decreasing the wall from 0.005 inch to 0.002 inch increases the sensitivity of the device by a factor of about six.
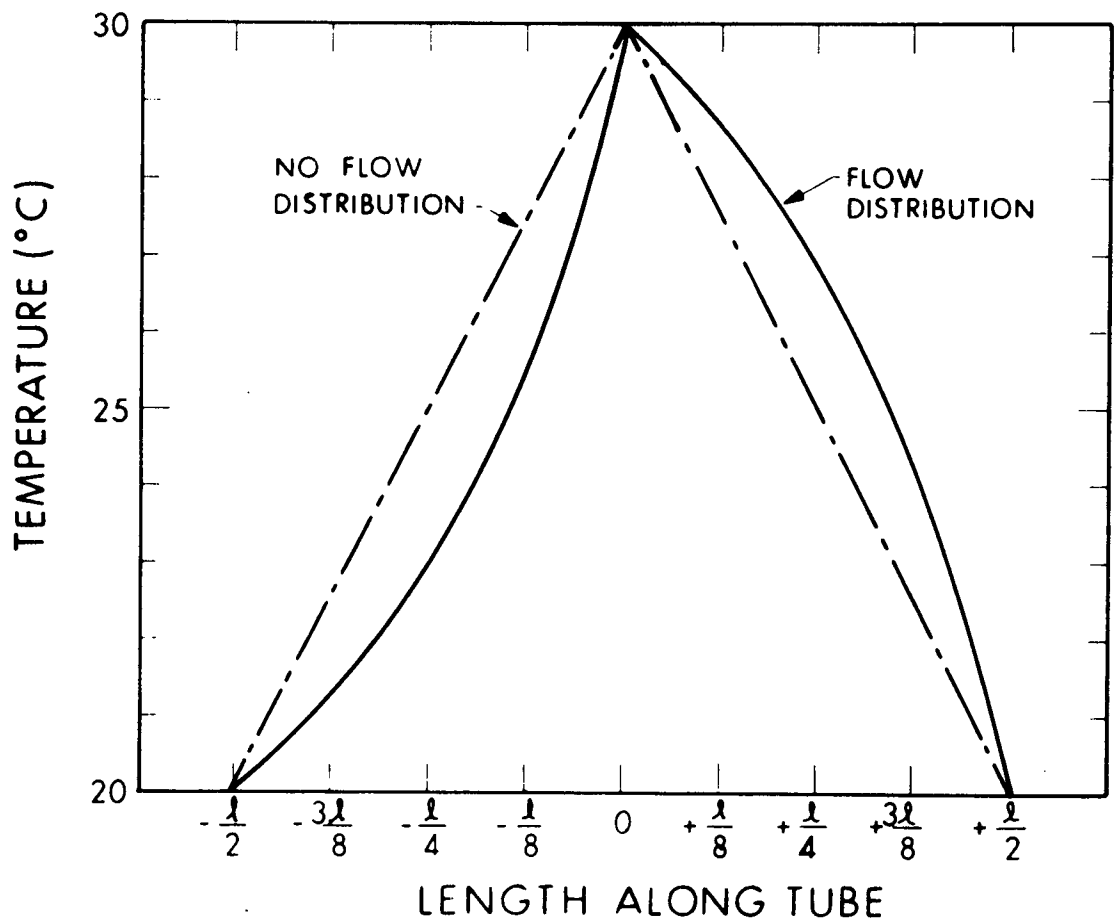
Figure V-1. Flow and No-Flow Temperature Profiles as a Function of Position Along Metering Tube
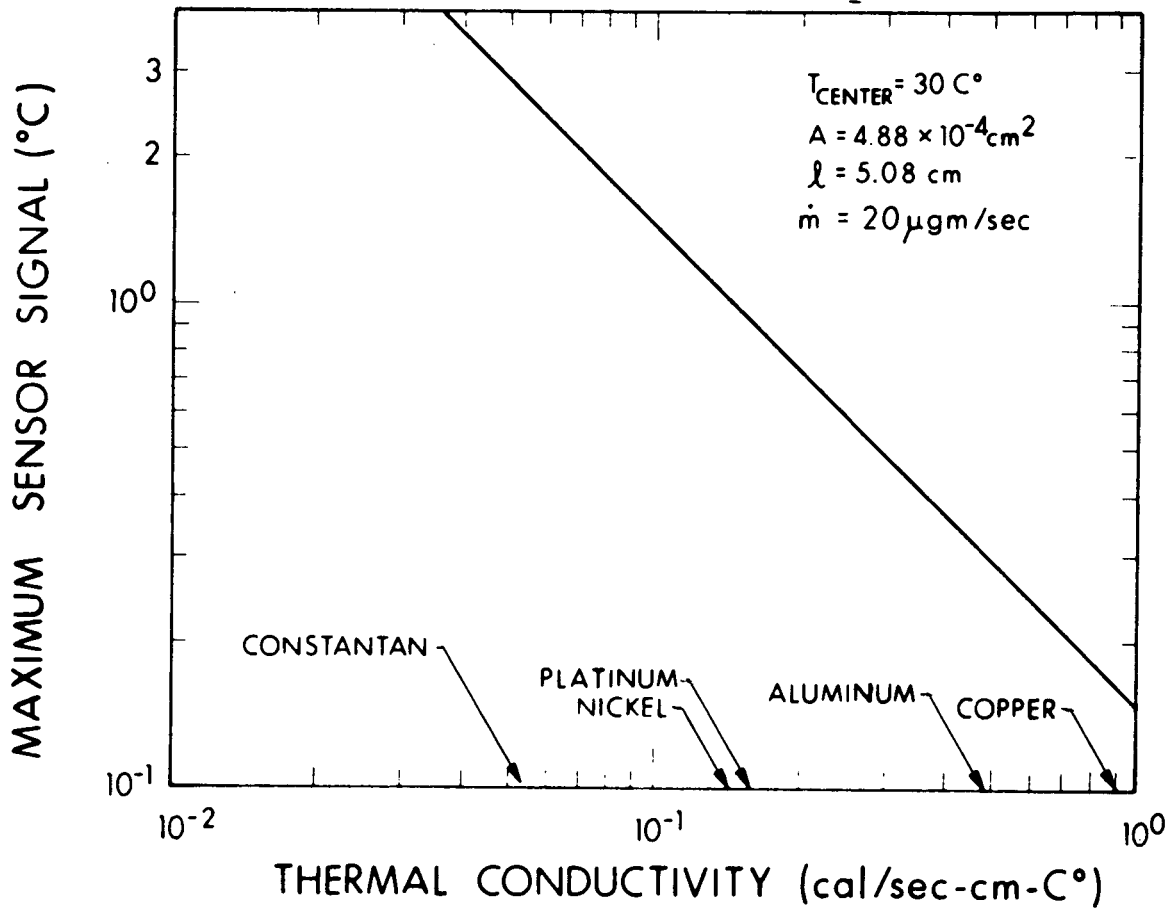
Figure V-2. Maximum Sensor Signal as a Function of Thermal
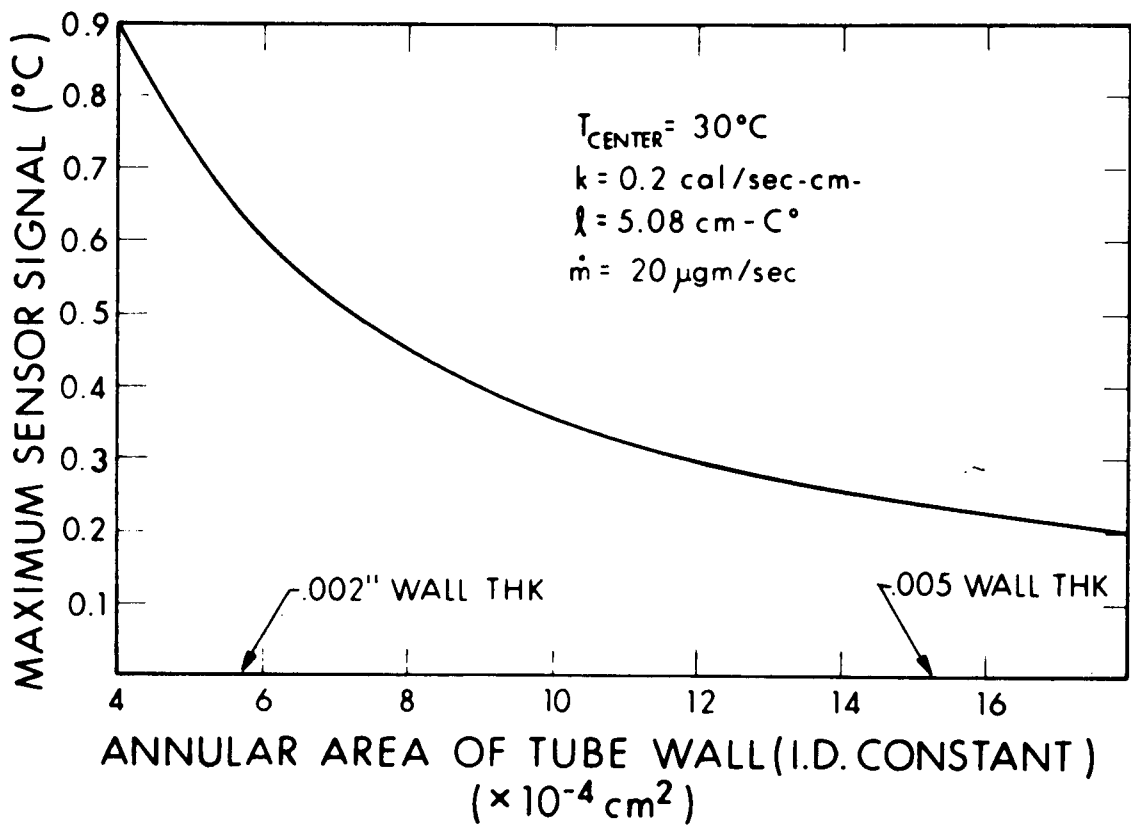Conductivity of Metering Tube

Figure V-3.   Maximum Sensor Signal as a Function of Annular Area
             of Metering Tube Wall (I.D. Constant)

In Fig. V-4 the theoretical sensor signal is plotted as a function of the temperature difference between the tube center and the tube at $\pm\ell/2$. Also shown are experimental data points taken at a mass flow rate of 20 μgm/sec using a simplified version of the EOS mass flow meter which was specially constructed to test the marked increase in sensitivity predicted by this analysis. The realization of the predicted increase in sensitivity indicates that by incorporating the other other design features discussed above it should be possible to achieve optimum sensitivity.

Utilizing the design considerations described here we have theoretically examined the maximum sensor signal (in $^{\circ}$C) as a function of mass flow rate (fluid velocity) for the following conditions: $A = 4.9 \times 10^{-2} cm^2$, $\ell = 5.08 cm$, $k = 0.14$ and $k' = 6.91 \times 10^{-4} cal/sec\text{-}cm\text{-}C^{\circ}$, C (glycerol) = $0.47 cal/g\text{-}C^{\circ}$, $T_{center} = 30^{\circ}C$, $T_{o} = 20^{\circ}C$ and i.d. of metering tube = 0.010 inch. Figure V-5 shows the linearity of the sensor signal with mass flow rate over a practical range for these conditions. This type of curve has also obtained for the mass flow meter used in the tests to examine the effect of increasing the temperature at the center of the tube. These data are shown in Fig. V-6 for two different values of the temperature at the tube center. The offset of the $T_{c} = 63^{\circ}C$ curve at $\dot{m} = 0$ is due to an error in zeroing the meter caused by a finite pressure head of propellant in the reservoir. This type error was not present for the $T_{c} = 51^{\circ}C$ curve.

In summary, the important features which affect the sensitivity of the thermo-differential mass flow meter have been examined both theoretically and experimentally with the result that a better understanding of the ways to obtain optimum sensitivity have resulted. It is suggested that this understanding be utilized in any continuation of colloid thruster research.
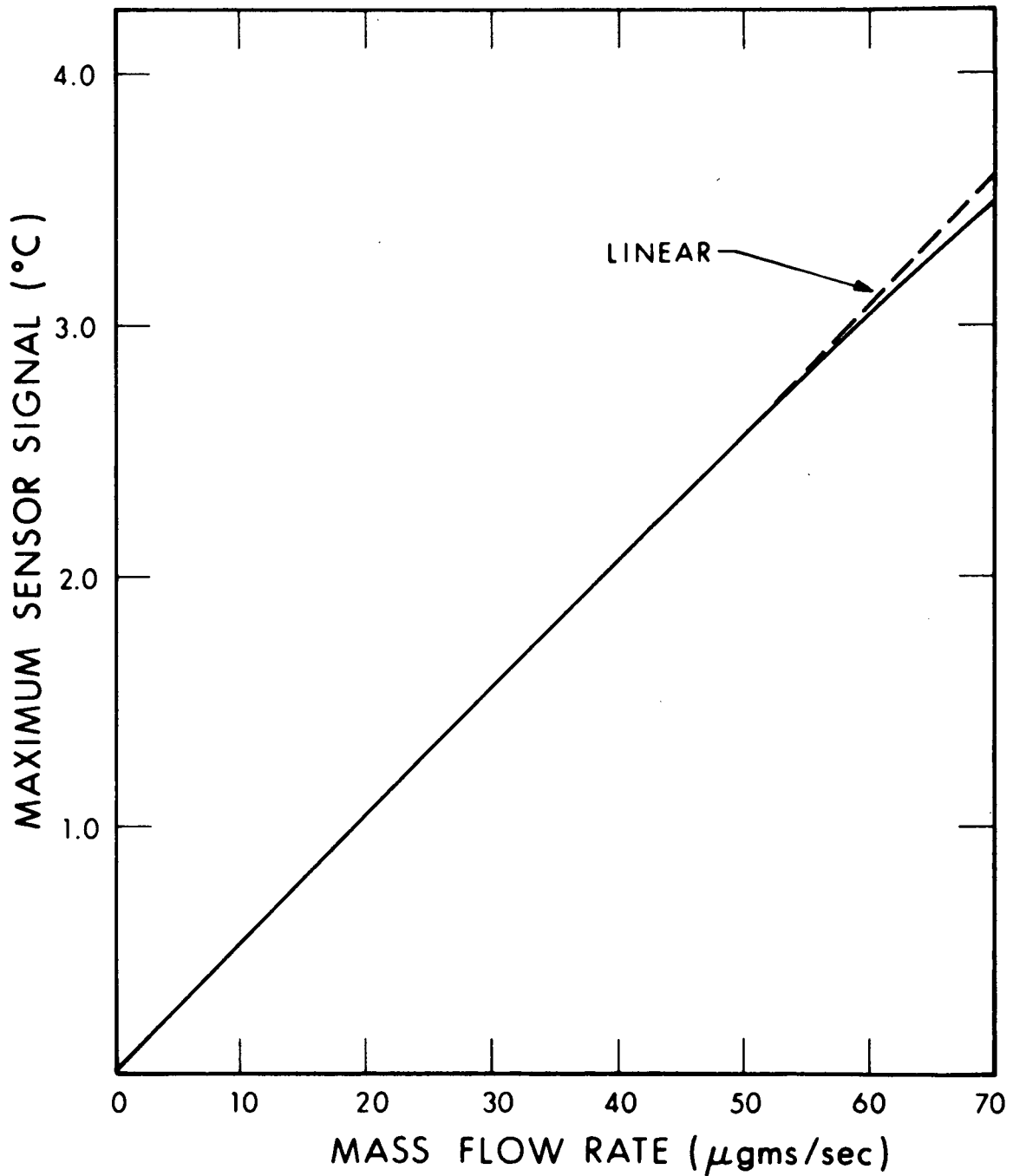
Figure V-4. Maximum Sensor Signal as a Function of Mass
Flowrate
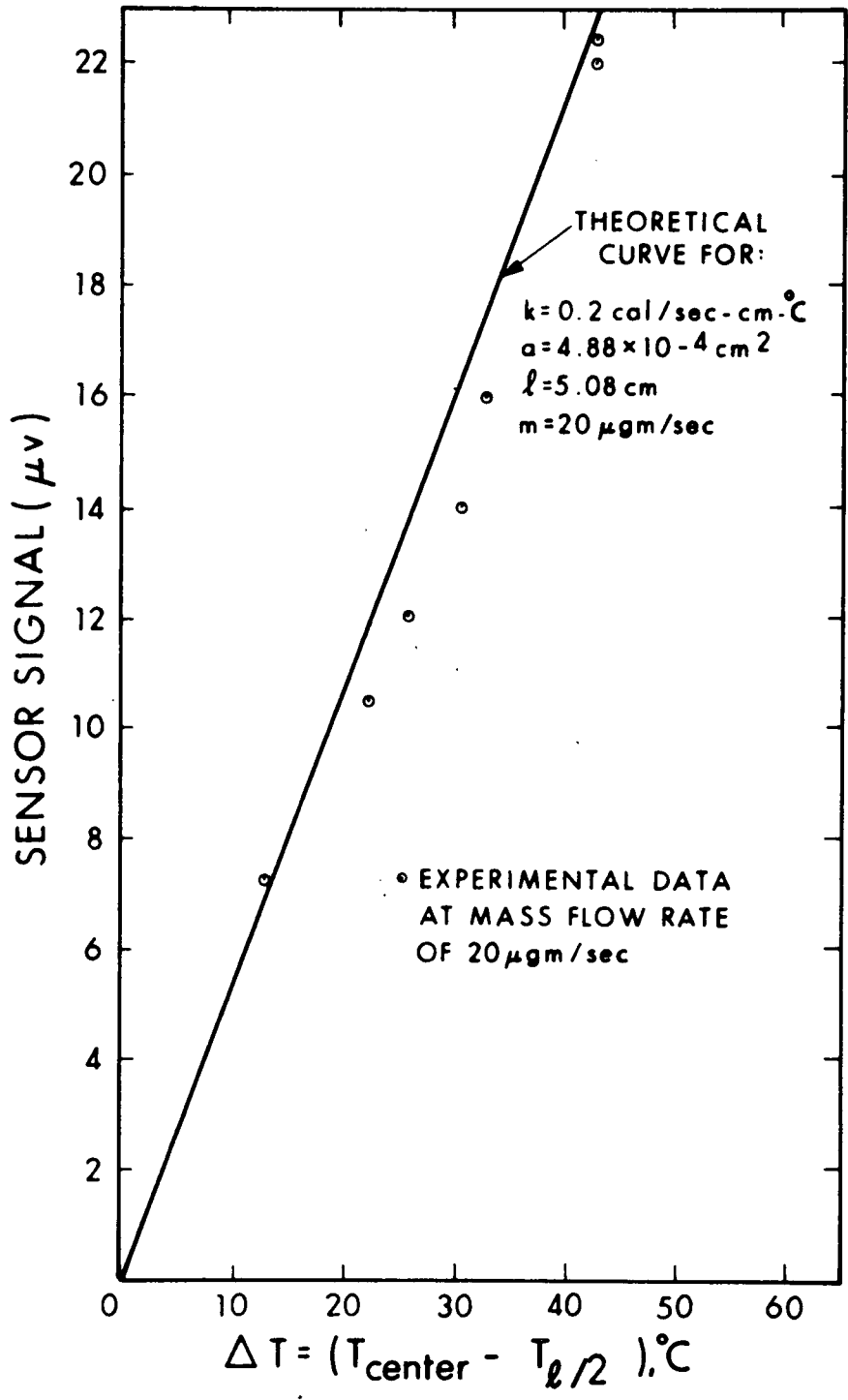
Figure V-5. Mass Flow Meter Signals as a Function of Temperature Difference
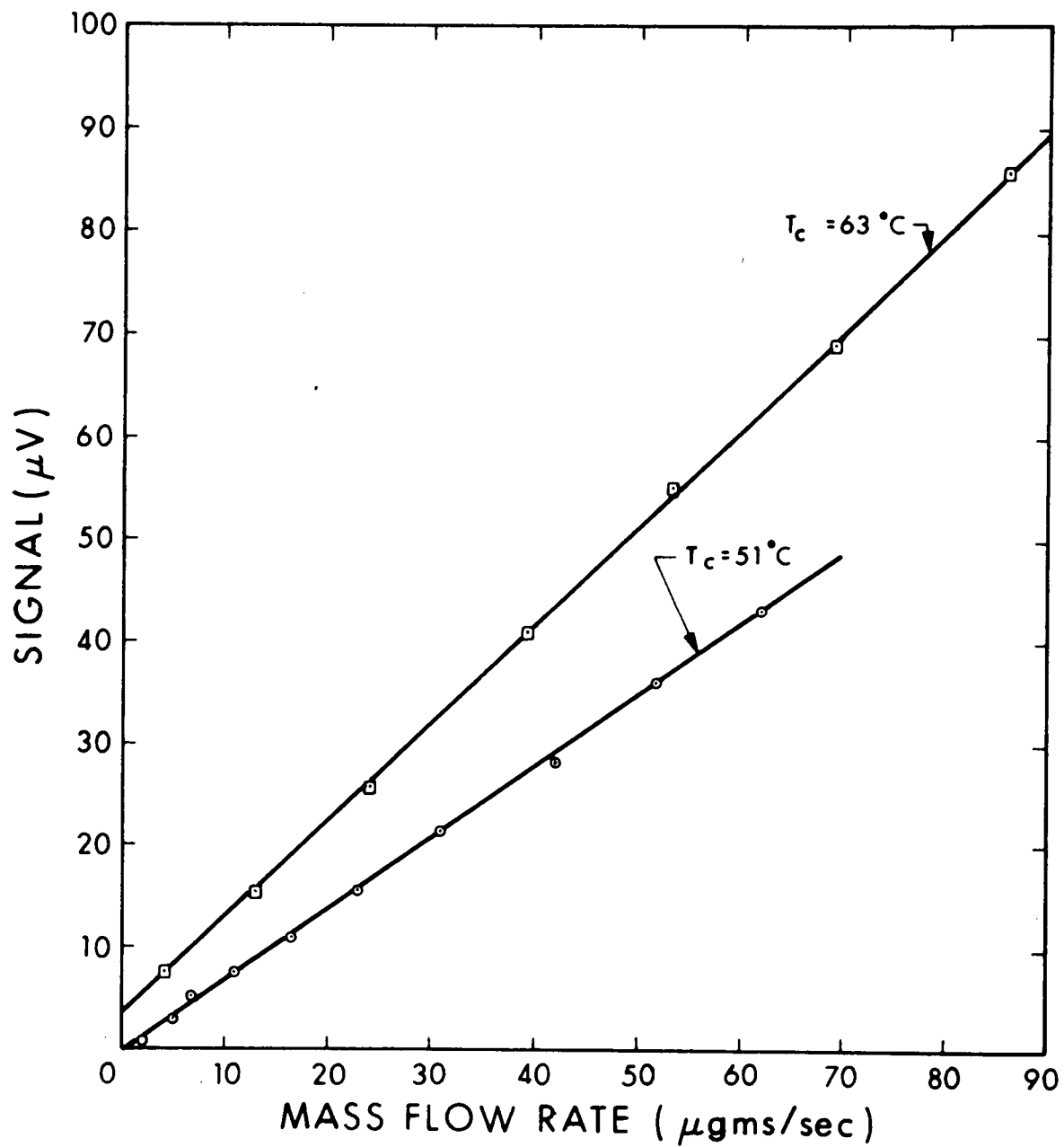
Figure V-6.   Mass Flow Meter Signal as a Function of Mass
Flow Rate

APPENDIX VI

PROPELLANT ANALYSIS

Methods to increase specific impulse over previous performance levels
were investigated during this program. Past analytical studies and
supporting experimental work have indicated that the performance index
k_o must be increased to achieve higher specific impulse (Section 2.2).
Increasing k_o can be accomplished using either a geometrical configu-
ration which results in higher electric fields at the emitter tip or
a dopant-fluid combination yielding higher specific charges. Analyti-
cal studies of the mechanics of the effectiveness of a dopant in a
fluid as a means of increasing k_o were examined since the possibility
of significant improvement in the specific charge appears to occur in
this area.

Semi-analytical considerations are first made in which the performance
index (k_o) is used as a possible means of selecting fluid/dopant combi-
nations for testing to achieve higher specific impulses. An analytical
study is presented of charge generation in an electrolytic propellant
fluid which theoretically predicts the measured specific charge depen-
dence upon temperature and the dependence on other physical variables
(Ref. 1 and 3). Moreover, the theory relates the specific charge to
the total number of dissolved solute molecules, initial degree of
dissociation, the fluid density, electric field configuration and di-
electric constant. It is interesting to note that the theory can be
used to calculate a "zero" field degree of dissociation. The theory
is a result of combining the analytical work describing colloid thruster
operation in the near linear region (Ref. 1 and 4) with a theory for the
dependence of molecular dissociation upon intense electric fields origi-
nally developed by Onsager (Ref. 7) in 1934.

The results of the analytical studies are beneficial in that they isolate
those physical parameters which may exert the primary influence in deter-

mining the specific charge in the electrostatic spraying process. Further propellant research involving a more extensive experimental study of these parameters and their effects, can now use these concepts to provide a significant and meaningful direction.

Maximum Specific Charge Index

Consider an electrolytic propellant solution with positive and negative ions dispersed in a dielectric medium (solvent). When the fluid is in motion, it is desired to know the equivalent flow of positive current corresponding to the mass flow rate. The current flow I^+, of positive ions is expressed by

$$I^+ = zNe\dot{V}, \qquad \text{(VI-1)}$$

where z is the electrochemical valency, N is the number of positive ions per cm^3, e is the electronic charge and $\dot{V}$ is the volume flow per second of propellant. The rate of volume flow is related to mass flow rate by

$$\dot{V} = \frac{\dot{m}}{\rho^*} \qquad \text{(VI-2)}$$

where ρ^* is the density of the propellant and takes into account the weight of solute dissolved in the solvent assuming no volume change. The density is then

$$\rho^* = \frac{(W_1 + W_2)}{V}, \qquad \text{(VI-3)}$$

where W_1 is the weight of solute, W_2 is the weight of solvent and V is the volume of solute in cm^3. The number of ions per cm^3, N, can be determined from

$$N \text{ (ions/cm}^3) = \frac{\alpha_o W_1}{\left(n_1 A^+ + n_2 A^-\right) m_p V} \qquad \text{(VI-4)}$$

where A^+ and A^- are the atomic mass numbers of the cation and anion respectfully, α_o is the degree of dissociation (ratio of active to total number of molecules), n_1 and n_2 are the number of cation and anion molecules contributing to the gram molecular weight, and m_p is the proton rest mass. Using Eqs. (VI-2), (VI-3) and (VI-4) the current flow is

$$I = \left[\frac{\alpha_o z e W_1}{m_p(n_1 A^+ + n_2 A^-)(W_1 + W_2)} \right] \dot{m} \qquad (VI-5)$$

Note the similarity of this formulation with the expression for emitter current given by

$$I = <C> \dot{m}, \qquad (VI-6)$$

where $<C>$ is the mean specific charge. Assuming all the positive ions in solution become droplet surface charge during the electrostatic spraying process, the maximum specific charge available (not considering other limiting factors) is

$$\left[\frac{\alpha_o z e W_1}{m_p(n_1 A^+ + n_2 A^-)(W_1 + W_2)} \right] = C_m \qquad (VI-7)$$

This holds for an ensemble where the charge is distributed evenly among droplets of the same size.

For an example of the magnitude of C_m, consider a solution of 20 gms NaI/100 ml glycerol. The terms on the left-hand side of equation (VI-7) have the following values:

$e = 1.6 \times 10^{-19}$ coulomb $\qquad\qquad n_2 = 1$

$W_1 = 20$ gms $\qquad\qquad\qquad\qquad A^+ = 23$ (Na) AMU

$z = 1$ $\qquad\qquad\qquad\qquad\qquad A^- = 127$ (I) AMU

$$m_p = 1.67 \times 10^{-24} \, \text{gm/AMU} \qquad W_2 = 126 \, \text{gms}$$

$$n_1 = 1 \qquad \alpha_o = 1 \text{ (complete dissociation assumed)}.$$

Therefore for a 100 percent efficient, completely dissociated system, a mass flow rate of $10 \mu g/\text{sec}$ would correspond to a positive current flow (I) of 870 μA. A typical annulus current range for $m = 10 \mu g/\text{sec}$ achieved in operation using a NaI dopant is 10 to 30 μA. This corresponds to specific charges of 1×10^3 to 3×10^3 coulomb/kg. C_m has been computed for a number of electrolytic substances and listed in Table I. The values are all calculated for a mixture of 20 gms of the electrolytic substance per 100 ml of glycerol.

TABLE VI-1

COMPOUND	$C_m (10^6 \text{coul/kg})$
NaI	8.74
LiI	9.85
LaI_3	7.62
ZnI_2	8.24
NaBr	12.8
LiBr	15.4
$MgCl_2$	27.8
NaOH	32.8

It is expected that the electrolytic compound with the largest C_m should be capable of transferring the greatest amount of charge in solution to a droplet surface. Of those compounds listed in Table VI-1, only data for NaI and LiI is available to test the significance of C_m. Lithium Iodide, which has the largest C_m of the two, results in a higher specific impulse beam than NaI under identical operating conditions.

The number of potential ions in solution (including those ions from dissociation through the usual chemical kinetics and ion production by high field dissociation) must be dependent on concentration. Figure VI-1 shows the number of ions available for a completely dissociated electrolyte per solute weight in grams 100 ml glycerol. Note that (based on the assumption of complete dissociation) 70 gms of LaI_3 is required to produce the same number of ions in solution as 20 gms of NaI. Compared to the NaI solution, attempts to achieve higher specific charge involving amounts of LaI_3 less than 70 gms may not be meaningful. On the other hand such large quantities of LaI_3 may not be totally soluble. It is not suggested that these statements are indeed the case but are made to point out possible tradeoffs in the course of fluid experimentation. Although Fig. VI-1 shows NaI has 3.5 times more positive ions in solution than LaI_3 at equal solute weights, their C_m values do not reflect such a large difference. This is because the La ion has a valency of three while Na has a valency of one. The high C_m calculated for NaOH is indicative of its small gram-molecular weight.

Charged Particle Generation Theory
Source Operation Theory from Droplet Considerations

In general, the current (I) from a charged particle source such as the annulus can be expressed by

$$I = <C>\dot{m}, \qquad (VI-8)$$

where $<C>$ is the mean charge-to-mass ratio of the charged droplets and $\dot{m}$ is the mass flow rate of the fluid. Although the net charge possessed by the droplets is strictly surface charge, one can treat the charge in a mathematical sense as distributed throughout the droplet volume according to

$$\frac{eN}{\rho} = <C>, \qquad (VI-9)$$

where N is the net number of charges per unit volume, e is the electronic charge and ρ is the density of the fluid. Further, one can distinguish

4040-Final

$C.3$
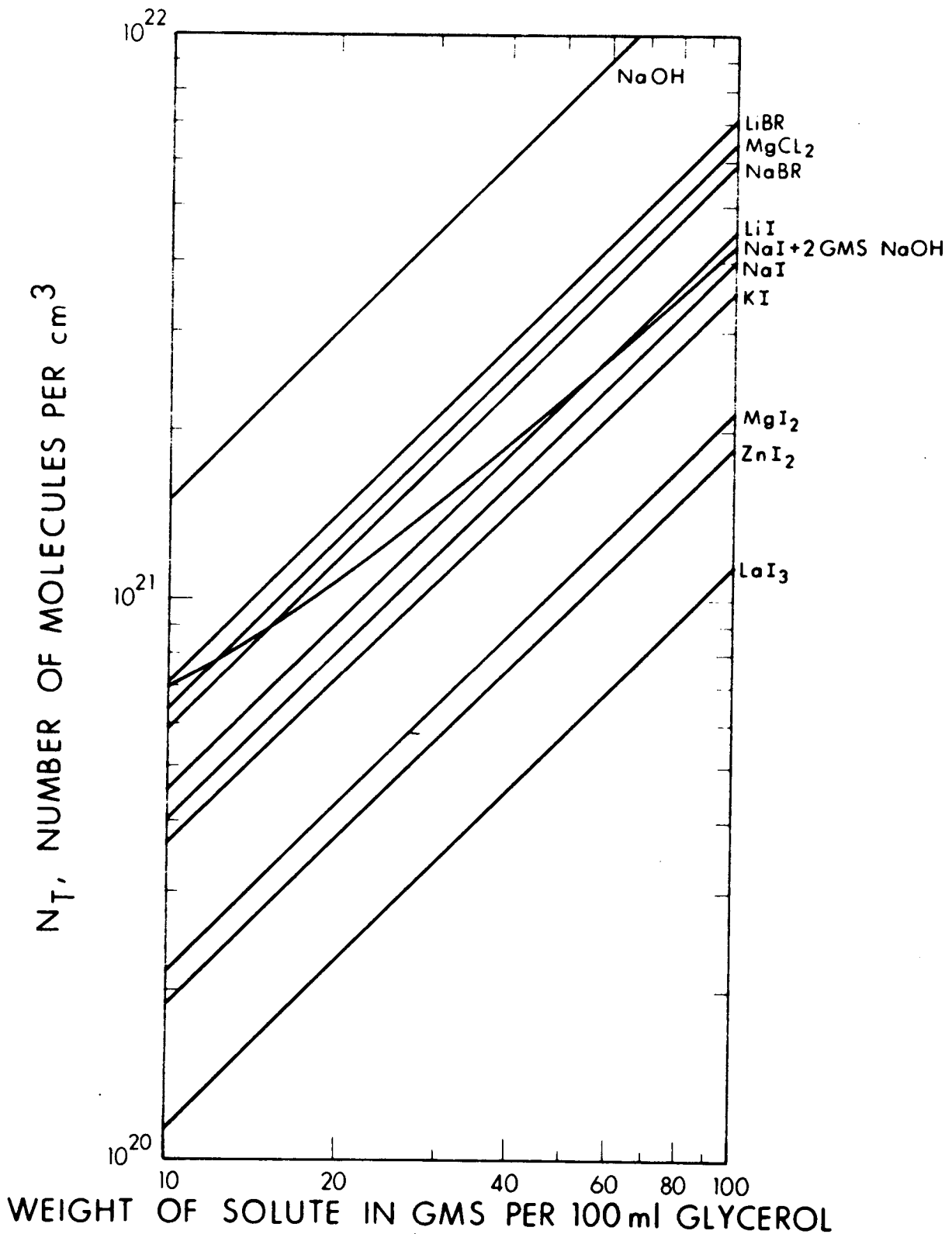
Figure VI-1. Number of Molecules (Available Ions for a Completely
Dissociated Electrolyte) for Various Solute Weights
in Glycerol

between contributions to charge arising from two sources:

1.) $N(0)$, the number of positive charges present at "zero" field
2.) $N(V)$, the number of positive charges generated by the application of voltage, V.

Therefore,

$$\frac{e}{\rho}\left[N(0) + N(V)\right] = <C>, \tag{VI-10}$$

where

$$\frac{e}{\rho} N(0) = <C_1>, \tag{VI-11}$$

and

$$\frac{e}{\rho} N(V) = <C_2>. \tag{VI-12}$$

For the region of source operation where the current varies linearly with mass flow rate, the dependence of $<C>$ on voltage can be expressed as

$$<C_2> = k_o^2 V, \tag{VI-13}$$

where k_o^2 is a source performance index (described in Section 2.2 and Refs. 1-4), V is the voltage applied to the source, and it is assumed that $<C_2>$ is much larger than $<C_1>$. From Eqs. (VI-12) and VI-13) we have

$$\frac{e}{\rho} N(V) = k_o^2 V. \tag{VI-14}$$

Equation (VI-14) can be expressed in differential form to relate the change in the number of positive charges with respect to the voltage change as

$$\frac{\triangle N}{\triangle V} = k_o^2 \rho/e \tag{VI-15}$$

Therefore the change in the number of net charges on emitted droplets with voltage is proportional to ρ/e and k_o^2 (determined from source performance). Results from experimental source studies lead to the

conclusion that k_o^2 is dependent on the magnitude of the electric field at the emitting surfaces, the nature of the electrolytic mixture, and the temperature of the fluid. One of the purposes of this analysis is to relate the quantitative dependence of k_o^2 on these and other physical parameters.

To examine the order of magnitude of $\Delta N/\Delta V$ under conditions of actual source operation, let $k_o^2 = 0.25$, $\rho = 1.26 \times 10^{-3} kg/cm^3$ and $e = 1.6 \times 10^{-19}$ coulombs, and solve for $\Delta N/\Delta V$:

$$\frac{\Delta N}{\Delta V} \sim 2 \times 10^{18} \left(\frac{charges}{cm^2 - kV} \right). \qquad (VI-16)$$

The number of charges consistent with a charge-to-mass ratio range of 1×10^3 to 6×10^3 coul/kg (a suitable range for electric propulsion) calculated from $N = \rho/e\langle C \rangle$ are 8×10^{18} to $4 \times 10^{19}/cm^3$ respectfully. For $\Delta V = 15$ kV, Eq. (VI-16) gives $\Delta N = 3 \times 10^{19}/cm^3$ corresponding to 4×10^3 coul/kg. Hence from a reservoir of $10^{21}/cm^3$ dissolved molecules, charges are generated at the rate of $2 \times 10^{18}/cm^3$ per kilovolt to produce a beam of charged droplets having a charge density on the order of $10^{19}/cm^3$.

Equation (VI-15) can be solved to express the charge generating nature of k_o^2 as

$$k_o^2 = \frac{e}{\rho} \frac{\Delta N}{\Delta V} \qquad (VI-17)$$

Therefore k_o^2 (for a given source geometry) is proportional to the rate at which charges are generated by application of a voltage. When an equivalent voltage is applied to sources of varied geometrical configuration, differences in the magnitude of the electric field intensity will determine the value of k_o^2. A more fundamental index, the same for any source geometry for a given fluid, would express k_o^2 in terms of the change in N with respect to the electric field.

High Field Dissociation in Weak Electrolytes

A theory describing the increase in the concentration of free ions
by applying intense electric fields to weak electrolytes in good
agreement with subsequent experimental investigations was outlined by
Onsager (Ref. 7). According to the theory, the ratio of the degree of
dissociation in an electric field E to the degree of dissociation at
zero field is

$$\frac{\alpha(E)}{\alpha_o} = \left(F(b) \right)^{1/2}, \tag{VI-18}$$

for $\alpha(E) \ll 1$. The parameter b in Eq. (VI-16) is given by

$$b = \frac{z_1^2 z_2^2 \left(\Lambda_1 + \Lambda_2 \right)}{z_2 \Lambda_1 + z_1 \Lambda_2} \; 9.636 \; \frac{E}{DT^2}, \tag{VI-19}$$

where z_1 and z_2 are the valences of the ions, Λ_1 and Λ_2 are
equivalent conductances, E is the electric field in volts cm, D is
the dielectric constant and T is the absolute temperature. For electro-
lytes where the valences of the cation and anion are one (i.e., a 1-1
electrolyte), Eq. (VI-19) reduces to the relation

$$b = 9.636 \; \frac{E}{DT^2} . \tag{VI-20}$$

Colloid electrostatic thrusters presently use propellant fluids which
are 1-1 electrolytes, e.g. NaI or LiI salts in glycerol.

For the case of large b($b \geq 3$) Onsager's derviation for F(b) becomes

$$\tag{VI-21}$$

$$F(b) \cong \left(\frac{2}{\pi} \right)^{1/2} (8b)^{-3/4} e^{(8b)^{1/2}} \left[1 - \frac{3}{8(8b)^{1/2}} - \frac{15}{128(8b)} - \frac{105}{1024(8b)^{3/2}} \right]$$

The function $\left(F(b)\right)^{1/2}$ versus the parameter b is illustrated in Fig. VI-2 and values of F(b) and $(F(b))^{1/2}$ computed using Eq. (VI-19) are listed in Table VI-2.

In general, the degree of dissociation (α_0), in the absence of applied fields is given by $\alpha_0 = N(0)/N_T$, where N(0) is the concentration of free ions in a zero field and N_T is the total number of dissolved molecules. Further, $\alpha(E) = N(E)/N_T$, where N(E) is the concentration of free ions generated in solution when field E is applied.

Although the dissociation kinetics are altered by the applied field, producing a concentration N(E)>N(0), we shall interpret the net effect of the field as contributing a free ion concentration in excess of N(0) according to

$$N(V)_{fluid} = N(E) - N(0), \qquad (VI-22)$$

where N(V) is the additional ion concentration due to the application of voltage to the fluid. From Eqs. (VI-16) and (VI-22) and using the expression for α_0 and N(E), we have the relation

$$N(V)_{fluid} = \alpha_0 N_T \left[\left(F(b)\right)^{1/2} - 1 \right] \qquad (VI-23)$$

To relate the voltage dependent charge on an ensemble of droplets in a charged particle beam as given by Eq. (VI-14) to the number of free ions in a fluid generated by the field dissociation mechanism expressed by Eq. (VI-23) we make the following simple assumption:

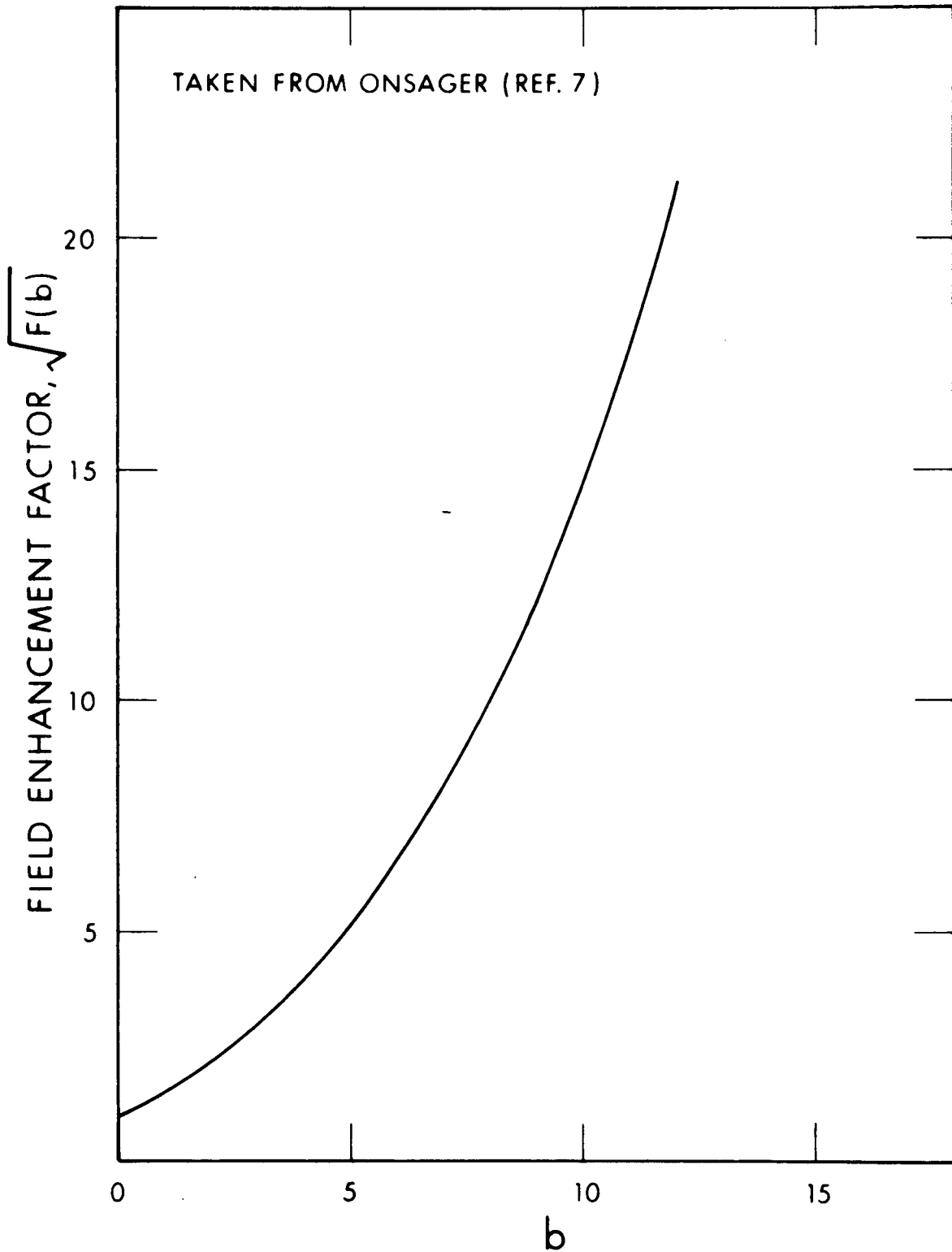$$N(V) \text{ droplets} = N(V) \text{ fluid} \qquad (VI-24)$$

4040-Final

Figure VI-2. The Function $\sqrt{F(b)}$ versus the Parameter b (from Ref. 7)

TABLE VI-2

TABULATION OF b, F(b) and $\sqrt{F(b)}$

b	F(b)	$\sqrt{F(b)}$
3.000	9.059	3.010
3.100	9.600	3.098
3.200	10.166	3.188
3.300	10.760	3.280
3.400	11.383	3.374
3.500	12.035	3.469
3.600	12.717	3.566
3.700	13.431	3.665
3.800	14.179	3.765
3.900	14.961	3.868
4.000	15.778	3.972
4.100	16.633	4.078
4.200	17.526	4.186
4.300	18.459	4.296
4.400	19.434	4.408
4.500	20.451	4.522
4.600	21.514	4.638
4.700	22.622	4.756
4.800	23.779	4.876
4.900	24.986	4.999
5.000	26.244	5.123
5.100	27.556	5.249
5.200	28.923	5.378
5.300	30.348	5.509
5.400	31.832	5.642
5.500	33.379	5.777
5.600	34.989	5.915
5.700	36.666	6.055
5.800	38.411	6.198
5.900	40.227	6.342
6.000	42.117	6.490
6.100	44.083	6.640
6.200	46.128	6.792
6.300	48.254	6.947
6.400	50.465	7.104
6.500	52.763	7.264
6.600	55.151	7.426
6.700	57.632	7.592
6.800	60.211	7.760
6.900	62.888	7.930
7.000	65.670	8.104
7.100	68.557	8.280
7.200	71.555	8.459
7.300	74.667	8.641
7.400	77.897	8.826
7.500	81.248	9.014

b	F(b)	$\sqrt{F(b)}$
7.600	84.725	9.205
7.700	88.332	9.398
7.800	92.072	9.595
7.900	95.951	9.795
8.000	99.973	9.999
8.100	104.143	10.205
8.200	108.465	10.415
8.300	112.944	10.628
8.400	117.585	10.844
8.500	122.394	11.063
8.600	127.376	11.286
8.700	132.536	11.512
8.800	137.880	11.742
8.900	143.414	11.976
9.000	149.144	12.212
9.100	155.075	12.453
9.200	161.215	12.697
9.300	167.569	12.945
9.400	174.145	13.196
9.500	180.949	13.452
9.600	187.988	13.711
9.700	195.270	13.974
9.800	202.801	14.241
9.900	210.591	14.512
10.000	218.645	14.787
10.100	226.973	15.066
10.200	235.583	15.349
10.300	244.483	15.636
10.400	253.683	15.927
10.500	263.190	16.223
10.600	273.015	16.523
10.700	283.166	16.828
10.800	293.653	17.136
10.900	304.488	17.450
11.000	315.678	17.767
11.100	327.236	18.090
11.200	339.172	18.417
11.300	351.497	18.748
11.400	364.223	19.085
11.500	377.361	19.426
11.600	390.923	19.772
11.700	404.921	20.123
11.800	419.368	20.478
11.900	434.278	20.839
12.000	449.663	21.205
12.100	465.537	21.576
12.200	481.914	21.953
12.300	498.808	22.334
12.400	516.234	22.721
12.500	534.208	23.113
12.600	552.744	23.511
12.700	571.859	23.914
12.800	591.569	24.322
12.900	611.890	24.736
13.000	632.841	25.156

By setting Eq. (VI-14) equal to Eq. (VI-23) and solving for $k_o^2 V$
the result is

$$\langle C \rangle = k_o^2 V = \frac{e \alpha_o N_T}{\rho} \left[\left[F(b) \right]^{1/2} - 1 \right] . \tag{VI-25}$$

Since $N(0) = \alpha_o N_T$ Eq. (VI-25) can be written as

$$\langle C \rangle = \frac{e N(0)}{\rho} + k_o^2 V = \frac{e \alpha_o N_T}{\rho} \left(F(b) \right)^{1/2} \tag{VI-26}$$

Equation (VI-26) further illustrates that the charges of the
sprayed droplets originate within the propellant fluid by two dis-
tinct mechanisms. Before application of voltage, there is a supply
of free charge made available by the formation of ion pairs when
molecules of the solute react chemically with the solvent.
Secondly, ion pairs are generated upon the application of intense
electric fields. For the case of a weak electrolyte, the latter
charge generating mechanism (strongly dependent on the electric
field) is the dominant source of free charge that contributes to
the charge-to-mass ratio of the droplets.

Comparison of Theory with Experiment

The charge-to-mass ratio of droplets emitted from a charged particle
source generally increases with increasing electric field and decreas-
ing mass flow rate. The nature of this dependence is contained in the
dimensionless function $f^2(x)$ (see Fig. 1 of report text). As a result, the
expression for the charge-to-mass ratio obtained from purely field consider-
ations must be modified to include a mass flow effect. As the field and mass
flow rate are independent variables, we have chosen to express their
interdependence in the following form:

$$\langle C \rangle = \frac{e \alpha_o N_T}{\rho} f^2(x) \left(F(b) \right)^{1/2} , \tag{VI-27}$$

where $f^2(x)$ has the value of unity when the mass flow rate is zero and decreases with increasing $\dot{m}$. As a result $<C>$ given by Eq. (VI-26) is the maximum charge-to-mass ratio in the limit as the mass flow rate approaches zero.

Equation (VI-27) can be used to calculate $<C>$ as a function of temperature for comparison with a value of α_o is estimated using the experimental data. Using the general dependence of $<C>$ with mass flow rate at various temperatures shown in Fig. (VI-3) the single-valuedness of α_o can be established. From the figure we can write:

$$\alpha_o = \frac{a_1 <C> \max}{\left[F_1(b)\right]^{1/2}} = \frac{a_1 <C_2> \max}{\left[F_2(b)\right]^{1/2}} = \frac{a_1 <C_3> \max}{\left[F_3(b)\right]^{1/2}} \qquad (VI-28)$$

independent of the curve chosen for the computation where the constant a_1 is ρ/eN_T.

Using Eq. (VI-28), α_o was calculated for an electrolytic solution consisting of 30 gms NaI/100 ml glycerol. The density of the solution was taken to be 1.56×10^{-3} kg/cm^3 and $N_T = 1.2 \times 10^{21}$/cm^3. For the computation of the parameter b, the dielectric constant of glycerol was taken to be 45, the electric field to be 4×10^6 volts/cm, and the temperature equal to $0°C$. The value of $<C>_{max}$ was determined from extrapolation of experimental data to be 1.9×10^3 coul/kg. Substitution of the above quantities yields the result that $\alpha_o = 6.42 \times 10^{-4}$. This value of α_o was used in subsequent calculations involving $<C>$.

Figure VI-4 shows data illustrating the experimentally measured variation of $<C>$ with temperature at constant mass flow rates for a charged emitter operating at 15 kilovolts. Theoretical values of $<C>$ from Eq. (VI-28) are compared with the variations in $<C>$ with temperature at a mass flow rate of 20 μgms/sec. The results of this comparison are shown in Fig. VI-5 where the solid line is the theoretical curve and
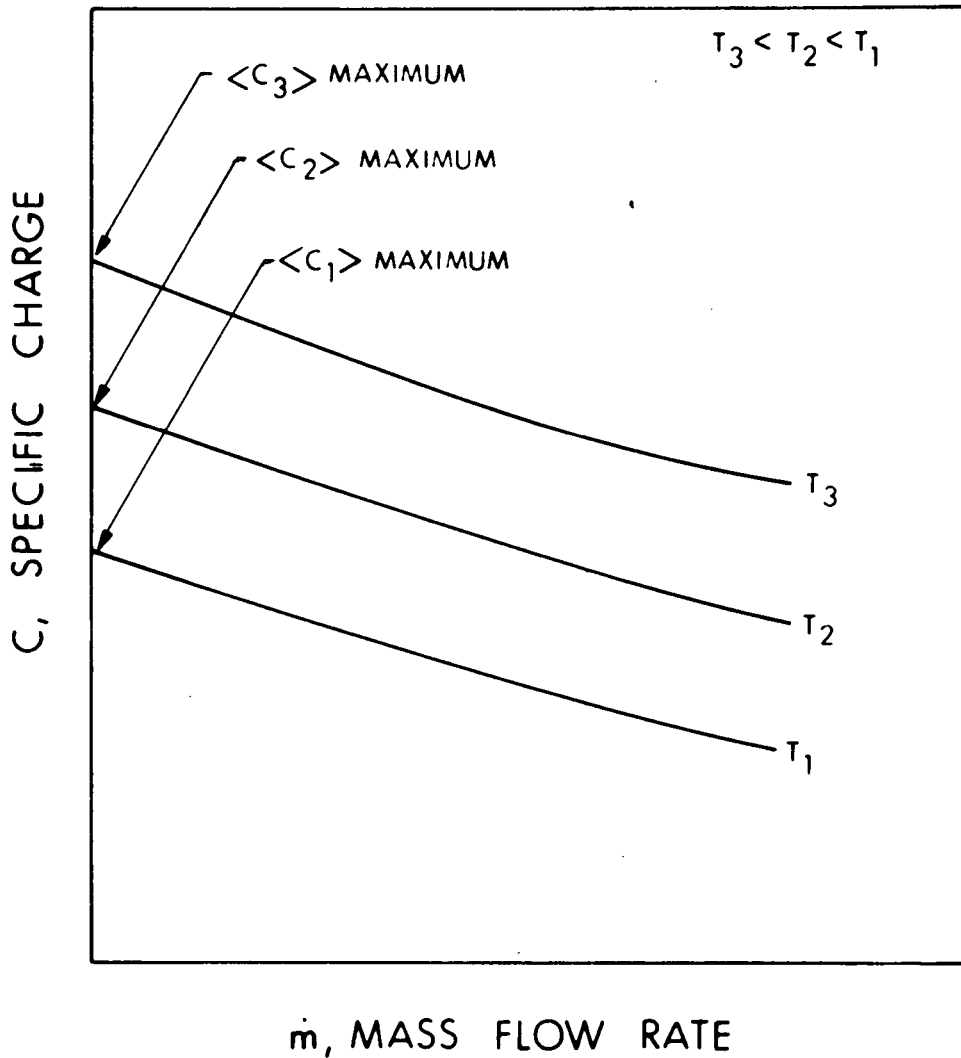
Figure VI-3. Characteristic Dependence of Specific Charge
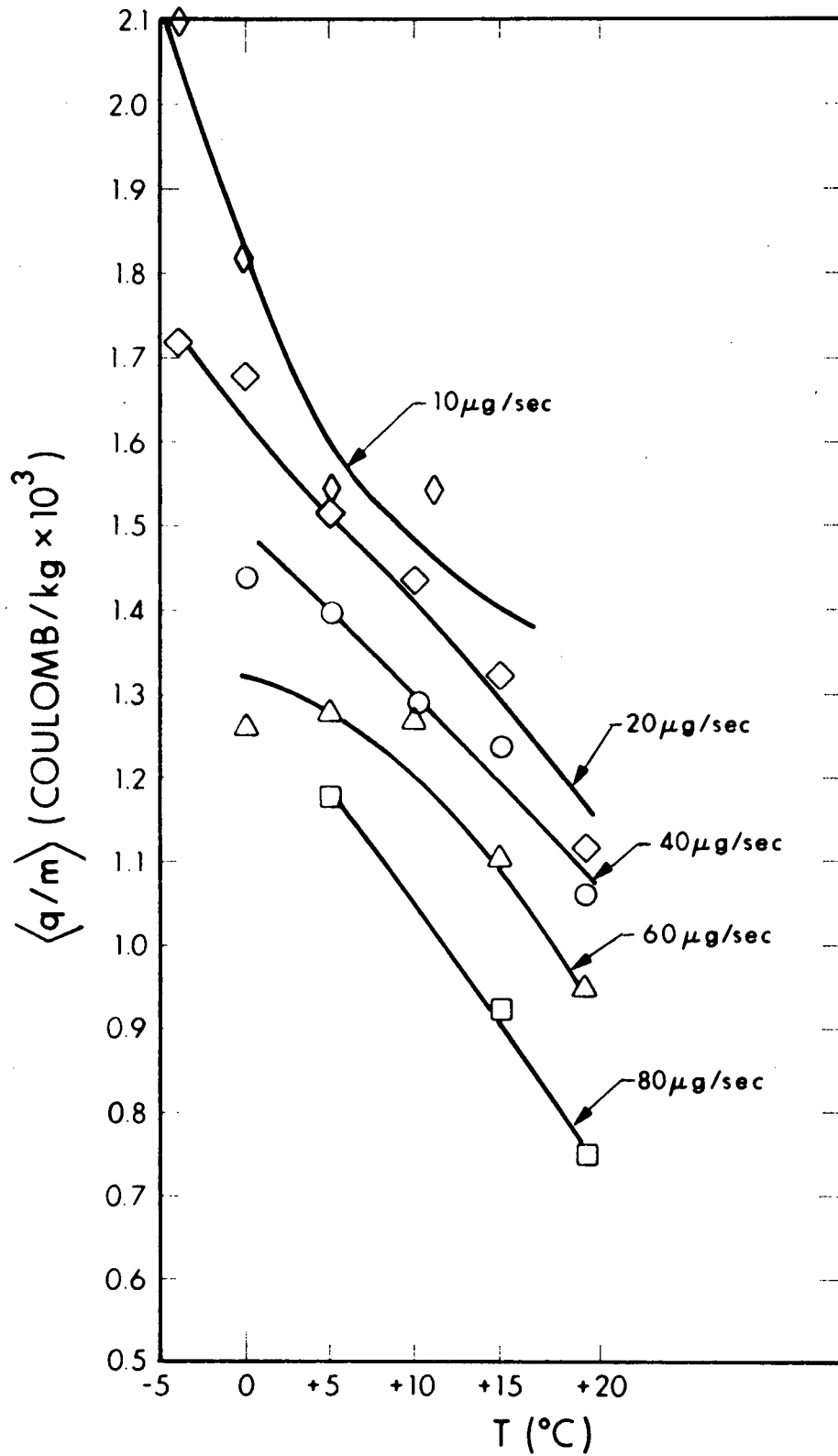on Mass Flowrate for Various Temperatures

Figure VI-4. Variation of Specific Charge with Temperature for Constant Mass Flowrates for Annulus A06, Run 7006-02
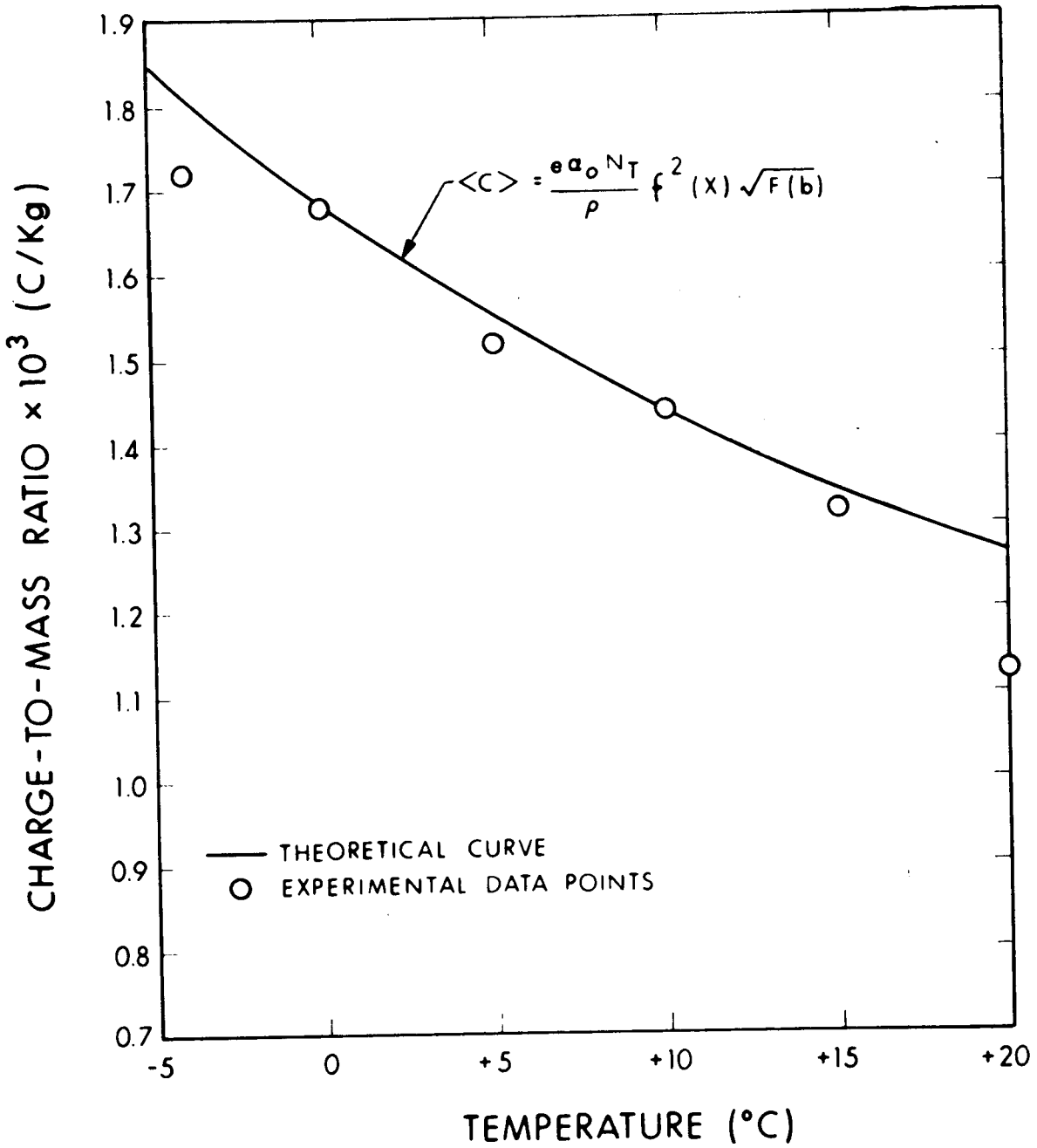
Figure VI-5. Comparison of Theoretical and Experimental Dependence of Charge-to-Mass Ratio on Temperature

the circles denote experimental data points. The value of b at
each temperature was calculated using Eq. (VI-20) and correspond-
ing values for $\left(F(b)\right)^{1/2}$ determined from Fig. VI-2 or from
Table VI-2. For this calculation $f^2(X)$ was chosen to be 0.9.
The agreement between the theoretical curve with the experimental
data is quite good.

CONCLUSIONS

The excellent agreement of the theortical dependence of charge-to-mass
ratio on temperature with experimental data may successfully extend the
range of electric fields over which Onsager's theory is applicable.
More data is required to verify the charge-to-mass dependence on electric
field.

The bridge between Onsager's high field dissociation theory in weak
electrolytes with the generation of a charged droplets was provided
by the assumption given by Eq. (VI-24).

Essentially, the model proposed treats the charge generation in a bulk
electrolytic liquid and uses charged droplet analysis from TOF techniques
to derive a theoretical expression for charge-to-mass ratio, an important
parameter for colloid thrusters. Equation (VI-24) states that the number
of positive ions generated in a given fluid volume are preserved in drop-
let formation. That is, the number of free positive ions in solution per
unit volume is equivalent to the positive surface charge per unit volume
of droplets. The assumption that the parameter $b \geq 3$ for the application
of Eq. (VI-21) is justifiable due to the high field involved in the electro-
static spraying process. Only the upper limit of applicability is brought
into question here. According to Onsager, Eq. (VI-18) applies when the
number of ions generated by the fields is small when compared to the total
number of molecules, $\alpha(E) \ll 1$. For our case, $N_T \sim 1.2 \times 10^{21}/cm^3$ and
$N(V) \sim 3 \times 10^{19}/cm^3$ yields $\alpha(E) \sim 2.5 \times 10^{-2}$ (where we have assumed $N(0)$ small
compared to $N(V)$).

Further, it has been assumed (not discussed by Onsager) that the dielectric
constant remains unchanged in the solution, independent of field or charge
distribution. The bulk dielectric constant for (undoped) glycerin has
been used in these calculations. The effect of different ionic species
dissolved in a solvent is known to lower the dielectric constant, the

amount of decrease being dependent on the particular ionic species involved (Ref. 8 and 9).

The success so far in the theoretical prediction of charge-to-mass ratios although limited implies that electrical aspects of droplet production are the most important. The equations do not take into account the seemingly intractable droplet formation and separation process where surface tension and viscosity effects are involved. Nevertheless, agreement of Eq. (VI-28) with the data is remarkable. If fluid viscosity exerted a large effect on $\langle C \rangle$ one would expect a larger variation in $\langle C \rangle$ in Fig. VI-4 where the bulk viscosity of glycerol varies by a factor of 10. Yet the percentage change by $\langle C \rangle$ is very small and predicted by Eq. (VI-28) which does not incorporate hydrodynamic quantities such as viscosity and surface tension.

Among those parameters which are known to play a significant role in determining charge-to-mass ratios are the electric field and temperature. Interestingly, Eq. (VI-20) predicts that the dielectric constant of the solvent medium (in the presence of dissolved solute) will have a dominating effect in determining charge-to-mass ratio. In fact, reducing the dielectric constant by a factor of two should have the same effect as doubling the electric field strength. On the other hand, to achieve a comparable change by varying the temperature requires differences on the order of hundreds of degrees. Therefore, it would seem fruitful to search for solvents having lower dielectric constants than glycerol which also meet vapor pressure and ionic dopant solubility criteria.

4040-Final

REFERENCES

1. Electro-Optical Systems, Interim Report for Colloid Thruster Technology, Contract No. NAS 5-21025 (30 June 1969 - 20 June 1970).

2. J. Perel, A.Y. Yahiku, J.F. Mahoney, H.L. Daley and A. Sherman, "Operational Characteristics of Colloid Thrusters", J. Spacecraft and Rockets, 8, 702 (1971)

3. A.Y. Yahiku, J.F. Mahoney, H.L. Daley, and J. Perel, "Experimental Study of Colloid Annular Thrusters", AIAA Paper No. 70-1112, AIAA 8th Electric Propulsion Conference (Stanford, California, Aug. 31-Sept.2, 1970).

4. J. Perel, J.F. Mahoney and A.Y. Yahiku, "Analytical Study of Colloid Annular Thrusters," AIAA Paper No. 70-1113, AIAA 8th Electric Propulsion Conference (Stanford, Calif., Aug. 31 - Sept. 2, 1970).

5. K.W. Stark, and A. Sherman, "Research and Development in Needle and Slit Colloid Thrusters", NASA TN D-5305, Goddard Space Flight Center, Greenbelt, Md., February 1970.

6. S. Zafran and J.C. Beynon, "Colloid Microthruster System Life Test", J. Spacecraft and Rockets 8, 140 (1971).

7. L. Onsager, "Deviations from Ohm's Law in Weak Electrolytes", J. Chem. Phys., 2, 599 (1934).

8. J.B. Hasted, D.M. Ritson, and C.H. Collie, "Dielectric Properties of Aqueous Ionic Solutions, Part I and II", J. Chem. Phys., 16, 1 (1948).

9. C.P. Smyth, Dielectric Behavior and Structure, ,(McGraw Hill, N.Y.) 1965) p90.

4040-Final